DEEP NEAR-INERTIAL WAVES IN THE SAMOAN PASSAGE

A DISSERTATION SUBMITTED TO THE GRADUATE DIVISION OF THE UNIVERSITY OF HAWAIʻI AT MĀNOA IN PARTIAL FULFILLMENT OF THE REQUIREMENTS FOR THE DEGREE OF

DOCTOR OF PHILOSOPHY

IN

OCEANOGRAPHY

MAY 2019

By

Kelly Pearson-Potts

Dissertation Committee:

Glenn Carter, Chairperson
Matthew Alford
James Girton
Doug Luther
Philip Thompson
Eva-Marie Nosal

© 2019

Kelly Pearson-Potts

This work is licensed under a Creative Commons BY-NC-SA License.

Acknowledgements

Thank you to Glenn for all of your help and commitment to our weekly meetings. I have enjoyed the evolution of how we work together and my growing understanding of your facial expressions. My favorite moments have been when one of us does not understand the other person and we resort to drawing on your chalkboard.

Thank you to my Samoan Passage group: Glenn, Matthew, James, Gunnar, Larry, Jesse and Shuwen for their input and enthusiasm in my research. I have enjoyed all of the time that we have spent together and have particularly enjoyed watching your enthusiasm for research.

Thank you to my committee for highlighting the fun science can be. I appreciate your support and insights.

Thank you to John Mickett, Eric Boget, Andrew Cookson, Keith Magness, Janna Köhler, Trina Litchendorf, Zoë Parsons, Andy Pickering, Tessa Tafua, Samuel Fletcher, Tahmeena Aslam, Thomas Decloedt, Alofa Aleta, Vaatele Tauinaola Deepika Goundar, and the captains and crews of the *R/V Revelle* and *R/V Thompson* for all of their help in collecting the data used in this research.

Thank you to my family without whom I would have never survived this process.

To Alex, my rock who has put up with middle of the night typing in bed, clumsy midnight broken dishes and numerous food runs. I can't wait to see where we go from here.

To my parents and siblings who have been positive and supportive with their words and actions. I appreciate your constant coverage of my back during the highs and the lows. I love you.

To Michelle who has dealt with crying phone calls and silence all with such understanding and grace. Well, maybe also a few swear words and alcohol. Now that I will be back on the mainland, I am looking forward to seeing you more in person.

To my Hawaiian family: the Patinos and the Ishiis thank you all for being sunshine in an otherwise sunshiny state. I love that you all bring a smile to my face and don't mind if I show up if I am missing a family atmosphere or if I am grumpy after a night of no sleep.

This work was funded by the National Science Foundation under grants OCE-1029268, OCE-1657264, OCE-1657870, OCE-1658027, OCE-1657795, and OCE-1029483.

Abstract

The Samoan Passage Abyssal Mixing Experiment (SPAM-Ex) is a unique data set comprised of a deep mooring array and a long-term mooring time series in the Samoan Passage (10°S, 170°W), an abyssal constriction through which the majority of deep and abyssal waters in the North Pacific pass. As near-inertial waves (NIW) are episodic and propagating, they are difficult to observe. Deep observations of NIW are even more difficult and as a result there are a limited number of deep observations of NIW. This work hopes to provide a detailed description of such an observation.

Depth-time plots of velocity and shear, in addition to rotary spectra at each depth, show a NI event between 4000 and 4200 m on the mooring array. An idealized model is formed to describe the shear by using a plane wave method fitting the best fit. Plane wave solutions found independently for each mooring and show spatial coherence across the array. The idealized model found the wave to be comprised of both a downward propagating and an upward propagating wave, used for all subsequent research. Wavelet analysis shows multiple NIW over the course of the long-term, 17-month mooring deployment. These events correspond to an increase in the magnitude of the v velocity and a decrease in the magnitude of the u velocity. In addition, on average the 27.786 kg/m^3 isopycnal is depressed 14 m on average during NI events.

In calculating the various variables describe the observed NIW, the inclusion of the horizontal Coriolis term ($\tilde{f}$) is found to be important. This solution was expanded across latitudes and values of N^2 near the inertial limit. It was found that $\tilde{f}$ should be included in the dispersion relation at low latitudes ($< 10°$) and low stratification ($N < 0.001\,s^{-1}$) and for groups speeds at all latitudes at low stratification ($N < 0.003\,s^{-1}$). As a result, inclusion of $\tilde{f}$ specifically in the group speed calculation is particularly important during ray tracing.

Increased mixing was found to correspond to the NIW but only at one of the 4 moorings in the array. Both meridional shear above the interface and below the interface are found to have a high correlation to the near-inertial variation in depth integrated dissipation rate. This corresponds to a

decrease, but not reversal in the magnitude of the velocity. Low Richardson numbers (below 0.25) correspond to increased turbulence indicating the observed mixing is shear driven.

Table of Contents

List of Tables

List of Figures

CHAPTER 1

Introduction

1.1 Samoan Passage

The Meridional Overturning Circulation (MOC) in the Pacific is dramatically different from the Atlantic. There is limited deep water formation in the North Pacific (Warren, 1983) and consequently the deep branch of the Pacific MOC (PMOC) is supplied with waters only from the south. Approximately 20 Sv of cold water sinks near Antarctica and flows northward into the Pacific Ocean around Campbell Plateau and along Kermadec Ridge. Half of this water makes it into the North Pacific (Roemmich et al., 1996), where it spreads throughout the basin, mixing with the waters above and gradually warming. Eventually, the warmed waters return southward at intermediate depths, completing the PMOC (Wunsch & Ferrari, 2004). The North Pacific's long residence time and large capacity for storage of heat and atmospheric carbon dioxide make it important to climate on longer time scales (Sloyan et al., 2013, Fukasawa et al., 2004, Purkey & Johnson, 2013).

A submarine ridge extending from French Polynesia to Fiji largely blocks the northward transport of abyssal waters. The first appreciable gap deeper than 4000 m is the Samoan Passage (10°S, 170°W). Roemmich et al. (1996) found more than half, 6 Sv, of the northward transport into the North

Pacific at 9°S was through the narrow Samoan Passage, with other main flow routes across Robbie Ridge, 1.1 Sv, and around Manikiki Plateau, 2.8 Sv. Also, using hydrographic measurements, Taft et al. (1991) and Johnson et al. (1994) estimated northward transport of water colder than 1.2°C through the passage of 6.0 Sv and 4.8 Sv, respectively. Rudnick (1997) calculated a volume transport of 6.0 Sv with a standard deviation of 1.5 Sv below 4000 m from a six-element mooring array deployed from 1992 to 1994 at the mouth of the passage. A 2012–2014 reoccupation of the four western moorings recalculated the transport below 4000 m to be 5.4 Sv, a statistically significant decrease over the 20-year interval at the 68% but not at the 95% confidence levels (Voet et al., 2016).

The Samoan Passage constricts flow, resulting in substantial acceleration (Reid & Lonsdale, 1974), hydraulic control (Freeland, 2001), and turbulence (Roemmich et al., 1996). Freeland (2001) observed velocities of up to 6.7 cm/s and believed there to be western intensification of the flow. Over the length of the Passage, mixing erases the NADW signature and modifies the deep and bottom waters (Alford et al., 2013).

1.2 Near-inertial waves

Near-inertial waves (NIWs) are internal waves near the inertial frequency, f. NIWs were first observed in 1930 by Ekman (1953) and since then, some general characteristics of NIWs have been determined. NIWs are polarized, clockwise in the northern hemisphere and counter-clockwise in the southern hemisphere. In rotary spectra, NIWs appear as a peak in the anticyclonic component near the inertial limit. NIWs are episodic and freely propagating (Fu, 1981). NIWs tend to propagate toward the equator, during which time the wave becomes super-inertial relative to the local f, with frequencies between 1 and 1.2f (Alford et al., 2016). While propagating equatorward the NIWs also propagate vertically: upward/downward phase propagation corresponds to downward/upward energy propagation. As the wave propagates, variation of the Coriolis frequency can modify the horizontal length scales (D'Asaro, 1989). The rate of vertical energy transfer is affected by the variation of this horizontal length scale. Pure inertial motion is composed of only horizontal rotation.

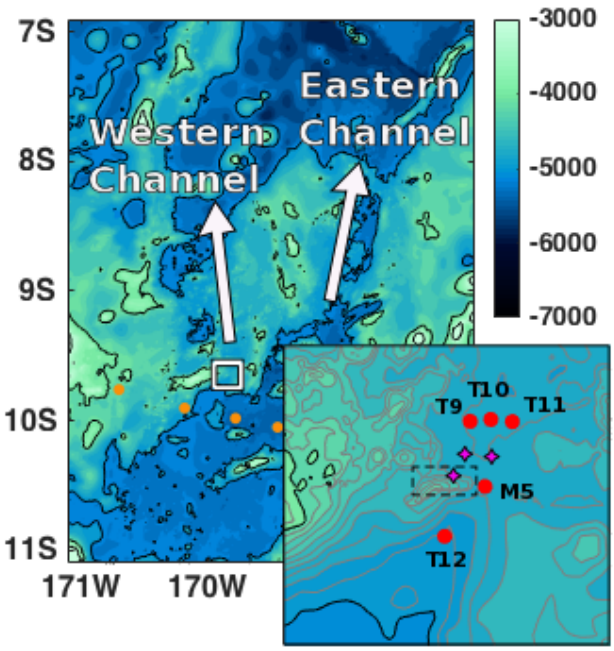

Figure 1.1: Map of the Samoan Passage and zoomed-in on the sill between the eastern and western channels. Orange circles in the main panel indicate the mooring locations in Rudnick (1997) and Voet et al. (2016). The zoomed-in map area is denoted by the white box. Mooring locations used in this work are marked with red circles. Purple diamonds denote the location of full depth Conductivity, Temperature, and Depth (CTD) casts, while the dashed black box outlines the bump.

In near-inertial motion the horizontal rotation tilts, resulting in vertical displacements that modulate the stratification.

There are a myriad of NIW sources that include wind, wave-wave interactions, lee waves, and spontaneous generation. Observations tend to be linked to events at the surface because surface observations are easier to make and consequently more extensive. However, this is to not say that a large proportion of NIWs could not originate at the surface. There is evidence of increased mixing associated with seasonal storms (Alford & Whitmont, 2007). The amount of NI energy propagating out of the mixed layer and into the deep ocean is uncertain. Alford et al. (2012) found 12-33% of mixed layer NI energy propagates to the deep ocean; D'Asaro (1995) found an energy decrease of 36%($\pm$10%) in the mixed layer after three weeks; and in a numerical study, Furuichi et al. (2008) found 15% of NI energy to propagate out of the upper 150 m. All in all, there are simply not enough observations of NIWs and NIW generation to know the partition of NI energy sources.

Along the propagation path, three factors are known to influence the kinematic structure of NIWs: buoyancy, currents, and topography. Variable stratification changes vertical wavelengths (Leaman & Sanford, 1975). Also, strong variations in N^2 can cause internal reflection (Tomczak & Godfrey, 2003). NIWs are known to interact strongly with currents, in particular mesoscale features (Kunze, 1985, Olbers, 1981). Internal waves can reflect (Eriksen, 1982) or scatter (Simmons & Alford, 2012) off of topography. In addition, topography can inhibit the lateral scales of NIWs (Gill, 1984, Lighthill, 1978).

Observations show increased mixing due to NIWs (Alford & Gregg, 2001, Hebert & Moum, 1994). Alford et al. (2016) hypothesizes that, in the interior ocean, mixing due to NIWs could exceed that of internal tides. Kunze & Sanford (1986) found amplification of the NIW during propagation against the flow and NIW dispersal with reduction in energy during propagation with the flow. Enhanced energy is associated with increased production of turbulence and mixing.

1.3 Dissertation outline

This thesis focuses on moored hydrographic and velocity observations in the region surrounding the sill at the mouth of the western channel (white box in Fig. 1.1). This 3 km-wide sill shallows from 4,900 m to 4,600 m over the course of 4 km. The western side of the sill has a secondary topographic feature reaching 400 m above the sill, which we will denote as "the bump" (dashed black box in Fig. 1.1). Alford et al. (2013) found that flow over the bump resulted in strong overturns and dissipation, while flow around the the eastern side of the bump had less acceleration and shear, producing less mixing.

The next chapter describes the mooring deployments around the southern sill, the location of this research. A table of dates and locations is included for ease of reference.

The third chapter describes near-inertial wave observations from a mooring array, in the deep ocean, during the Samoan Passage Abyssal Mixing Experiment (SPAM-Ex). It is difficult to observe NIW in the ocean, let alone in the deep ocean on a mooring array. A description of the observed waves is presented. The wave was found to propagate equatorward. The wave was spatially coherent across all moorings. The best-fit solution, which describes both the zonal and meridional shears, was a downward propagating and a $\frac{1}{4}$-the-amplitude, upward propagating interference pattern. NI energy appears to be symmetric about an energy peak at 4,100 m, disagreeing with Voet et al. (2015), and corresponding to a peak in N^2. Over a 17-month period, we observed seven near-inertial events with a lull between May and November. These events were best described by a two-wave solution and propagated equatorward. The NIW observed is found to be robust across moorings and not unique in the area.

Key points:

- Coherent NIW observed with four short-term moorings in the Samoan Passage between 4000 and 4200 m.
- Even though moorings are separated by only a few kilometers, differences between moorings

are observed which relate to variations in N^2, currents, and adjacent topography .

- Long-term mooring in the same region observed 7 NI events over the course of a 17-month deployment. NI events corresponded to a decrease in the magnitude of the u velocity component, and an increase in the magnitude of the v velocity component, and a depression of the isotherms above 3900 m.

- The plane wave description of the observations is composed of the superposition of two waves: a downward propagating wave and an upward propagating wave.

The fourth chapter discusses the inclusion of the horizontal Coriolis term in the calculation of horizontal wavenumbers, group speeds, and the intrinsic frequency. Traditionally, only the vertical component of the Coriolis vector is included in the Navier Stokes equations of geophysical fluid motion. However, in regions of low stratification and/or low latitude, the horizontal component of the Coriolis vector ($\tilde{f} = 2\Omega \cos\phi$, where Ω =angular velocity of rotation and ϕ =latitude) is not negligible. This research, motivated by observations of deep NIWs in the Samoan Passage (9°40.65'S), highlights the error associated with neglecting $\tilde{f}$ at low latitudes and in low stratification regions. The Samoan passage is used as a case study to illustrate a practical application of the inclusion of $\tilde{f}$ in various calculations. Our calculations are expanded beyond the specific case of the Samoan Passage to a range of latitudes and N in an attempt to assess the relative importance for NIWs by applying the inertial limit. The inclusion of the horizontal component in the dispersion relation is found to have a significant difference at very low latitudes and very low N. Outside of these regions, the inclusion of $\tilde{f}$ does not make a significant difference. However, the inclusion of $\tilde{f}$ is necessary in the calculation of the group speeds. When $\tilde{f}$ is included, the percent differences of the group speeds ($\Delta_{c_{gy}}$ and $\Delta_{c_{gz}}$) exceed 20% and 10% respectively across most latitudes for $N < 0.003\,s^{-1}$. The differences in group speed result in more equatorward ray paths and more northerly inferred sources. There is no discernible difference in the calculations of the effective frequency and horizontal wavelength with the inclusion of $\tilde{f}$. Ray tracing models for NIWs, including $\tilde{f}$ show a difference in the spatial and temporal scales of their propagation paths from those calculated neglecting $\tilde{f}$.

Key points:

- $\tilde{f}$ should be included in the calculation of the dispersion relation at low stratification ($N < 0.001\,s^{-1}$) at latitudes less than 10°.
- When calculating group speeds, $\tilde{f}$ needs to be included for $N < 0.01\,s^{-1}$, at all latitudes, particularly the meridional group speed.
- As ray tracing is heavily based on the group speed, $\tilde{f}$ needs to be included for any ray path that may propagate through a region with $N < 0.01\,s^{-1}$.
- It is not necessary to include $\tilde{f}$ when calculating k_H or f_{eff} as the differences are minute and result in increased error bars.

The fifth chapter investigates a unique mixing pattern observed at one of the short-term moorings. Turbulent mixing driven by NIWs is not well documented because it is an episodic and propagating event. During a mooring deployment, in the mouth of the western sill of the Samoan Passage (Fig. 4.1), near-inertial variation of the depth-integrated (4200-4600 m) dissipation rate is observed. The NIW, discussed in chapter 3, occur above these depths between 4000 and 4200 m. Time series comparison determines the meridional shear as the most likely driving mechanism for the increased depth-integrated dissipation rate. Increased turbulence is found to occur during periods when the NIW opposes the background flow, minimizing–never reversing–the velocity. The time-averaged, depth-integrated rate is comparable to those found at two adjacent moorings where hydraulically controlled mixing dominates. As a result, NIW overturns are suspected to be shear-driven and important in the localized region. In addition conclude that mixing from NIWs should be included in a Samoan Passage mixing budget and should be considered for other deep constrictions, in particular those with accelerated flow speeds.

Key points:

- Increased mixing is found to be associated with a downward propagating wave interacting with a topographically accelerated meridional flow.

- The depth integrated dissipation rate peaks during periods when the NIW motion opposes the flow.
- Although NIWs are coherent across 10–100 km scales, interaction with currents cause variation on much smaller scales (< 1 km).

The sixth chapter is the conclusion. It includes a summary of this work, a discussion of ongoing deep near-inertial research, and future work to be done. The summary includes research highlights for each chapter in addition to a general description of work done. The discussion of ongoing deep near-inertial research describes current limitations and difficulty of research while also including the author's hopes for the future. The description of future work includes topics for the Samoan Passage, deep and abyssal constrictions, and NIWs more generally.

Chapter 7 is comprised of two appendices. The first appendix is the error analysis associated with the horizontal Coriolis calculations. Errors for f_{eff}, intrinsic frequency, horizontal wavenumber, group speeds, water properties, and ray tracing are calculated both with and without $\tilde{f}$. The second appendix details the application of the inertial limit to the percent difference of the dispersion relation and the group speeds.

CHAPTER 2

Data

2.1 Moorings

A total of five moorings were deployed within 3 km of the sill crest, as shown in Fig. 1.1. Four moorings (T9–T12) were concurrent short-term deployments (collectively denoted as T-moorings) during February 6–14, 2014. On the sill crest, there was an ~17 month deployment (M5, August 8, 2012–January 11, 2014). Each mooring spanned the bottom 1,200–1,600 m of the water column to study the deep northward transport of Antarctic-origin water and the interface with the overlying waters. T12 was located 2 km upstream of the sill (relative to the flow of Antarctic origin bottom water), whereas T9, T10, and T11 were located 3 km downstream of the sill and spaced 1 km apart. The locations, dates, and depth ranges of all five moorings are listed in Table 2.1.

All moorings were equipped with McLane moored profilers (MPs) fitted with CTDs and acoustic current meters (Doherty et al., 1999, Alford et al., 2007). The MPs on the T-moorings continuously profiled over their depth ranges (Table 1) at vertical speeds of 25–27 cm/s. Due to power restrictions on the longer deployment, the MP at M5 paused after the completion of each up or down profile. Consequently, vertical profiles of temperature, conductivity, pressure, and velocity were completed

Table 2.1: Details of the five moorings located at the sill between the Eastern and Western Channels. T-moorings are the concurrent short-term moorings and M-mooring is the long-term mooring.

	Start date	End date	Depth (m)	Latitude	Longitude	Bottom depth (m)
M5	2012-08-24	2014-01-11	3698-4710	9°38.7′S	169°48.9′W	4730
T9	2014-02-06	2014-02-13	3590-4768	9°36.0′S	169°49.5′W	4788
T10	2014-02-07	2014-02-14	3590-4804	9°36.0′S	169°48.7′W	4824
T11	2014-02-07	2014-02-14	3590-4786	9°36.0′S	169°47.8′W	4806
T12	2014-02-07	2014-02-14	3390-4976	9°40.6′S	169°50.6′W	4996

$\approx$ 1.4 hours on the T-moorings and $\approx$ 17.4 hours, 1/4 of the inertial period, on the M5 mooring. The conductivity sensors were corrected on the M5 and T9 profilers for a systematic bias, which lead to the salinities being 0.005 and 0.07 g/kg, respectively, above those observed at the other moorings. For more details on the instrumentation used in this experiment, refer to Voet et al. (2015).

CHAPTER 3

Observations of near-inertial waves

3.1 Introduction

A spectrum of freely propagating internal waves exists in the frequency band between the inertial frequency (f) and the buoyancy frequency (N) (Garrett, 2001), with NIWs (NIWs) existing near the lower limit, f. NIWs are unique in the internal wave spectrum as they tend to be variable and event-like due to the natural resonance of the fluid ocean at the Coriolis frequency in response to impulsive forcing (Kunze, 1985). Although any impulsive forcing with a resonance near f can excite NIWs, the main sources are: wind forcing the mixed layer at NI frequencies (Gill, 1984, D'Asaro, 1985, Alford & Gregg, 2001); lee waves developing a feedback system with the overlying flow (Nikurashin & Ferrari, 2010a,b); parametric subharmonic instability (PSI) (Alford et al., 2007, Alford, 2008, McComas & Muller, 1981, Muller et al., 1986, Winters, 2005, Simmonds, 2008, Hazewinkel & Winters, 2011); and interaction with balanced flows (Alford et al., 2013, 2016, Vanneste, 2012). All of which have been observed except for the lee wave feedback system.

After excitation of the NIWs, high modes stay in the local region and result in localized mixing while low modes propagate equatorward carrying the majority of NI energy. As the NIWs propagate equatorward, they become super-inertial relative to the local f and start to tilt transitioning from a purely horizontal circulation to circular rotation with a vertical component modulating the strain and stratification (Gill, 1984). In addition to equatorward propagation, the NIWs also propagate vertically. In the transit of a NIW through the ocean, three main factors can modulate the NIW propagation path: interaction with the flow, variations in the stratification, and interaction with topography. NIW experiences amplification in anticyclonic vorticity or propagation against the flow and dispersal and energy reduction in positive vorticity or propagation with the flow (Kunze & Sanford, 1986). Variations in the stratification are well known to modify the vertical propagation (WKB) in addition to internal reflection or trapping in cases of large variation. The waves may also encounter topography where they may break due to topographic scattering (Simmons & Alford, 2012) or reflect (Eriksen, 1982).

On average the NI peak contains half of the total energy in the internal waveband (Munk, 1981). NIW are a major flux of energy into the ocean. The final destination of this energy is unknown. As such, it is possible NIW contribute to deep mixing.

NIWs have been observed at deep and abyssal depths. Using moored data from the POLYMODE Experiment in the Western North Pacific, Fu (1981) showed an inertial peak slightly above f, with energy varying with depth and bottom roughness. Alford (2010) observed the downward propagation of a NIW past a mooring at 3,000 m depth. van Haren & Millot (2004) observed a peak in super-inertial energy at frequencies 2% above the local inertial frequency across all depth ranges in the Western Mediterranean Sea. They noted a secondary broader sub-inertial peak at 0.99f at a depth of 2,700 m, 300 m above the seafloor. Alford & Whitmont (2007) using a database of deep global NIW observations observed seasonal variation with an increase in events corresponding to the winter.

The North Pacific has no deep water formation, consequently, the bottom water in the basin is of Antarctic origin. The Samoan Passage (10°S, 170°W) being the westernmost gap deeper than 4,000 m in the submarine ridge extending from French Polynesia to Fiji is the location of a significant fraction of this northward transport, 5.4 Sv 2012/13 (Voet et al., 2016). As water transverses the passage,

it undergoes a significant modification; the densest Antarctic Bottom Water (AABW) signature is decreased to 1/4 of its entry density (Alford et al., 2013) due to intense mixing over the course of the Samoan Passage, 1,000 to 10,000 times typical abyssal turbulence values (Alford et al., 2013). The Samoan Passage consists of a deep Eastern channel and a more convoluted Western channel (Fig. 4.1). The volume transport below 4,000 m is split evenly between the two channels (Voet et al., 2015).

The Samoan Passage is located in a region with low annual mean energy input from the wind to near-inertial mixed layer motions (Alford, 2003). However both Rudnick (1997), Voet et al. (2016) observed NI peaks with energy decreasing toward the seafloor using moored arrays at the mouth of the Samoan Passage. The locations of the moorings are denoted as orange dots on the map of the Samoan Passage (Fig. 4.1). This NI energy is likely low mode propagation into the region. Rudnick (1997) hypothesized that bottom topography inhibited the lateral scales of the NIWs, resulting in the observed decrease in energy, whereas Voet et al. (2016) hypothesized the waves lose energy while propagating to depth.

The primary focus of this chapter is to present observational evidence of NIWs in the Samoan Passage. Section 3.2 presents the analysis methods used. In section: 3.3a a description of the water properties is provided, 3.3b finds the NI signal to be concentrated between 4000 and 4200 m in the short-term moorings (T9-T12) and above 3900 m in the long-term mooring (M5), 3.3c fits a plane wave solution to the observations and finds the best-fit to be a superposition of a downward propagating wave and a 1/4 the amplitude upward propagating wave, and 3.3d uses wavelet analysis to find 7 NI events over the course of the long-term mooring. Sections 3.4 and 3.5 are the discussion and conclusions, respectively.

3.2 Methods

3.2.1 Velocity

Depth-time plots of meridional and zonal velocities (Fig. 3.2) show a temporally periodic signal in the depth range between 4,000 and 4,200 m in each of the four concurrent T-moorings. Consecutive peaks occurred approximately every three days, consistent with the local Coriolis period of 2.99 days (0.33 cpd). Therefore, upward sloping, alternating bands of positive and negative velocities show the upward phase and downward energy propagation of a near-inertial wave.

To isolate the near-inertial signal in the shear and strain observations the time-series were bandpassed (0.5f–2f) and vertically averaged with a 40 m window.

3.2.2 Spectra

Spectral analysis places variance of a time series as a function of frequency. Rotary spectra treats two orthogonal vectors as a single complex function then separates the vector into cyclonic and anti-cyclonic rotating circular components for each frequency (Gonnella, 1972, Mooers, 1973). After decomposing the velocity or shear time series into these rotating components, a NIW will have an anticyclonic component that exceeds the cyclonic near the local inertial frequency. The frequency spectra were calculated in 4 m-depth bins and a Tukey window was applied in time. A measure of the aspect ratio of internal waves as a function of frequency is given by the rotary coefficient (Gonnella, 1972):

$$C_r = \frac{|\text{Cyclonic} - \text{AntiCyclonic}|}{\text{Cyclonic} + \text{AntiCyclonic}} \tag{3.1}$$

where $C_r = 1$ is perfectly circular motion and $C_r = 0$ is rectilinear motion.

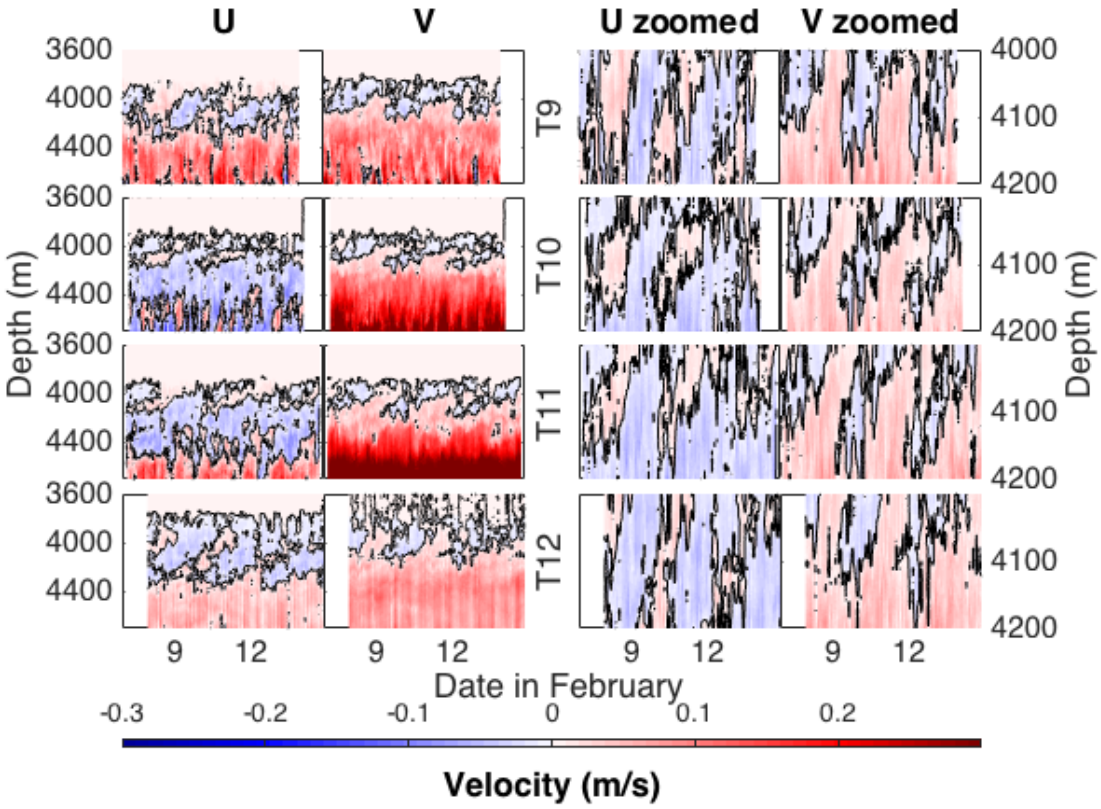

Figure 3.1: (left 2 columns) Depth-time plot of the u and v velocity components observed at each of the four short-term moorings. (right 2 columns) Zoom in on the depth range where the near-inertial pattern observed in the velocity. The x axis is the same for all plots. It begins when T9 was deployed and ends when T12 was taken out of the water. Each mooring was deployed for approximately seven days.

3.2.3 WKB stretching and scaling

Wentzel-Kramers-Brillouin (WKB) stretching is used to account for varying vertical stratification, N(z) (Leaman & Sanford, 1975, Althaus et al., 2003). For NIWs propagating through variable stratification, WKB scaling mitigates the effects of changing vertical wavelengths due to variations in N^2. WKB-stretched depths were calculated as:

$$z' = \int_z^0 \frac{N(z)}{N_0} dz, \tag{3.2}$$

where N_0 is the reference buoyancy frequency – an appropriate value for deep and abyssal waters is $10^{-3}\,s^{-1}$ (Leaman & Sanford, 1975). The observed mean buoyancy frequency for the four short-term moorings was 9.8×10^{-4} s^{-1}, confirming the applicability of the reference buoyancy frequency for the Samoan Passage. The resultant plots of shear and strain have straighter phase lines indicating WKB scaling is appropriate. To correct for amplitude modification caused by the depth varying N^2, the WKB scaled velocities are:

$$(u', v') = (u, v)\sqrt{\frac{N_0}{\langle N(z) \rangle}}, \tag{3.3}$$

where $\langle\ \rangle$ denotes a time average.

3.2.4 Shear and strain

Internal waves are identifiable in depth-time plots of shear, the vertical gradient of the speed, as bands of alternating positive and negative values. The slope of the bands is related to the wave frequency and propagation direction – downward/upward propagating wave energy with upward/downward propagating phase.

To isolate the NI signal, the WKB-stretched 2 m-binned velocity were bandpassed between 0.5f (1.5 days) and 2f (6 days), where the inertial frequency, f, is 0.33 cycles per day (cpd). Total NI shear was calculated by adding the squares of the meridional shear and the zonal shear components:

$$S^2 = \left(\frac{\partial u}{\partial z}\right)^2 + \left(\frac{\partial v}{\partial z}\right)^2. \tag{3.4}$$

Strain, the convergence or divergence of motion, was calculated using:

$$\gamma = \frac{\langle N^2 \rangle}{N^2} - 1. \tag{3.5}$$

For this calculation, it is necessary to calculate the time average over n-integer periods due to the short record length and periodic nature of NIWs. The resulting shear and strain was smoothed with 40 m vertical averaging.

3.2.5 Plane wave solution

Plane waves are used to provide wavenumbers, phase, and frequency as a means to describe the observed wave. plane wave fits to the NI bandpassed, vertically averaged, WKB-stretched-and-scaled meridional shear, zonal shear, and strain were calculated using:

$$\Psi = \mathrm{Re}[A\ \exp(2\pi i(\omega_0 t - kx - ly - m_0 z' + \phi_0))], \tag{3.6}$$

where: A = amplitude, ω_0 = observed frequency, (k, l, m_0) = wavenumbers and ϕ_0 = phase. Where the horizontal wavenumbers (k,l) are calculated from frequency and vertical wavenumber.

Using the meridional shear, zonal shear, and strain in the time versus WKB-stretched depth the values of ω_0, m_0, and ϕ_0 that best fit the observations are able to be found. This is iteratively done by varying ω_0 between 0.95f and 1.1f, m_0 between 0 and 0.1 m^{-1}, and ϕ_0 between 0 and 360 degrees, similar to Alford & Gregg (2001). The best fit solution is determined from the root mean square (RMS) difference between the calculated interference pattern and observations. A two-wave solution is calculated using the same iterative process. The direction of propagation(Θ) is calculated from the lag between the phase of the zonal shear and the strain (Pinkel, 1985):

$$\Theta = \phi(\gamma, u_z). \tag{3.7}$$

3.2.6 Wavelet analysis

The temporally varying frequency content of a time-series can be calculated using wavelets. This is important for NIWs as they are episodic events. A wavelet kernel is a function that generally has zero mean and is localized in time and frequency. The Morlet Wavelet (Grinsted et al., 2004) is defined as:

$$\Psi_o(t) = \pi^{-\frac{1}{4}} e^{i\hat{\sigma}\hat{t}} e^{-\frac{1}{2}\hat{t}^2}, \tag{3.8}$$

where $\hat{t}$ (dimensionless time) and $\hat{\sigma}$ (dimensionless frequency) are stretched in time by varying the scale and are normalized. The Morlet Wavelet, $\Psi_o(t, \sigma)$, is complex and therefore provides power and phase information for each time and frequency pair.

3.3 Results

Depth-time plots of meridional and zonal shear (Fig. 3.2) show a temporally periodic signal in the depth range between 4,000 and 4,200 m in each of the four concurrent T-moorings. Consecutive peaks occurred approximately every three days, consistent with the local inertial period of 2.99 days (0.33 cpd). Therefore, upward sloping, alternating bands of positive and negative shear show the upward phase and downward energy propagation of a NIW.

To isolate the NI signal in the shear and strain observations the time-series were bandpassed (0.5f–2f), WKB-stretched-and-scaled, and vertically smoothed over a 40 m window (Fig. 3.3). The NIW is the dominant signal between 4,000 and 4,200 m as non-bandpassed shear pattern shows similar results (not shown). In strain, the NIW pattern is more convoluted than the shear.

3.3.1 Water Properties

The depth range between 4,000 and 4,200 m in the T-moorings is distinct from the surrounding water column as it includes the interface between the Antarctic-origin water and the overlying waters. This interface is defined by a sharp thermocline and halocline, a depth of no motion, and increasing N^2

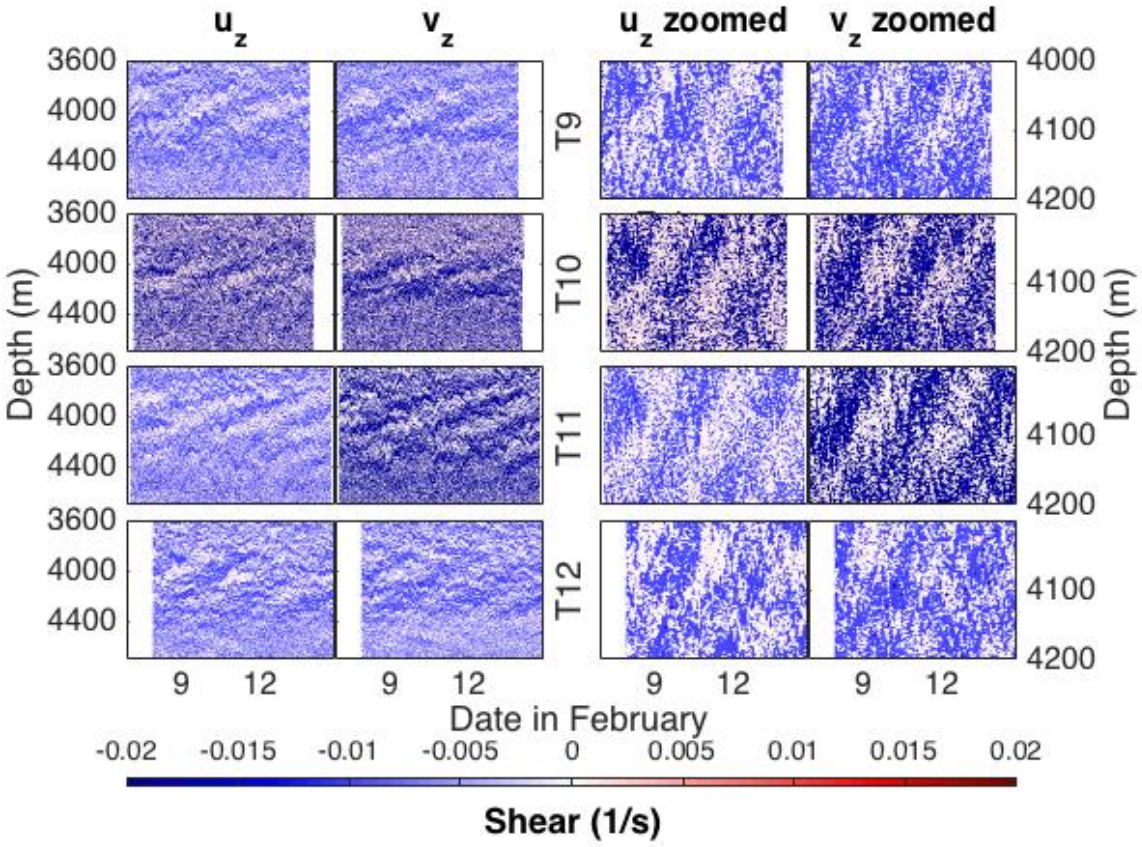

Figure 3.2: (left 2 columns) Depth-time plot of the u_z and v_z shear components observed at each of the four short-term moorings. (right 2 columns) Zoom in on the depth range where the NI pattern observed in the raw shear. The x axis is the same for all plots. It begins when T9 was deployed and ends when T12 was taken out of the water. Each mooring was deployed for approximately seven days.

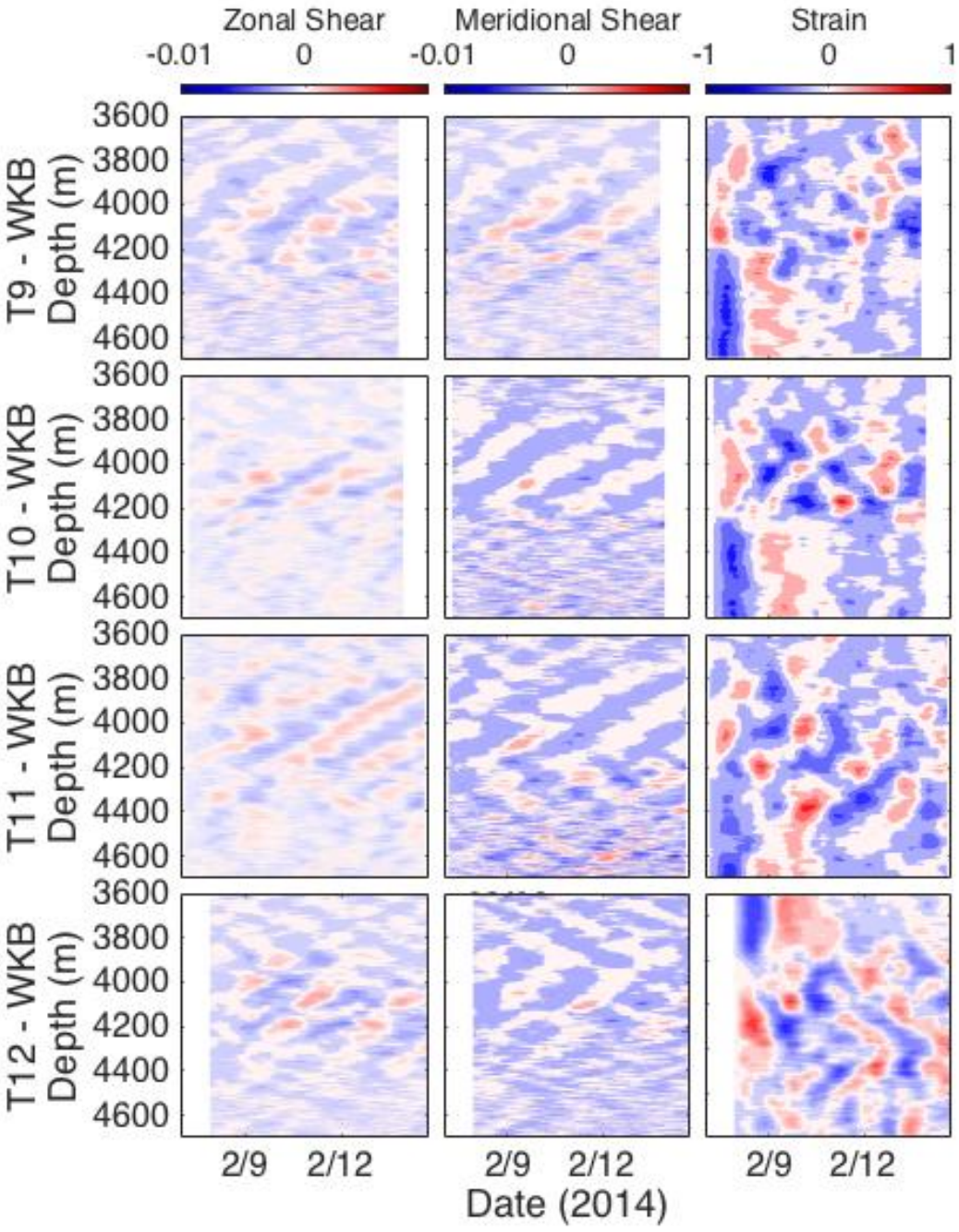

Figure 3.3: WKB-stretched-and-scaled, bandpassed, and vertically averaged zonal shear (left column), meridional shear (middle column), and strain (right column) for each of the T-moorings.

values peaking at approximately 4,200 m (Fig. 3.4, top row). Between the top of the mooring depth range (3,590 m) and 4,100 m, the potential temperature profiles are similar between the moorings. Below the interface, the moorings diverge; from coldest to warmest: T12 (black line), T9 (red line), T10 (green line), and T11 (blue line). T11 and T12 had ≈ 0.1°C difference at their maximum separation ($\approx$ 4,300 m). T12 was upstream of the sill prior to the flow being topographically accelerated, and consequently has undergone minimal mixing of AABW with intermediate waters. T11, on the other hand, was in the path of the accelerated flow and underwent mixing of AABW with the warmer intermediate waters above (see Fig. 4 in Alford et al., 2013).

T9–T11 moorings showed similar salinity profiles between 4,000 and 4,200 m with the start of the halocline at $\approx$ 4,100 m. T12 had higher salinity values within the halocline due to less mixing with the fresh AABW signal. Below the halocline T12 is fresher than T10 and T11, but is saltier than T9.

All short-term mooring N^2 profiles have a peak at the bottom of the interface, near 4200 m. The sharpest peak occurs in T11 while T12 has a spread out N^2 peak from approximately 4100 to just below 4200 m.

A depth of no motion occurred at $\approx$ 4,000 m in all moorings below which $v \gg u$, especially at T10 and T11. The velocity minimum allowed the NI signal to dominate the flow pattern and appear in raw velocity observations. Below 4,200 m accelerated flow dominated the observations.

The bottom row of Fig. 3.4 shows the long-term average at M5 (red) and the average of various NI events: October 10–19, 2012 (green); January 8–15, 2013 (blue); and December 31, 2013–January 10, 2014 (black). The long-term mooring and the short-term moorings had similar potential temperature, salinity, and density profiles with just the NIW observed at different depths. Below 4,300 m, the zonal velocity exceeded that of the short-term moorings while the meridional velocity was similar. Above 4,300 m, the long-term velocity average approached zero in both u and v. The major difference between the short-term moorings and the long-term mooring was N^2. M5 had a double peak on either side of 4200 m (the average depth of the peak of N^2 in the short-term moorings).

There were no similar water properties between the depths where the NIW is seen in the short-term moorings and the long-term mooring besides low flow speeds and high N^2 values.

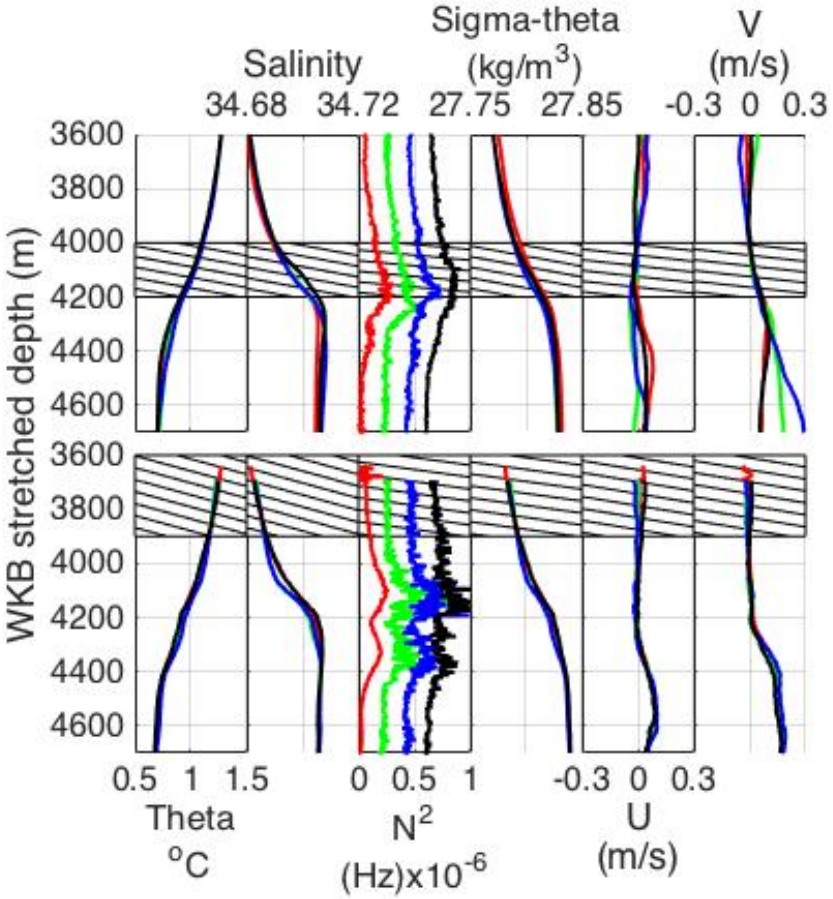

Figure 3.4: Water properties observed in the MPs at each of the moorings located around the western sill. The top panels show the short-term mooring observations averaged over the mooring lengths. The bottom panel shows the time-average of the entirety of the M5 mooring and sub-intervals of high NIW energy (as found in wavelet analysis (Fig. 3.8). From left to right: Theta, Salinity, Buoyancy Frequency, Density, u-velocity, and v-velocity. T9 (red), T10 (green), T11 (blue), and T12 (black). T9 salinity has been shifted down by 0.07 at all depths. Bottom : M5 average (red); October 10–19, 2012 (green); January 8–15, 2013 (blue); December 31, 2013–January 10, 2014 (black). M5 salinity has been shifted down by 0.0125 at all depths. Hashed area shows depths of high ACKE. Each N^2 profile has been shifted 2×10^{-6} to the right of the prior profile from red to black respectively.

3.3.2 Spectra

Spectra of shear at 4,100 m show the anticyclonic component to exceed the cyclonic component of the near inertial shear spectra at f (Fig. 3.5). This indicates a NIW signal, consistent with the velocity observations in Fig. 3.2. The Garrett-Munk spectrum is used as a reference to show a comparison of a general spectra and our observations of total energy (grey shaded region Fig. 3.5). When compared to the GM76 spectra (Fig. 3.5 dashed line; Garrett & Monk, 1972, Garrett & Munk, 1975, Cairns & Williams, 1976), the observed levels are higher than those predicted by the GM76. In addition, a M_2 peak is observed.

Depth spectrograms (Fig. 3.6) show a peak in the anticyclonic downward propagating NI shear spectra at each of the short-term moorings between 4,000 and 4,200 m. All the moorings except for T11 have a single-depth range of elevated anticyclonic shear spectra. The extent of the peak energy depth range varies between the moorings. The T12 mooring peak extends from above 4,000 m to right above 4,200 m, the widest depth range of any of the short-term moorings, potentially corresponding to the observed broader stratification peak. The depth range of elevated anticyclonic shear spectra at the T11 mooring is much narrower than at T12, corresponding to a more defined peak in N^2. In total, T11 had three peaks: 3,900, 4,100, and 4,300 m, with the upper two peaks having a statistical difference from the cyclonic shear spectra, indicating a downward propagating oscillation. The smaller, secondary peak, centered about 3,900 m, does not correspond to a local maximum in the buoyancy frequency. The primary and secondary peaks are almost purely circular motion while the third, statistically insignificant peak had a rotary coefficient of approximately 0.5. T10 had the sharpest peak in NI energy and buoyancy frequency (particularly when approaching from depth) of any of the moorings. T9 had a similar depth range of NI energy and peak buoyancy frequency to T11 and T12 and a similar observed signal. The M5 NI peak occurred above 3,900 m. The depth range of the NI signal extends above the shallowest MP observations (3,600 m), and therefore the depth extent of the NI peak at M5 is unknown. This NI peak is 200-300 m above the peaks at the short-term moorings, a similar distance to the difference of bottom depth between M5 and the other

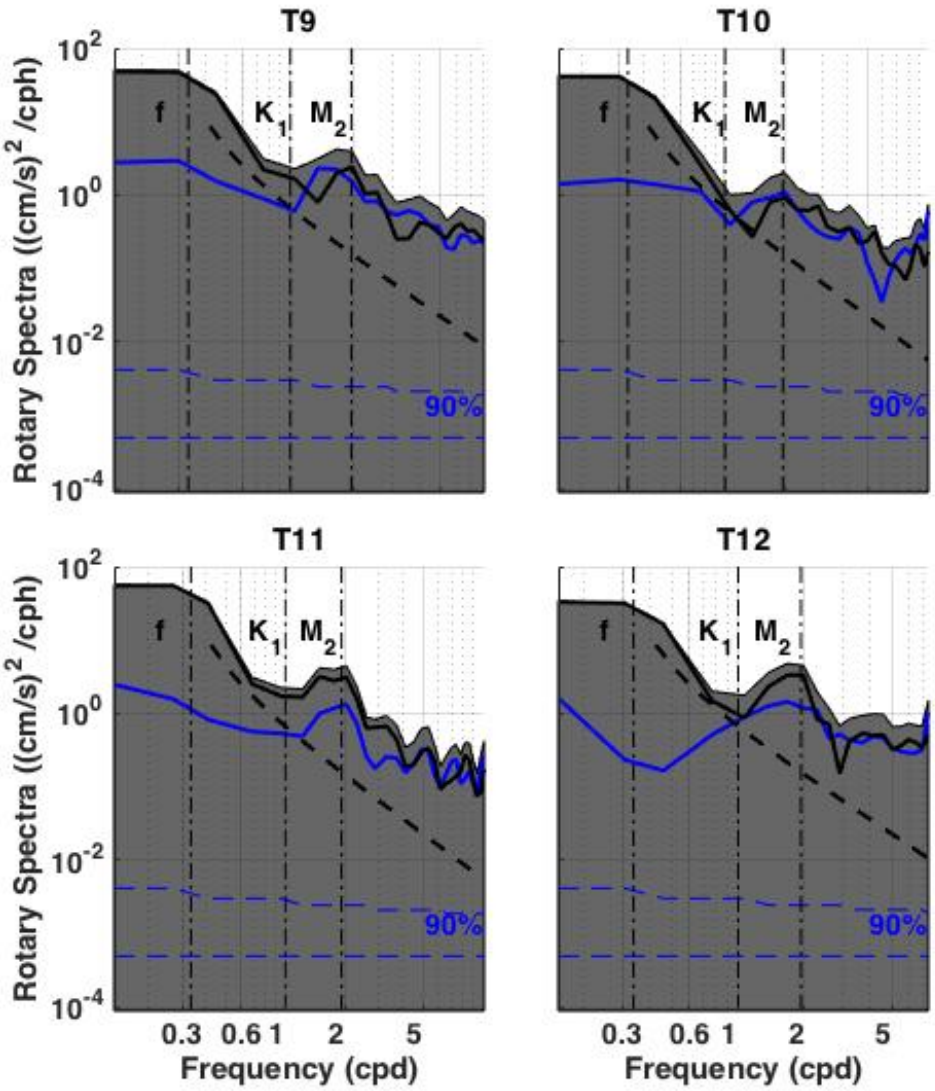

Figure 3.5: Rotary spectra of the four short-term moorings at 4,100 m depth. The total energy plotted in grey patch, clockwise, cyclonic energy (blue) plotted against the counterclockwise, anticyclonic energy (black). Black dashed line is the GM76 energy spectra and the blue dashed lines are the 90% confidence interval. Vertical dashed lines denote the inertial, K_1 and M_2 frequencies from left to right.

moorings.

It appears that the presence of NI energy corresponds to high values of buoyancy frequency agreeing with past observations (Alford & Gregg, 2001), except in the case of the T11 peaks at 3,900 and 4,300 m (Fig. 3.6). The peak at 3900 m is not statistically significant and the peak at 4300 m corresponds to an increase in dissipation, discussed further in Chapter 5. However, high values of N^2 do not necessarily indicate peaks in NIW energy. M5 had a double peak in stratification on either side of 4,200 m but did not have a corresponding NIW signal. It is possible the double peaks at M5 do not have a NI signal as M5 is considerably closer to topography at the depths of the peak in N^2 than the other moorings.

The peak of cyclonic shear spectra near f was not as concentrated in a single-depth range and the depth pattern was distinct for each mooring: T9 – a single concentrated depth band at 4300 m, T10 – a smaller signal with a peak at 4500 m, T11 – a double peak one at 4200 m and the second at 4300 m, and T12– a dispersed peak spread from 4100 to 4400 m with the absolute peak at 4300 m. M5 shows constant cyclonic shear spectra. As this record is approximately 17 months and the total time of NI events was ≈ 2 months (3.4) the signal may have been diluted. The majority of the cyclonic shear spectra peaks, near f, were below 4,200 m, but there did appear to be a local maximum in cyclonic shear, at f, which corresponded to the absolute peak in anticyclonic shear.

The difference between the anticyclonic and cyclonic shear spectra show that the anticyclonic shear spectra exceeds the cyclonic shear spectra near the inertial frequency in all 4 short-term moorings at the depths of peak anticyclonic NI shear spectra. M5 does not have a discernible difference, as neither signal is strong this is not surprising.

The last column of Fig. 3.6 is the rotary coefficient and shows depths with circular motion and corresponds to depths of peaks of the anticyclonic shear near f. In all moorings except T9, the rotary coefficient became rectilinear almost immediately below the events where anticyclonic shear $\gg$ cyclonic shear, above 4200. This abrupt transition from circular to rectilinear motion occurred at approximately the depth of the peak of the bump on the sill, the sill has a height of 4600 m and the secondary bump has a height of 4200 m. The agreement of these two depths is in accord with

Rudnick (1997) hypothesis that topography limits the downward propagation of NIWs.

3.3.3 Plane wave

The NIW (Fig 3.3) can be described with a plane wave fit to to the shear and strain in the NI frequency band. The observations are best described by the interference of a downward- and upward-propagating NIW. The upward propagating NIW has an amplitude one-quarter of the downward propagating wave, consistent with the relative magnitudes in Fig. 3.6. The two-wave solution over-plotted on the T11 WKB-stretched-and-scaled zonal shear observations is shown in Fig. 3.7. The interference pattern of the two plane waves mimics the variations in the phase lines and amplitude, whereas a single wave would have a constant slope and amplitude.

To assess the robustness of plane wave solution, the best-fit to the parameters in Eqn. 3.6 were calculated in two ways: first by treating each T-mooring separately (Table 3.1), and secondly by assuming that as the moorings are closely spaced the frequency and wavenumbers would be constant between the moorings (Table 3.2). Errors for each parameter (Table 3.3) show that the variation between best-fit plane-wave solutions for each mooring are all within error bars, except for the upward propagating wave in the zonal shear of T12.

Treating each mooring independently resulted in the upward propagating wave generally having a smaller vertical wavelength (≈ 100 m) than the downward propagating wave (≈ 200 m). The difference in wavelengths matches what would be expected of a topographically reflected wave (Eriksen, 1985). It is difficult to determine the validity of this comparison as the depth range where the NI is observed has approximately the same thickness (200 m) as the calculated vertical wavelength (200 m). The downward propagating wave was super-inertial while the upward propagating wave was sub-inertial. Local vorticity (Kunze, 1985) and the inclusion of the horizontal Coriolis term could cause the sub-inertial frequency of the upward propagating wave. The phases of the strain and zonal shear provided the propagation directions of 40°, 20°, 10°, and 0 ° true North for T9, T10, T11, and T12 respectively. All are propagating equatorward as expected. Error bars for the phases of T9–T11 overlap, Table 3.3.

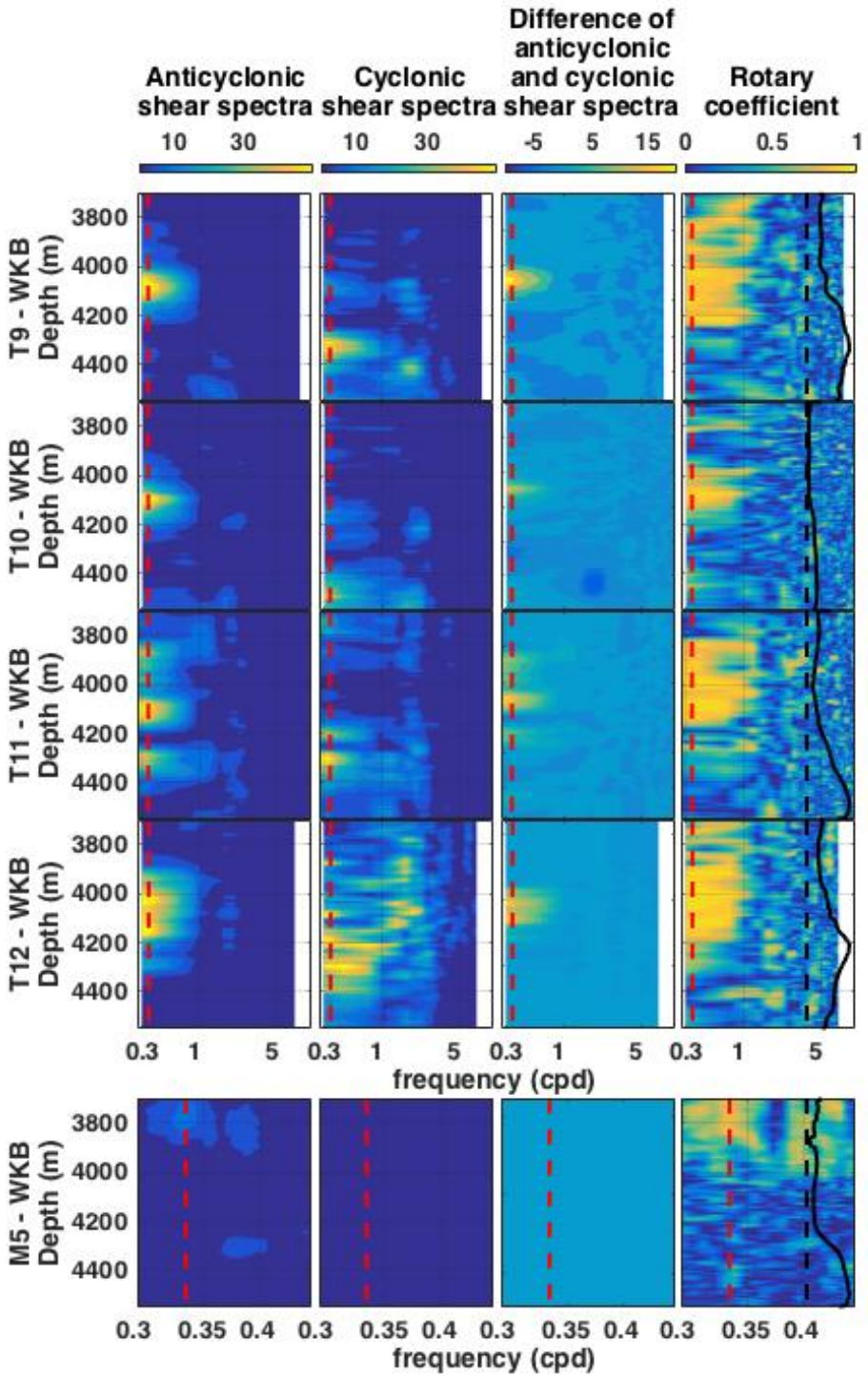

Figure 3.6: The rotary spectra plotted against depth and frequency for all five moorings in the western sill area. The red line shows the local inertial frequency. The black line is the magnitude of the velocity with the black dashed line denoting 0 m/s. A zero rotary coefficient denotes rectilinear flow while 1 is circular flow.

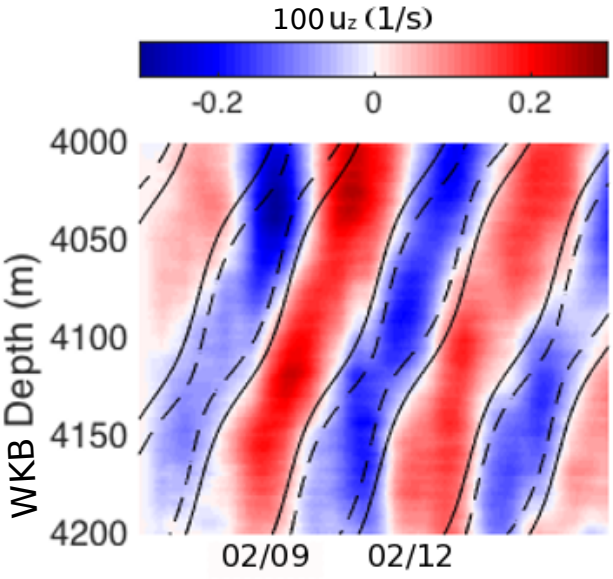

Figure 3.7: Zonal shear of the T11 mooring. The calculated plane wave solution calculated using the values in Table 3.2 is contoured on top. Dashed lines denote negative amplitude while the solid black line denotes the zero contour.

3.3.4 Wavelet analysis

Wavelet analysis of kinetic energy observations at 3,706 m depth from the M5 mooring show nine NI events occurred over the 17 month record (Fig. 3.8). These events, identified where the wavelet values are above the 95% significance level (black lines), occur 7 times: September 14–25, 2012, October 10–19, 2012, January 8–15 2013, February 25–March 3, 2013, March 15–22, 2013, September 22–28, 2013 and December 31, 2013–January 10, 2014. The lull in NI events between May and November could correspond to reduced wind events during the austral summer, 6 months prior. If the waves were formed at the surface and propagated to depth, then the average vertical propagation speed would be 22 m/day, within previous vertical propagation observations (Alford & Gregg, 2001, Alford et al., 2016, Johnston et al., 2016).

The fact that the M5 depth spectrogram (Fig. 3.6) shows a peak at the NI frequency when there only events (totalling 61 days) over a 17 month record suggests these events must be energetic

Table 3.1: Best-fit plane wave parameters when all the values are calculated individually for each short-term mooring.

Mooring	ω_d	m_d	ϕ_d	A_d	ω_u	m_u	ϕ_u	A_u
Zonal shear								
T9	0.36	0.004	110	0.17	0.32	0.009	10	0.04
T10	0.35	0.005	190	0.16	0.32	0.005	10	0.04
T11	0.34	0.004	30	0.16	0.32	0.009	50	0.04
T12	0.34	0.005	100	0.17	0.35	0.009	100	0.05
Meridional shear								
T9	0.36	0.004	200	0.17	0.34	0.009	290	0.05
T10	0.35	0.004	280	0.17	0.34	0.007	260	0.05
T11	0.35	0.004	120	0.17	0.34	0.009	280	0.05
T12	0.37	0.004	190	0.17	0.35	0.01	90	0.03
Strain								
T9	0.35	0.005	160	0.17	0.34	0.008	100	0.04
T10	0.35	0.005	170	0.17	0.34	0.007	120	0.04
T11	0.35	0.005	200	0.18	0.35	0.006	120	0.05
T12	0.35	0.005	240	0.17	0.34	0.007	110	0.05

compared to the periods of no NIW activity. From April 14–23, 2012, a periodic oscillation at the NI frequency was observed as presented in Fig. 3.9. The plane wave solution for the observed event was more uncertain than that of the T-moorings because the sampling period of the moored profiler was approximately 17.4 hours. With that caveat in mind, the best-fit for this wave was an interference pattern between two waves: the downward propagating wave with a vertical wavelength of ≈ 200 m and a frequency of 0.36 cpd (1.07f), and an upward propagating wave with a vertical wavelength of ≈ 111 m and a frequency of 0.32 cpd (1.05f). Each individual event observed in the long-term mooring are analyzed and presented in Table 3.4.

3.4 Discussion

The plane wave solutions for the moorings present a coherent picture of the wave across moorings as would be expected over small spatial scales (Alford et al., 2017). Although, some differences are

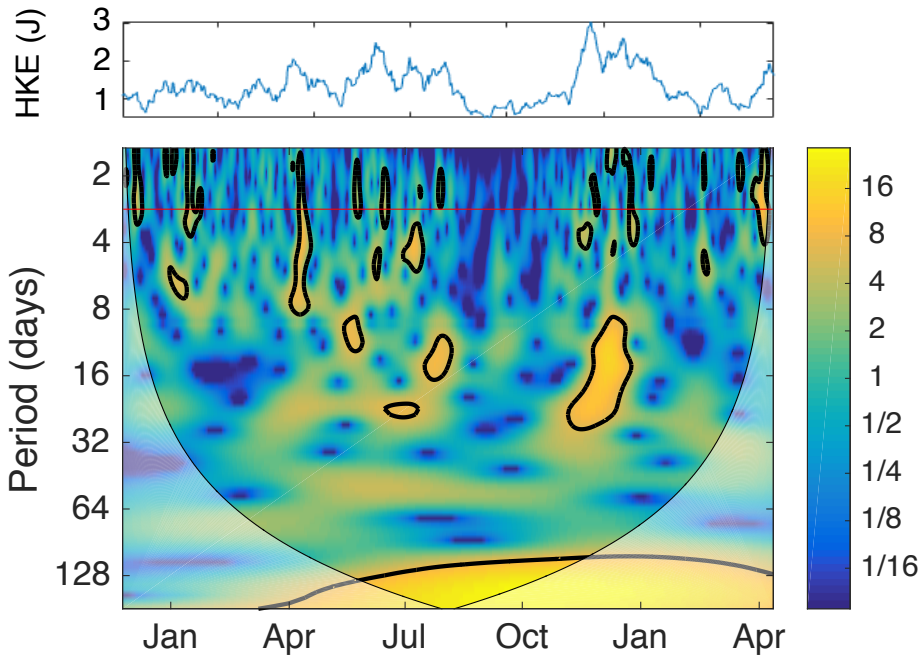

Figure 3.8: Top: The timeseries of the horizontal kinetic energy (HKE) for M5 at 3706 m. Bottom: The wavelet transform of kinetic energy at 3,706 m depth from the 17 month M5 mooring. Black contours denote events above the 95% significance level against red noise. The red horizontal line is the local inertial frequency. The light gray areas are where edge effects come into play. They are ignored for this research.

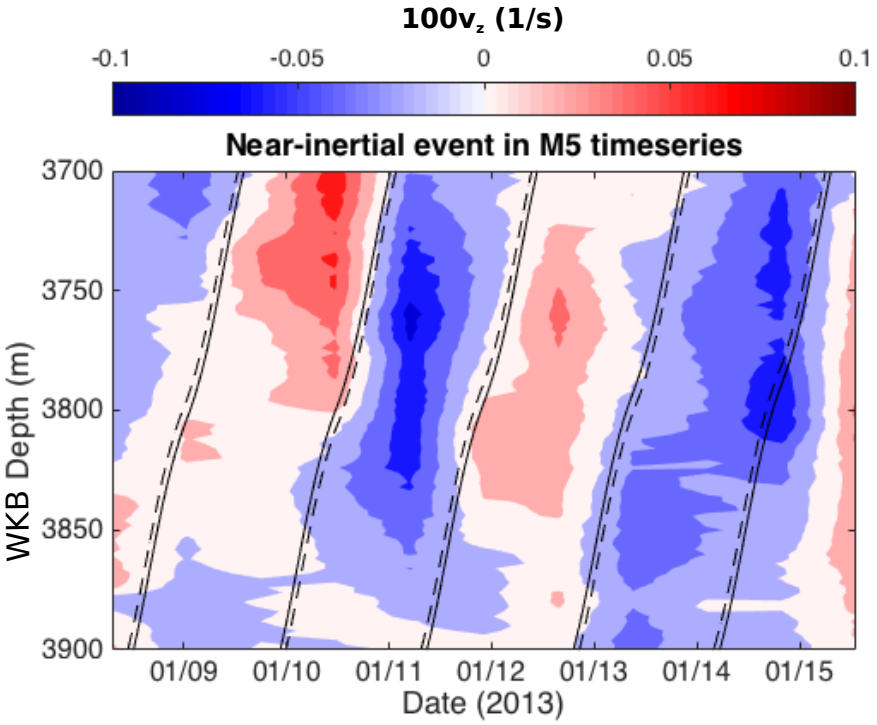

Figure 3.9: The meridional shear at M5 from January 8–15, 2013. Black solid contours are the zero contour and black dashed lines in regions of negative amplitude for the plane wave solution. The average flow has been subtracted.

Table 3.2: Best-fit plane wave parameters when frequency (ω) and vertical wavenumber (m) are held constant across all four T-moorings. The parameters for the downward and upward propagating plane waves were calculated independently.

Mooring	ω_d	m_d	ϕ_d	A_d	ω_u	m_u	ϕ_u	A_u
Zonal shear								
T9	0.36	0.005	210	0.1619	0.3	0.005	180	0.0407
T10	0.36	0.005	190	0.1619	0.3	0.005	180	0.0407
T11	0.36	0.005	190	0.1619	0.3	0.005	180	0.0407
T12	0.36	0.005	290	0.1619	0.3	0.005	180	0.0407
Meridional shear								
T9	0.36	0.004	300	0.17	0.33	0.009	270	0.05
T10	0.36	0.004	280	0.17	0.33	0.009	270	0.05
T11	0.36	0.004	280	0.17	0.33	0.009	270	0.05
T12	0.36	0.004	20	0.17	0.33	0.009	270	0.05
Strain								
T9	0.35	0.005	170	0.17	0.34	0.007	110	0.004
T10	0.35	0.005	170	0.17	0.34	0.007	120	0.004
T11	0.35	0.005	180	0.17	0.34	0.007	120	0.004
T12	0.35	0.005	220	0.17	0.34	0.007	120	0.004

observed particularly in the depth ranges of circular motion and peak anticyclonic shear spectra. This is highlighted in the rotary coefficient at T12, Fig. 3.6. T12 is the closest to the secondary peak on the sill that reaches ≈ 4200 m and it has the most abrupt transition from circular to rectilinear motion at ≈ 4200 m. The other moorings transition from circular to rectilinear motion at similar heights, but none correspond to the height of the secondary bump as well at T12. Topography is the most applicable reason for the differences.

Again the waves are cohesive in that they all propagate equatorward. This is as expected from the previous results of D'Asaro (1995), Garrett (2001), Alford (2003). Equatorward propagation is also observed in the 7 NIW events over the course of the 17-month mooring deployment. These 7 events appear to have a seasonal cycle consistent with Alford & Whitmont (2007), Silverthorne & Toole (2009). The two wave solution found in both the short-term mooring observations and the 7 events during the long-term mooring is not unique. Alford et al. (2017), Eriksen (1982), Fu (1981) observed upward

Table 3.3: The errors and calculation method for the variables used throughout this paper.

variable	average	error	method
salinity	34.6975	$\pm 2 \times 10^{-3}$	(Voet 2015)
temperature	1.2953	$\pm 5 \times 10^{-4}$	(Voet 2015)
u, v	0.0312, 0.0356	± 0.02	(Voet 2015)
r_l	1.08	± 0.15	STD
ω_d	0.36	± 0.01	t-score
ω_u	0.32	± 0.01	t-score
m_d	0.005	± 0.002	t-score
m_u	0.009	± 0.002	t-score
ϕ_d	210	± 20	t-score
ϕ_u	120	± 20	t-score
ρ	1027.8	± 0.02	STD
N^2	1.0×10^{-6}	$\pm 0.2 \times 10^{-6}$	STD
KE	NA	$\pm 3.0 \times 10^{-8}$	Error Prop.
PE	NA	± 0.04	Error Prop.

Table 3.4: The plane wave solutions for the seven NI events over the course of the 17 month record.

Date	Frequency	Vertical wavelength (m)	Direction of propagation (θ)
9/14/2012–9/25/2012	0.35	0.005	20
10/10/2012–10/19/2012	0.34	0.008	0
1/8/2013–1/15/2013	0.35	0.006	40
2/25/2013–3/3/2013	0.36	0.008	20
3/15/2013–3/22/2013	0.34	.006	10
9/22/2013–9/28/2013	0.35	.01	10
12/31/2013–1/10/2014	0.36	.005	-10

propagating NI energy and topographic reflection has been well observed: Eriksen (1985), Kunze & Sanford (1986). As the moorings in this experiment are near topography and the seafloor, reflection is not surprising.

3.4.1 Previous observations

Rudnick (1997) hypothesized that "proximity to topography prevents free inertial oscillations", which

is consistent with the theory of NIW and interactions with bottom topography (Gill, 1984). However, Rudnick's moorings consisted of Aanderra current meters at discrete depths, and hence did not give a continuous image of the transport over at depths. At 4,000 m depth his observations match ours, with both showing NI oscillations. But the greater spatial resolution between 3,600 and 4,700 m depth provided by the moored profilers showed that the NI signal peaks around 4,100 m and decays within a hundred meters either side. Voet et al. (2016) calculated transport using data from a reoccupation of the (Rudnick, 1997) mooring array. Voet et al. (2016) observations showed an inertial signal in transport that decreased with depth. However, as these moorings also had Aanderra current meters at the same discrete depths, hence the water column was again under sampled.

3.4.2 Merdional vs zonal

Across the interface, 4,000 to 4,200 m, there are differences between the meridional and zonal shear. The meridional shear has more linear phase lines and less amplitude variation than the zonal shear (Fig. 3.3). Based solely of the meridional shear, it could be argued that a single downward propagating wave best describes the observations. Whereas, the variations in phase and amplitude in zonal shear are best described by the interference between a downward and upward propagating wave. There are two possible hypotheses that might explain this asymmetry. First, the depth where the u component of velocity goes to zero lies in the middle of this NIW depth band, whereas the depth of no flow in the v component is above the interface. As a result, the weaker, upward propagating wave is not as inhibited by the background zonal flow allowing it to be more pronounced in the zonal shear observations. A second hypothesis could be that a secondary signal is introduced by eastward flow.

3.4.3 T12 - end of NI episode

Toward the end of the observation period (2014-02-13), it appears that the NIW event had passed by the T12 mooring or started to break apart (Fig. 3.3). This is most pronounced in the meridional shear. The NI event continued to be observed at the downstream moorings (T9, T10, and T11), providing

further evidence of a northward propagation direction. As increased mixing is expected with the dissipation of the NIW, (Hebert & Moum, 1994) and no such signal is observed it is suspected that the wave propagates past the T12 mooring.

3.4.4 M5 events

The long-term mooring on the sill had 7 NI events over the course of its 17-month deployment. These events occurred primarily in the months of November through June and at depths above 3900. During time periods of NI events there was a significant, at the 95% confidence level, decrease in the magnitude of u and depression of the 27.786 kg/m^3 isopycnal. Over the course of the mooring deployment the average magnitude of u was 0.0072 m/s with a 95% confidence interval of [0.0046 0.0099] m/s while during NI events the magnitude of u was 0.0044 m/s. Specifically during NI events, the displacement of the 27.786 was -14 m while the confidence interval for the entire mooring deployment was [-6.9 -2.4] m with a mean of -4.7 m. In addition, the magnitude of v was significantly increased, at the 90% confidence level. Over the course of the mooring the average magnitude of v was -0.0044 m/s with a 90% confidence interval of [-0.0064 -0.0024] m/s and during NI events the magnitude of v was -0.0067 m/s.

3.5 Summary

A deployment of 5 moorings on and around the sill at the mouth of the Western Channel of the Samoan Passage show NIWs. In the four concurrent short-term T-moorings the NI event lasts the entirety of the 7 day deployment, with the exception of at the end of the T12 deployment, with NI energy observed between 4,000 and 4,200 m. In the latter half of the week-long deployment at T12, the wave signal started to decay. As this was not observed at the T9, T10, or T11 moorings, it demonstrates a lag between the upstream and downstream moorings and corroborates our calculation of northward wave propagation.

Water column structure, specifically a peak in N^2, appears to be the main instigator for NIW observations. Above 4,000 m, minimal NI energy is observed it is suspected to be due to the low values of N^2 forcing a stretching of the vertical wavelength; between 4,000 and 4,200 m, there is a peak of the NIW energy corresponding to a peak in $N^2$and the resulting concentration of NIW; and below 4,200 m, the background flow and dominates over the NIW signal in addition to low N^2 and close topography.

A plane wave solution was fitted to the band-passed WKB stretch and scaled shears and found, between 4,000 and 4,200 m, the NIW to be comprised of an interference pattern between a downward propagating wave and a weaker, 1/4 the amplitude, upward propagating wave. A simple model using a sum of the modes, showed the upward propagating wave could not be the result of an internal reflection off the interface. However, when a realistic bottom boundary is present a nodal structure does develop at the appropriate depths showing bottom reflection may be a possible explanation of the upward propagating wave. The upward propagating NIW is more pronounced in the zonal shear observations than the meridional. A possible reason for this is that the depth with no zonal background flow is in the NIW band, whereas in the meridional the depth with no flow is above the density interface. The plane wave solutions show the NIW to be spatially coherent across all 4 moorings.

Wavelet analysis is used to determine the frequency of NIW events over the course of the long-term mooring. Seven events occurred between November and June. The same plane wave fit applied to the short-term moorings is done to analyze the long-term mooring NI energy events. This process is less accurate due to the lower sampling frequency of the long-term mooring compared to the short-term moorings. These events were found to have varying intrinsic frequency potentially indicating different origin regions. During periods of NI events there was a significant decrease in the magnitude of u, increase in the magnitude of v and depression of the 27.786 kg/m^3 isopycnal compared to the mooring average.

CHAPTER 4

Horizontal Coriolis term

4.1 Introduction

The ocean is a stratified fluid, on a rotating Earth, with momentum and buoyancy fluxes driven at the surface. These motions are described by the Navier Stokes equations. The equations describe a wide variety of phenomena on a wide range of space and time scales. Approximations must be applied as the Navier Stokes equations cannot be solved analytically. These approximations assume that the omitted terms are small when looking on the "large scale" but when looking at the "small scale" they become an issue (Marshall et al., 1997).

One such approximation is the "traditional" approximation where the radial coordinate is replaced by the earth's mean radius and the horizontal component of the Coriolis vector ($\tilde{f} = 2\Omega \cos(\phi)$, where $\Omega =$ angular velocity of rotation and $\phi =$ latitude) is neglected. Needler & LeBlond (1973) found a non-separable solution for an inviscid, incompressible, rotating fluid including $\tilde{f}$. Based on the factor of the mixed derivative, they determined it safe to neglect $\tilde{f}$ everywhere except for buoyancy waves

in weakly stratified deep layers.

This has since been found to not always be the case. The inclusion of $\tilde{f}$ has been found to be necessary including but not limited to situations with: weak stratification, bottom generated NIW, inertio-gravity waves, and atmospheric motions. Kasahara (2010) found the inclusion of the horizontal Coriolis term significantly enhances the intensity of bottom generated NIW. Gerkema & Shira (2005) found that the properties of inertio-gravity waves changed when the traditional approximation was neglected. White & Bromley (1995) found through scale analysis that the horizontal Coriolis term can attain values of up to 10% of the major terms in both planetary scale and diabatically driven tropical motions in the atmosphere. As such, the numerical prediction models developed at the Met office now include the horizontal Coriolis term (Davies et al., 2005).

NIW have been observed in many locations (Alford et al., 2007, Webster, 1968) including: the deep ocean (Leaman & Sanford, 1975, Fu, 1981, Gill, 1984, Alford et al., 2012), where N^2 is low, and near the equator, at low latitudes. As NIW propagate equatorward (Alford et al., 2012), they become super-inertial (Gill, 1984) and for downward propagating waves, the ray angles generally steepen while propagating to depth (Garrett, 2001). Previous observations in the Samoan Passage (Alford et al., 2013) have been found to have a NIW signal in the deep and bottom water transport (Roemmich et al., 1996, Voet et al., 2015).

In this chapter NIW observations at the sill of the western channel of the Samoan Passage are used as a case study of why the horizontal component of the Coriolis vector needs to be included in calculations of NIW in low-latitude, low-stratification environments. Section 2 calculates the equations for the: dispersion relation, effective frequency, horizontal wavenumber, group speed and ray tracing for both the inclusion and exclusion of the horizontal component of the Coriolis vector. Section 3 looks a the values found, using the equations calculated in Section 2, specifically for the NIW observed in the Samoan Passage. Section 4 generalizes the percent difference between the dispersion relation and group speed when including and neglecting $\tilde{f}$ for a wide range of latitudes and N. Section 5 summarizes our findings and explores the importance of not always neglecting $\tilde{f}$. Appendix A includes the error calculations for the calculated quantities. Finally, appendix B describes

the method used to calculate the percent difference for the dispersion relation, and group speeds between including and neglecting $\tilde{f}$ as a function of latitude and N.

4.2 Equations

4.2.1 Dispersion relation

Start with the incompressible Boussinesq equations on the f-plane, including the horizontal Coriolis term:

$$\frac{\partial u}{\partial t} - fv + \tilde{f}w = -\frac{1}{\rho_0}\frac{\partial p}{\partial x} \tag{4.1}$$

$$\frac{\partial v}{\partial t} + fu = \frac{1}{\rho_0}\frac{\partial p}{\partial y} \tag{4.2}$$

$$\frac{\partial w}{\partial t} - \tilde{f}u = -\frac{1}{\rho_0}\frac{\partial p}{\partial z} - \frac{g\rho}{\rho_0} \tag{4.3}$$

$$\frac{\partial u}{\partial x} + \frac{\partial v}{\partial y} + \frac{\partial w}{\partial z} = 0 \tag{4.4}$$

$$\frac{\partial p}{\partial z} = -g\rho' \tag{4.5}$$

$$\frac{\partial p'}{\partial t} = \frac{\rho_0}{g}N^2 w \tag{4.6}$$

where $\tilde{\Omega} = (0, \cos\phi, \sin\phi)$ which can be used for $2\Omega = (0, \tilde{f}, f)$ where $\tilde{f} = 2\Omega\cos\phi$ and $f = 2\Omega\sin\phi$ and $\Omega =$ the earth's angular velocity (7.292×10^{-5} rad/s), $\tilde{u} = (u, v, w)$ the perturbation velocities, $p =$ pressure, $\rho_0 =$ background density, $\rho =$ perturbation density and $N =$ buoyancy frequency.

A single equation can be derived for w from these equations. Start by taking $\frac{\partial}{\partial y}$(Eqn. 4.3) and subtracting $\frac{\partial}{\partial z}$(Eqn. 4.2) to get:

$$\frac{\partial}{\partial t}\left(\frac{\partial w}{\partial y} - \frac{\partial v}{\partial z}\right) = \left(\tilde{f}\frac{\partial}{\partial y} + f\frac{\partial}{\partial z}\right)u - \frac{g}{\rho}\frac{\partial p'}{\partial y}. \tag{4.7}$$

A similar result can be found by taking $\frac{\partial}{\partial z}$(Eqn. 4.1) and subtracting $\frac{\partial}{\partial x}$(Eqn. 4.3) and then substituting

$-\frac{\partial v}{\partial y} = \frac{\partial u}{\partial x} + \frac{\partial w}{\partial z}$ from the continuity equation and taking $\frac{\partial}{\partial x}$(Eqn. 4.2) and subtracting $\frac{\partial}{\partial y}$(Eqn. 4.1) to get:

$$\frac{\partial}{\partial t}\left(\frac{\partial u}{\partial z} - \frac{\partial w}{\partial x}\right) = \left(\tilde{f}\frac{\partial}{\partial y} + f\frac{\partial}{\partial z}\right)v + \frac{g}{\rho}\frac{\partial p'}{\partial x} \tag{4.8}$$

and

$$\frac{\partial}{\partial t}\left(\frac{\partial v}{\partial x} - \frac{\partial u}{\partial y}\right) = \left(\tilde{f}\frac{\partial}{\partial y} + f\frac{\partial}{\partial z}\right)w - \tilde{f}v. \tag{4.9}$$

Then by taking $\frac{\partial^2}{\partial y \partial t}$ of Eqn. 4.7 and subtracting $\frac{\partial^2}{\partial x \partial t}$ of Eqn. 4.8 and use substitution of the continuity equation (Eqn. 4.4) and Eqn. 4.9 an equation solely in w is derived:

$$\frac{\partial^2}{\partial t^2}\bigtriangledown^2 w + (\tilde{f}\cdot\bigtriangledown)^2 w + N^2\bigtriangledown_h^2 w = 0, \tag{4.10}$$

where $\tilde{f} = (0,\tilde{f},f)$, $\bigtriangledown_h^2 = \frac{\partial^2}{\partial x^2} + \frac{\partial^2}{\partial y^2}$, and $\bigtriangledown = \frac{\partial^2}{\partial x^2} + \frac{\partial^2}{\partial y^2} + \frac{\partial^2}{\partial z^2}$.

Neglecting the horizontal Coriolis term

The application of the traditional approximation ($\tilde{f} = 0$) to Eqn. 4.10 and the substitution of a solution of $w = e^{i(kx+ly+mz-\omega t)}$ gives the dispersion relation:

$$\omega^2 = \frac{N^2(k^2+l^2)+f^2m^2}{k^2+l^2+m^2}. \tag{4.11}$$

Including the horizontal Coriolis term

If the traditional approximation is not applied and solutions of the form $w = e^{i(kx+ly+mz-\omega t)}$ are assumed, the dispersion relation is found to be:

$$\tilde{\omega}^2 = \frac{N^2(k^2+l^2)+(\tilde{f}l+fm)^2}{k^2+l^2+m^2}. \tag{4.12}$$

4.2.2 Group speeds

The group speeds can be found by taking the derivative with respect to each wavenumber:

Neglecting the horizontal Coriolis term

$$c_{gx} = \frac{\partial \omega}{\partial k} = \frac{kN^2}{m^2\sqrt{f^2 + \frac{N^2K_H^2}{m^2}}} \tag{4.13}$$

$$c_{gy} = \frac{\partial \omega}{\partial l} = \frac{lN^2}{m^2\sqrt{f^2 + \frac{N^2K_H^2}{m^2}}} \tag{4.14}$$

$$c_{gz} = \frac{\partial \omega}{\partial m} = \frac{N^2K_H^2}{m^3\sqrt{f^2 + \frac{N^2K_H^2}{m^2}}} \tag{4.15}$$

where $k_H = \mathrm{sqrt}(k^2 + l^2.)$.

Including the horizontal Coriolis term

$$\tilde{c}_{gx} = \frac{\partial \tilde{\omega}}{\partial k} = \frac{k(N^2 - \tilde{\omega}^2)}{\tilde{\omega}m^2} \tag{4.16}$$

$$\tilde{c}_{gy} = \frac{\partial \tilde{\omega}}{\partial l} = \frac{l(N^2 + \tilde{f}^2 - \tilde{\omega}^2) + f\tilde{f}m}{\tilde{\omega}m^2} \tag{4.17}$$

$$\tilde{c}_{gz} = \frac{\partial \tilde{\omega}}{\partial m} = \frac{\tilde{f}fl + m(f^2 - \tilde{\omega}^2)}{\tilde{\omega}m^2}. \tag{4.18}$$

4.2.3 Effective frequency (f_{eff})

The observed frequency differs from the intrinsic frequency because of Doppler shift by the mean currents and shifting by the background vorticity. The method described in Alford & Gregg (2001) is followed to compute the intrinsic frequency of the observed NIW using quantities observed in the data set. The background vorticity is taken into consideration by using the effective Coriolis frequency (f_{eff}) (Kunze, 1985),

$$f_{eff} = f_0 + \frac{\zeta}{2} \tag{4.19}$$

and then Doppler shifting by the mean currents (Alford & Gregg, 2001)

$$\omega - \omega_I = |K_H||U|\cos(\theta - \alpha). \tag{4.20}$$

The variable r_I is calculated to compare the ratio of energy in the vertical to energy in the horizontal and calculate the waves intrinsic frequency ($\omega_I = r_I f_{eff}$).

Where r_I describes the ratio of KE to PE, is calculated using:

$$r_I = \sqrt{\frac{\frac{KE}{PE} + 1}{\frac{KE}{PE} - 1}}. \tag{4.21}$$

The mean value of r_I over 4000-4150 m is used for r_l with an error of one standard deviation. Since the value for the horizontal wavenumber is unknown, Eqn. 4.20 is solved for K_H^2:

$$K_H^2 = \frac{\omega^2 - \omega_I^2}{U^2\cos^2(\theta - \alpha)}, \tag{4.22}$$

and substitute this into the dispersion relation, solving for f_{eff}. As we are working with NIW, it is possible to simplify the equation using $K^2 = m^2$ because $K_H^2 << m^2$.

Neglecting the horizontal Coriolis term

Start with the dispersion relation:

$$\omega_I^2 = \frac{N^2 K_H^2}{m^2} + f_{eff}^2 \tag{4.23}$$

and substitute Eqn. 4.22 to eliminate K_H:

$$r_I^2 f_{eff}^2 = \frac{N^2}{m^2}\frac{(\omega^2 - r_I^2 f_{eff}^2)}{U^2\cos^2(\theta - \alpha)} + f_{eff}^2. \tag{4.24}$$

Finally, solve for f_{eff}:

$$f_{eff} = \frac{N\omega}{\sqrt{(r_I^2 - 1)m^2U^2\cos^2(\theta - \alpha) + N^2 r_I^2}}. \tag{4.25}$$

Including the horizontal Coriolis term

To solve for the effective frequency, without applying the traditional approximation, substitute Eqn. 4.22 into the non-traditional dispersion relation:

$$\tilde{\omega}^2 = \frac{N^2K_H^2 + (\tilde{f}l + f_{eff}m)^2}{m^2} = \frac{N^2K_H^2 + \tilde{f}^2l^2}{m^2} + \frac{2\tilde{f}f_{eff}l}{m} + f_{eff}^2 \tag{4.26}$$

along with the definition of the intrinsic frequency to get:

$$r_I^2 f_{eff}^2 = f_{eff}^2 + \frac{2f_{eff}\tilde{f}}{m}\frac{(\omega - r_I f_{eff})}{\sqrt{2}G} + \frac{\tilde{f}^2}{m^2}\frac{(\omega^2 - r_I^2 f_{eff}^2)}{2G^2} + \frac{N^2}{m^2}\frac{(\omega^2 - r_I^2 f_{eff}^2)}{G^2}, \tag{4.27}$$

where $G = |U|\cos(\theta - \alpha)$. After rearranging this equation into standard form:

$$\begin{aligned} 0 = f_{eff}^2 \left((1 - r_I^2) - \frac{2\tilde{f}r_I}{\sqrt{2}mG} - \frac{\tilde{f}^2 r_I^2}{2m^2G^2} - \frac{N^2 r_I^2}{m^2G^2} \right) \\ + f_{eff} \left(\frac{2\tilde{f}\omega}{\sqrt{2}mG} \right) \\ + \left(\frac{\tilde{f}^2\omega^2}{2m^2G^2} + \frac{N^2\omega^2}{m^2G^2} \right) \end{aligned} \tag{4.28}$$

it is possible to calculate the f_{eff} using the quadratic formula:

$$f_{eff} = \frac{-B \pm \sqrt{B^2 - 4AC}}{2A} \tag{4.29}$$

where:

$$A = 2m^2G^2(1 - r_I^2) - r_I^2(2N^2 + \tilde{f}^2) - 2\sqrt{2}r_I mG\tilde{f}$$

$$B = 2\sqrt{2}\tilde{f}\omega mG$$

$$C = \omega^2(2N^2 + \tilde{f}^2).$$

4.2.4 Horizontal wavenumber

The horizontal wavenumber (K_H) can be found by substituting in the calculated value of the effective frequency into the dispersion relation:

Neglecting the horizontal Coriolis term

When $\tilde{f}$ is neglected and $\omega_I = r_I f_{eff}$ has been substituted in, an equation for k_H dependent on known values is derived:

$$K_H = \sqrt{k^2 + l^2} = \sqrt{\frac{m^2(\omega_I^2 - f_{eff}^2)}{N^2}}. \tag{4.30}$$

Including the horizontal Coriolis term

When $\tilde{f}$ is included and the dispersion relation is rearranged in standard form an equation:

$$0 = k_H^2 \left(N^2 + \frac{\tilde{f}^2}{2} \right) + k_H \left(\sqrt{2} f_{eff} \tilde{f} m \right) + m^2 (f_{eff}^2 - \tilde{\omega_I}^2), \tag{4.31}$$

is derived, where the quadratic formula can be used to calculate a value for k_H:

$$A = N^2 + \frac{\tilde{f}^2}{2}, \tag{4.32}$$

$$B = \sqrt{2} f_{eff} \tilde{f} m \tag{4.33}$$

and

$$C = m^2 (f_{eff}^2 - \omega_I^2). \tag{4.34}$$

4.2.5 Ray Tracing

It is possible to determine the time elapsed between wave formation and its observation at the moorings by integrating the ray equations (Lighthill, 1978) backward in time. We use Wentzel-

Kramers-Brillouin (WKB) stretched depths so as to account for changes in the vertical wavenumber, due to buoyancy fluctuations (Leaman & Sanford, 1975, Alford & Gregg, 2001). f_{eff} is used to account for the background vorticity. As a result, only l will have refractive changes, due to the β effect. It is incorrect to assume constant vorticity, but as a better assessment is impossible with our data set, it is necessary. Applying these assumptions gives the reduced ray tracing equations:

$$\begin{aligned} \frac{dx}{dt} &= c_{gx} + |U|\cos(\alpha) \\ \frac{dy}{dt} &= c_{gy} + |U|\sin(\alpha) \\ \frac{dz'}{dt} &= c_{gz'} \\ \frac{dl}{dt} &= \frac{\partial \omega_t}{\partial y} = \frac{f_{eff}}{\omega_t}\beta \end{aligned} \tag{4.35}$$

Where:

U = the magnitude of the background velocity, α = the direction of the background flow, and $c_{gx,gy,gz}$ = the group speed in the zonal, meridional and vertical directions respectively. A Fourth Order Runge-Kutta method is used to calculate the group speed and $\frac{dl}{dt}$ for each time-step.

4.3 Case study: Samoan Passage

Four concurrent 7-day moorings (Fig. 4.1B), located around the western sill, observed a NIW between depths of 4000 and 4200 m (Fig. 3.7). Moorings were equipped with moored profilers traveling between 3600 and 4800 m. For a more detailed description of mooring instrumentation refer to Voet et al. (2015) and the Data and section in Chapter 2. Time and depth averaged N was $0.001\,s^{-1}$ with a peak at approximately 4200 m reaching values up to $1.8 \times 10^{-3}\,s^{-1}$, Fig 4.1C. A plane wave solution was fit to the observed shear and strain. Values were found for the vertical wavelength, propagation direction, amplitude, and observed frequency 4.2. The observed plane wave solution was comprised of two waves: one downward propagating and one 1/4 the amplitude upward propagating wave (Fig. 3.7). Unless otherwise noted, values describing the downward propagating wave will be used.

	Amplitude (A)	Vertical wavenumber (m) [1/m]	Frequency (ω) [1/day]	Propagation direction (θ) [° from true North]
Downward	0.16	0.005	0.36	10
Upward	0.04	0.009	0.32	60

Table 4.1: The values calculated by applying a plane wave fit to NIW observations at all 4 short term moorings (T9 - T12).

r_I	1.08	1.23	1.01
ω_I (s^{-1})	4.5×10^{-6}	5.535×10^{-6}	4.185×10^{-6}
ω_0 (s^{-1})	4.1667×10^{-6}	4.1667×10^{-6}	4.1667×10^{-6}
f_{eff} (s^{-1})	3.865×10^{-6}	3.865×10^{-6}	3.865×10^{-6}
$1/k_H$ (km)	127	72	365
m (1/m)	0.005	0.005	0.005
ψ (1/s)	0.0458	0.0458	0.0458
z_0 (m)	4000	4000	4000
latitude	9°40.65′S	9°40.65′S	9°40.65′S
longitude	169°50.57′W	169°50.57′W	169°50.57′W
α (° true North)	0	0	0
θ (° true North)	20	20	20
|U| (m/s)	0.003	0.003	0.003

Table 4.2: The values used in the ray tracing calculations from 4 concurrent short-term moorngs (T9-T12).

The average flow speed (|U|) and direction (α) were calculated by taking the time average of the velocity observations between 4000 and 4200 m at all four moorings. The average depth profile of N (Fig. 4.1C) was found by temporally averaging all moored profiler profiles from the 4 moorings at depths between 3600 and 4800 m. N^2 at other depths is the time-average of all full depth conductivity, temperature, and depth (CTD) profiles in the western sill region (Table 4.3).

Latitude (S)	Longitude	Max depth (m)
9°37.5′	169°48.8′	4763
9°35.4′	169°45.7′	4764
9°36.1′	169°49.0′	4798
9°37.4′	169°54.3′	4288
9°40.2′	169°48.7′	4706
9°40.1′	169°50.3′	4956

Table 4.3: Location, and maximum depth of the full-depth CTD profiles around the western sill.

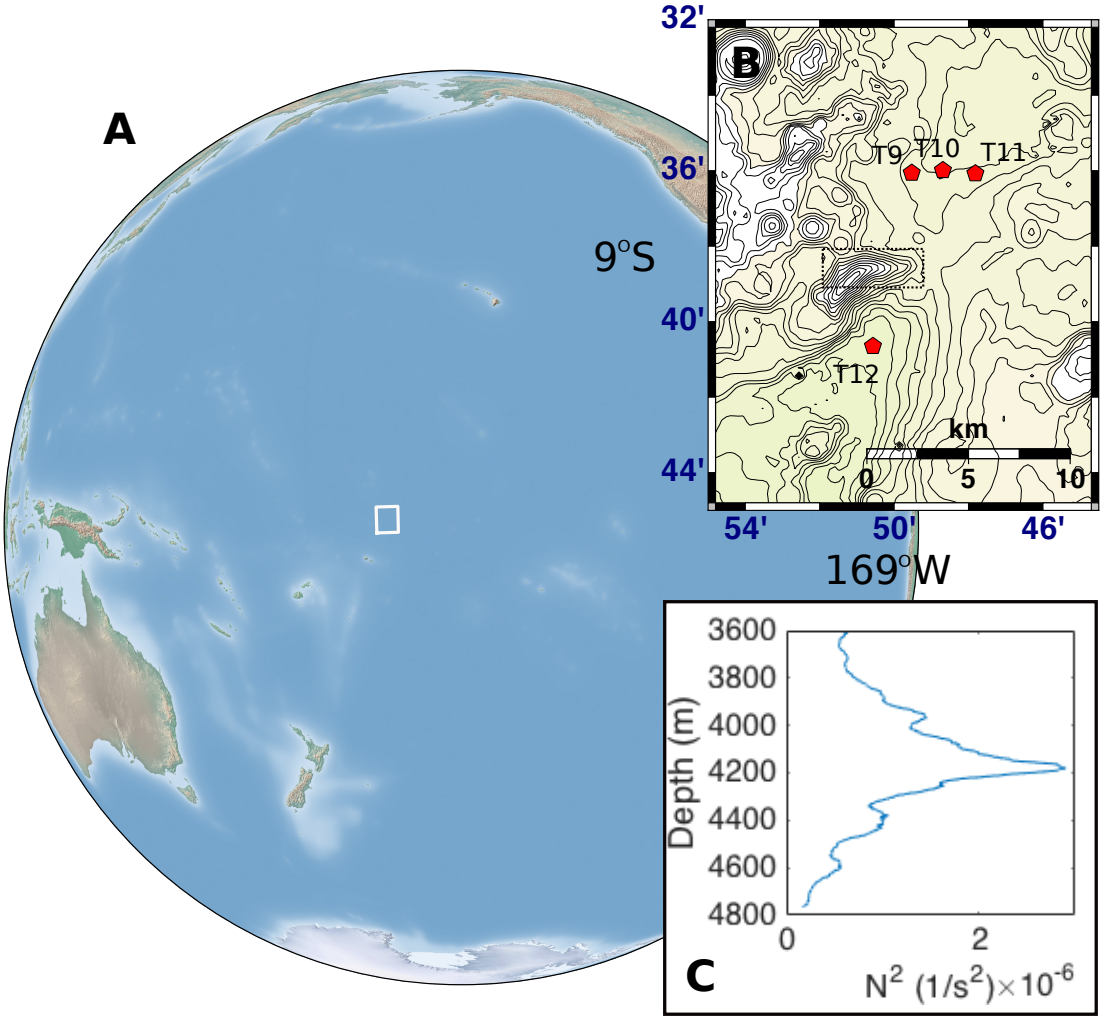

Figure 4.1: A) Global location of the Samoan Passage. B) The four 7-day moorings situated around the sill at the entrance to the western channel. C) a time averaged plot of N^2 vs depth, time average of all four moorings.

4.3.1 Dispersion relation

The importance of the horizontal Coriolis term can be assessed in the calculation of the dispersion relation by looking at the percent difference between the dispersion relation including the horizontal Coriolis term and the dispersion relation neglecting the horizontal Coriolis term:

$$\Delta = \frac{\tilde{\omega}^2 - \omega^2}{\omega^2}. \tag{4.36}$$

After substituting in Eqns. 4.11 and 4.12 an equation for the percent difference is found:

$$\Delta_{\omega^2} = \frac{\tilde{f}^2 l^2 + f\tilde{f} l m}{N^2 K_H^2 + f^2 m^2}. \tag{4.37}$$

Δ_{ω^2} is plotted against depth, where Δ_{ω^2} is calculated using a time averaged, depth varying N^2 at 9.5°S and holding all other values constant: $m = 0.005\,m^{-1}$ and $K_h = 4.7 \times 10^{-6}\,m^{-1}$ (Fig. 4.2). As N^2 increases from 3600 to 4200 m, the difference between the two equations decreases. Moreover, at minimum stratification the difference is maximized. The average difference ranged between 0.004% and 0.0052% with an average value of 0.005%. The inclusion of $\tilde{f}$ is determined to not be important in calculating ω^2 for the Samoan Passage.

4.3.2 Group speed

Substituting the values from the planewave solution into Eqns. 4.17 and 4.18 gives an initial horizontal group speed of 0.003 m/s and an initial vertical group speed of 0.7 m/day. When $\tilde{f}$ is neglected, Eqns. 4.14 and 4.15, the group speeds are found to be 0.007 m/s and 1.1 m/day respectively.

The relative error on the group speed is calculated using the same basic equation for the percent difference used for ω^2 except now using group speeds:

$$\Delta_{c_{gz}} = \frac{\tilde{c}_{gz} - c_{gz}}{c_{gz}} \tag{4.38}$$

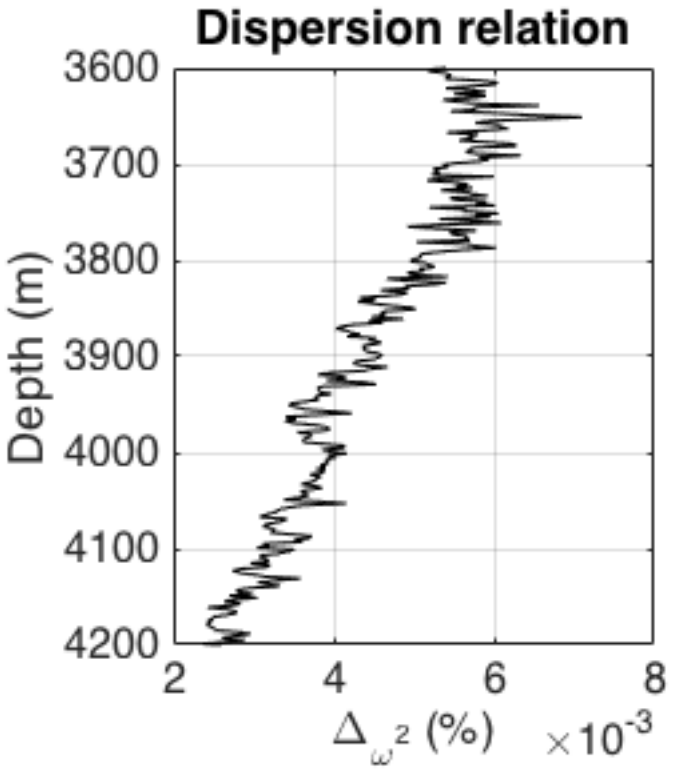

Figure 4.2: A plot of $\Delta = \frac{\tilde{\omega}^2 - \omega^2}{\omega^2}$ versus depth with depth varying N^2.

and

$$\Delta_{c_{gx}} = \frac{\tilde{c}_{gy} - c_{gy}}{c_{gy}}. \tag{4.39}$$

In Fig. 4.3 and 4.4 the meridional group speed (c_{gy}) and vertical group speed (c_{gz}), calculated using the depth varying N^2 values observed at the mooring site and holding m, k_H, and latitude constant, are plotted. For $\Delta_{c_{gy}}$ the differences in the two equations vary between 3 and 20% and by an average of $\approx 10\%$. It is apparent that there is a large difference in c_{gy} when $\tilde{f}$ is included compared to when it is neglected. The $\Delta_{c_{gz}}$ does not have as large of a percent difference as $\Delta_{c_{gy}}$ but can reach as high as 10% in regions of low N. Over these depth ranges there is a 5% difference between c_{gz} and $\tilde{c}_{gz}$. It can be concluded that in the Samoan Passage, it is important to include $\tilde{f}$ in the calculations of the group speeds.

4.3.3 f_{eff}

When f_{eff} is calculated with the traditional approximation (Eqn. 4.25) it is found that $f_{eff} = 0.33$ cpd (0.99f). When the traditional approximation is not applied (Eqn. 4.29), $f_{eff} = 0.33$ cpd (0.99f).

The differences between the effective frequency equations can be calculated using:

$$\Delta_{f_{eff}} = \frac{\tilde{f}_{eff} - f_{eff}}{f_{eff}}. \tag{4.40}$$

The differences between the effective frequency calculated with the horizontal Coriolis term and those without are negligible for the observed values of N (Fig. 4.5). In the Samoan Passage, there is no significant difference between the two calculations, beyond a less complicated calculation of f_{eff} when neglecting $\tilde{f}$.

The intrinsic frequency can be calculated using:

$$\omega_I = r_I f_{eff} \tag{4.41}$$

giving a value of $0.36 \pm 0.06\,s^{-1}$(1.06±0.15f). If the intrinsic frequency is used to calculate the latitude

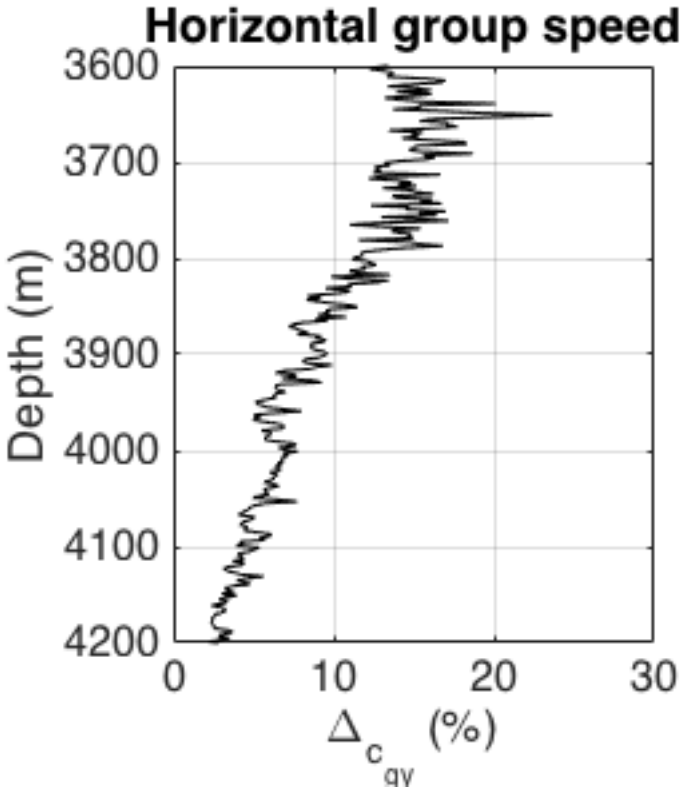

Figure 4.3: A plot of $\Delta = \frac{\tilde{c}_{gy} - c_{gy}}{c_{gy}}$ versus depth with depth varying N^2.

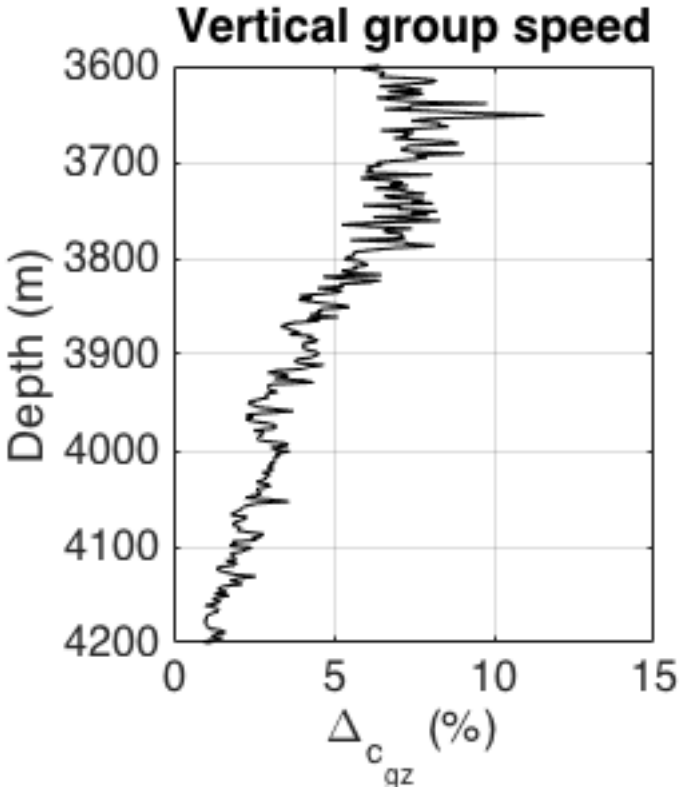

Figure 4.4: A plot of $\Delta = \frac{\tilde{c}_{gz} - c_{gz}}{c_{gz}}$ versus depth with depth varying N^2.

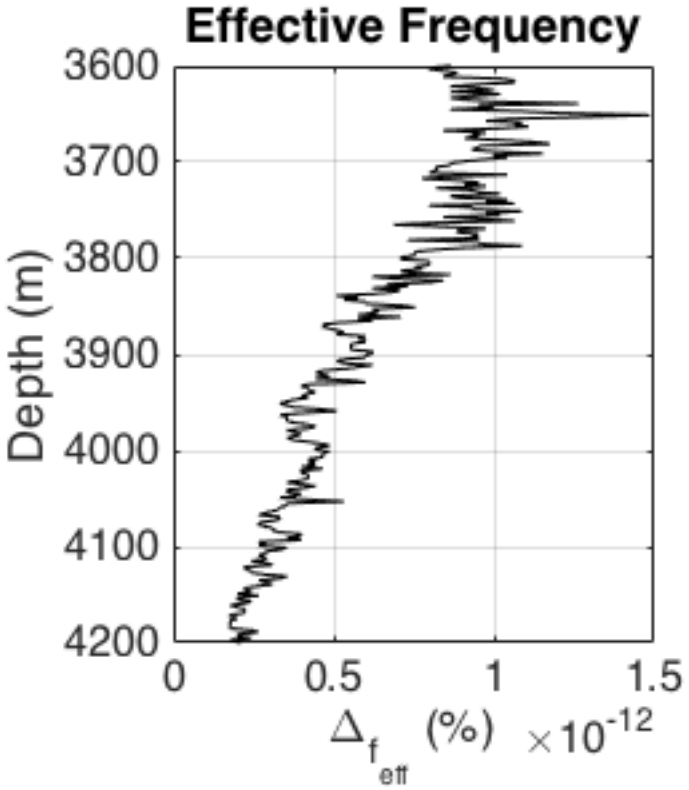

Figure 4.5: A plot of $\Delta = \frac{\tilde{f}_{eff} - f_{eff}}{f_{eff}}$ versus depth with depth varying N^2.

of origin it is found that the wave originates at 10°24′S with an upper bound of 12°06′S and a lower bound of 8°42′S.

4.3.4 Horizontal wavenumber

Substituting known values into Eqns. 4.30 and 4.31 gives $K_H = 7.87 \times 10^{-6}$ cpm, a horizontal wavelength of ≈ 127 km for both equations. There is no discernible difference between the two observed values.

The difference between the horizontal wavenumber with the traditional approximation and the horizontal wavenumber without the traditional approximation is calculated using:

$$\Delta_{K_H} = \frac{\tilde{K}_H - K_H}{K_H} \tag{4.42}$$

When the latitude is held constant if is found that the depth varying N^2 does not affect the percent difference of the horizontal wavelength (Fig. 4.6). At low values of N the percent difference can reach values of $\approx 0.18\%$, at the highest values of N a percent difference of $\approx 0.12\%$ is seen. The average percent difference across the depth range lies a little below 0.15%. As there is no discernible difference, it is easier to calculate the horizontal wavenumber neglecting $\tilde{f}$ as that is the simpler equation.

4.3.5 Ray Tracing

Using a starting position for the ray tracing to be the latitude and longitude of the T12 mooring (9°40.65′S, 169°50.57′W) and start time of February 14, 2014 at 19:00 GST. It is from this starting point that the NIW is propagated back both in time and space (Figs. 4.7 and 4.10).

Constant vorticity and mean flow are assumed throughout the water column. This is a necessary but not necessarily valid assumption, simply due to the extent of the ray tracing in depth, time and space. Two solutions are presented: a ray tracing from 4000 m up to 3600 m, depths with good data

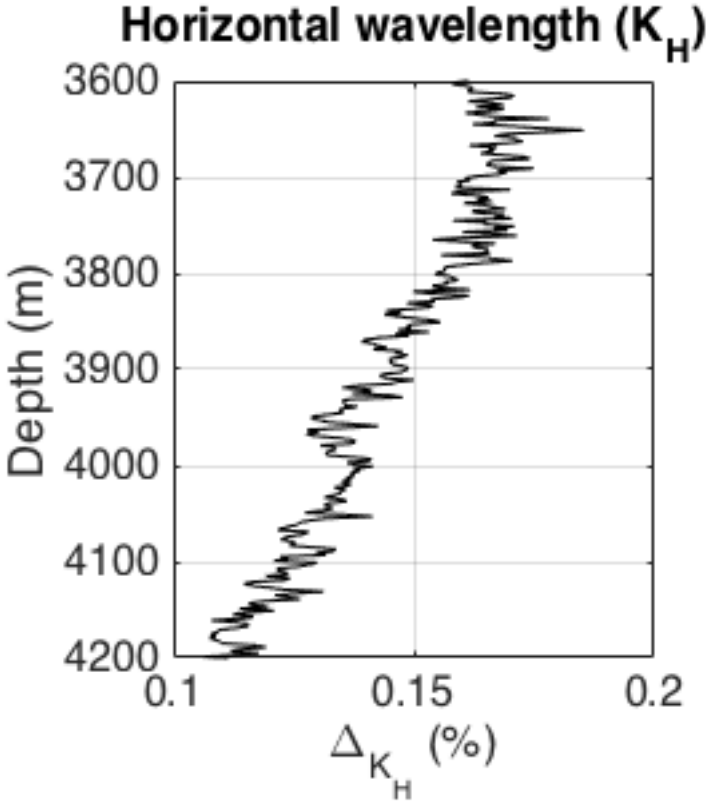

Figure 4.6: A plot of $\Delta = \frac{\check{K}_H - K_H}{K_H}$ versus depth with depth varying N^2.

coverage, and a ray tracing to the surface, because wind events are a common, but not the only, generation mechanism.

Ray tracing - up to 3600 m

The observations were comprised of a two-wave solution for the near-inertial signal. The ray tracing from 4000 to 3600 m shows a possible path for the upward propagating component. As such values used in the ray tracing equations were those found to describe the downward propagating wave (Table 4.1).

The time-averaged values of N are plotted against depth in Fig. 4.7. When ray tracing is used to find the path from 400 m to 3600 m, the differences between the two solutions, including $\tilde{f}$ and neglecting $\tilde{f}$, are apparent at 3600 m (Fig. 4.8). The solution including $\tilde{f}$ reaches 3600 m on November 17, 2013 after 89.1 days while the solution neglecting $\tilde{f}$ reaches 3600 m on November 3, 2013 after 103.9 days. There is already a difference of 14.8 days. This shows the inclusion of the horizontal Coriolis term increases the vertical velocity, as previously shown. This translates into a difference between expected latitudes: 10°12′S with $\tilde{f}$ and 10°24′S without $\tilde{f}$. As expected from Figs. 4.6 and 4.5, there is no apparent difference between the calculations for horizontal wavelength and the ratio of the intrinsic frequency to the effective frequency (ω_I/f_{eff}).

Fig. 4.9 shows the locations of the NIW using the two methods, the results are for the inclusion of $\tilde{f}$ (10°12′S, 170°54′W) and neglecting $\tilde{f}$ (10°24′S, 170°48′W) separated by a distance of 25 km.

Ray tracing - to the surface

As the wave propagates up to the surface there is a difference between the solution including $\tilde{f}$ and that excluding $\tilde{f}$. The ray tracing solution with the inclusion of $\tilde{f}$ reaches the surface on July 8, 2013 after 191.1 days, while the ray tracing neglecting $\tilde{f}$ reaches the surface on June 26, 2013 after 203.7 days (Fig. 4.10). This is a difference of 12.6 days. The calculation with $\tilde{f}$ reaches the surface at (13°S, 174.1°W) and the calculation neglecting $\tilde{f}$ at (13.2°S, 173.7°W). These two solutions are separated by

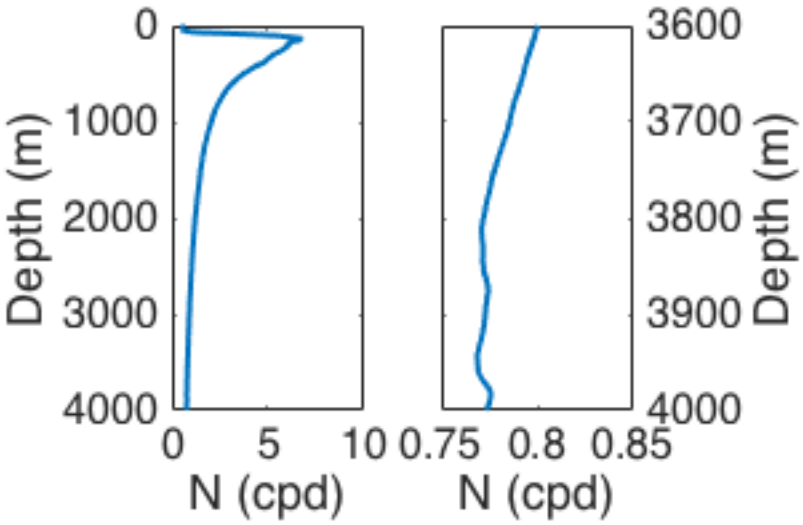

Figure 4.7: N vs depth for the whole water column (left) and zoomed in between 3600 and 4000 m (right).

49 km and are 593 km and 574 km from the observation site respectively (Fig. 4.11).

Ray tracing - down from the surface

When the ray tracing is started at the surface and propagated down to the observation site, starting at (15°36.6'S, 175°04.2'W) on June 3, 2013 the wave takes 226.5 days when $\tilde{f}$ is included. When $\tilde{f}$ is neglected the ray tracing starts at (15°46.2'S, 175°36.6'W) on May 22, 2013 and takes 235.3 days to reach the observation site. This is a difference of 8.8 days and 52 km between the two equations.

4.4 Generalizations/sensitivity

In the previous section, it was clear that the inclusion of $\tilde{f}$ was important in the calculation of the group speeds observed at 4000 m in the Samoan Passage. To determine the extent of the regions and the variables where $\tilde{f}$ is important, the relative error as a function of latitude ($\tilde{f}$ and f) was calculated and in addition to N for the dispersion relation and group speeds.

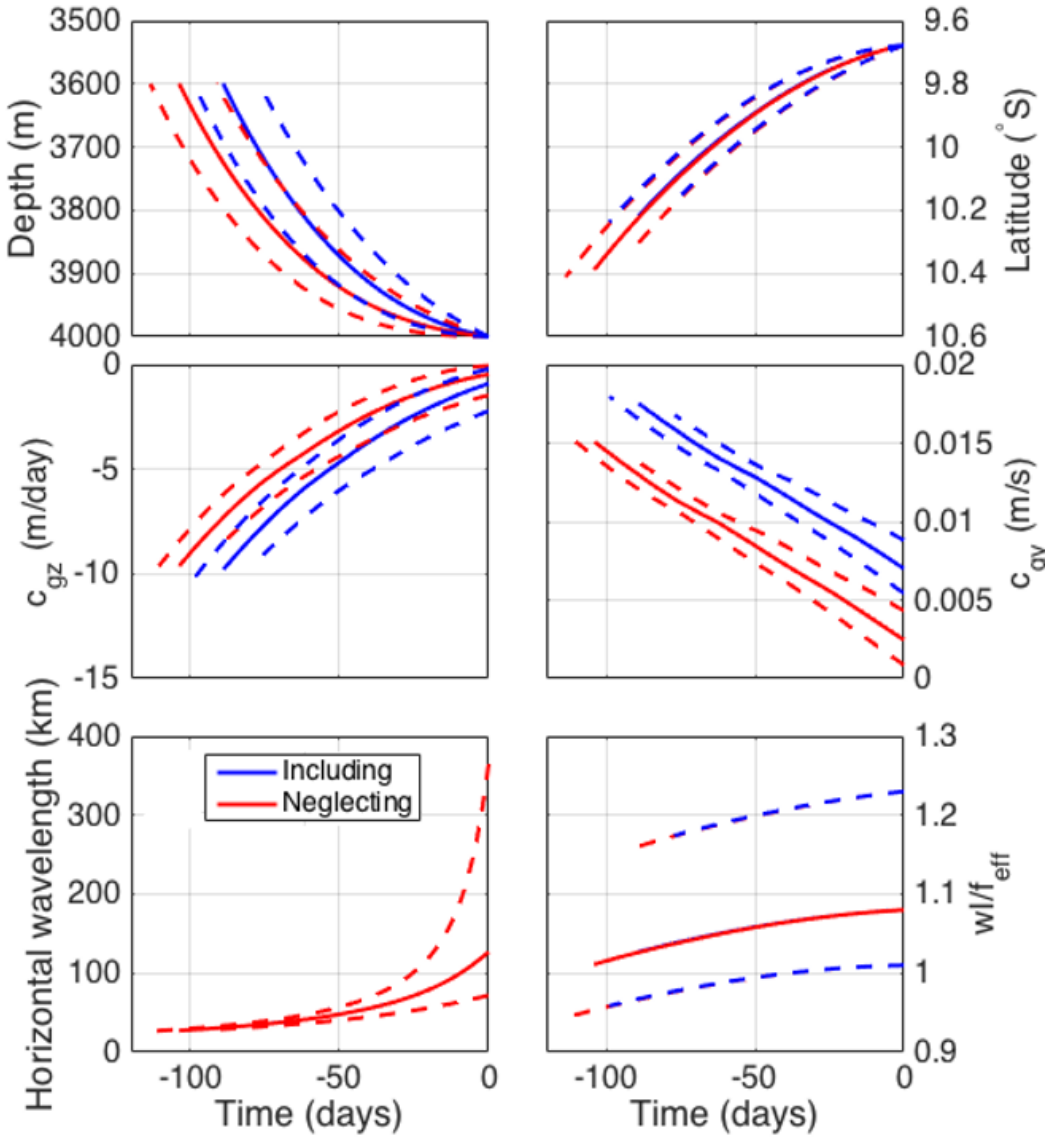

Figure 4.8: The ray tracing solutions for a NIW observed at (9°40.65′S, 169°50.57′W) on February 14, 2014 propagating up to 3600 m. Dashed lines show the upper and lower envelopes for $\omega_I \pm \omega_{Ierror}$. The solid line is the solution.

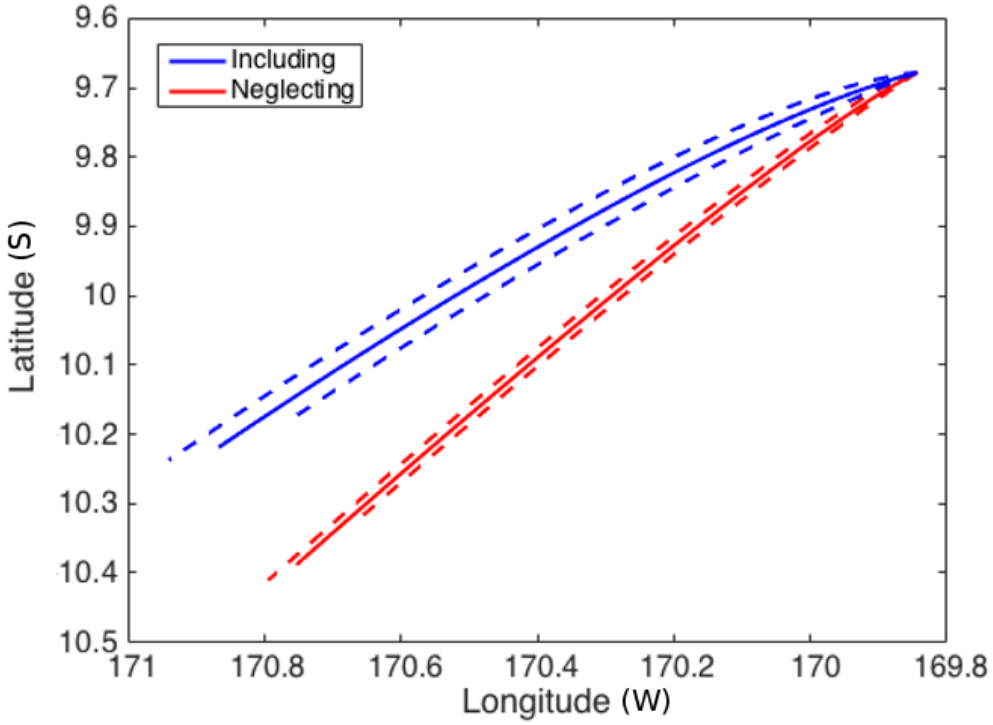

Figure 4.9: The ray tracing solution for a wave propagating up to 3600 m plotted in latitude vs. longitude.

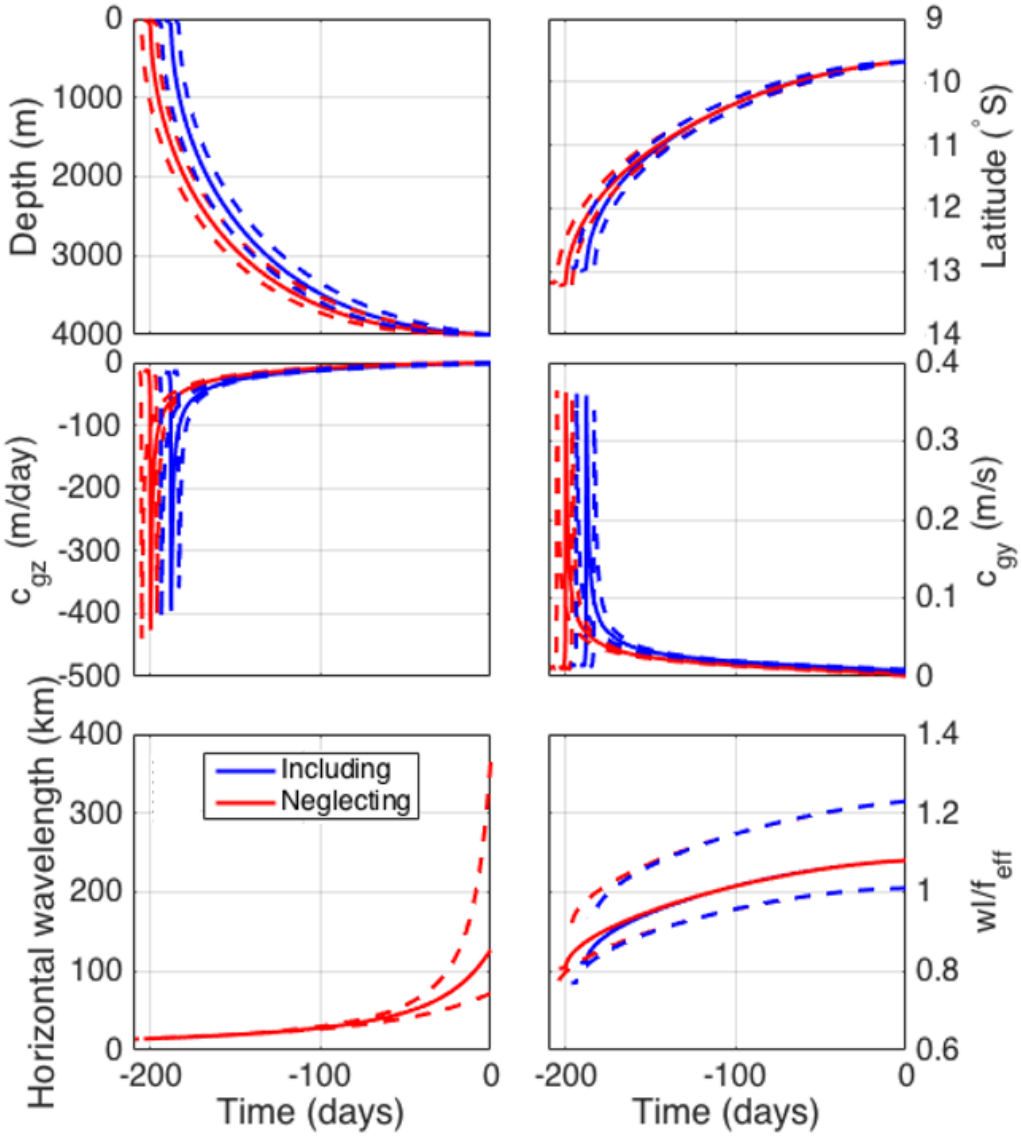

Figure 4.10: The ray tracing solutions for a NIW observed at (9°40.65'S, 169°50.57'W) on February 14, 2014 propagating up to the surface. Dashed lines show the upper and lower envelopes for $\omega_l \pm \omega_{lerror}$. The solid line is the expected path.

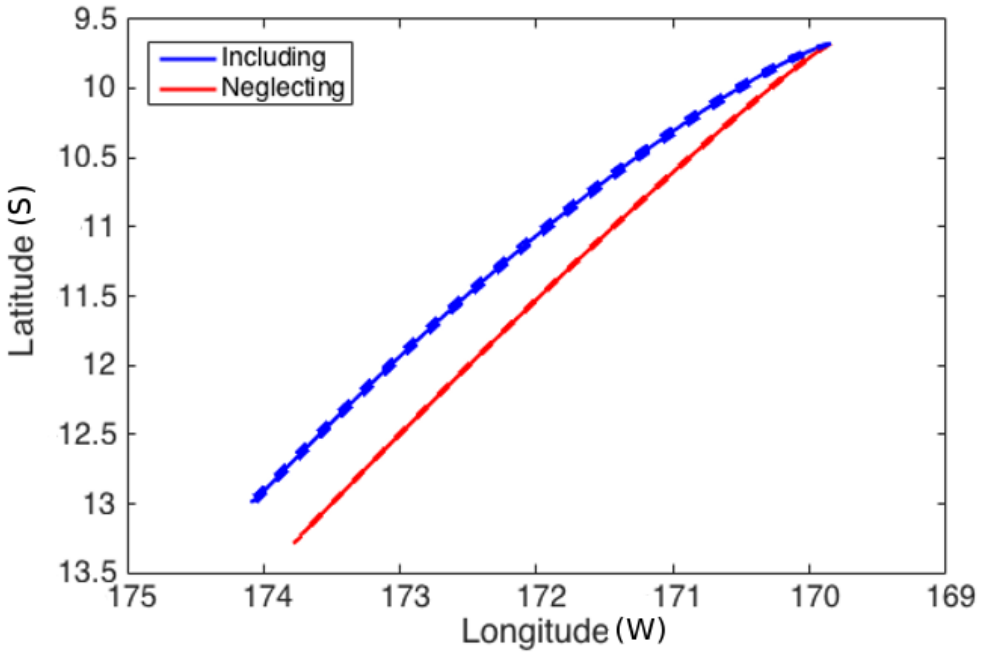

Figure 4.11: The ray tracing solution for a wave propagating up to the surface plotted in latitude vs. longitude.

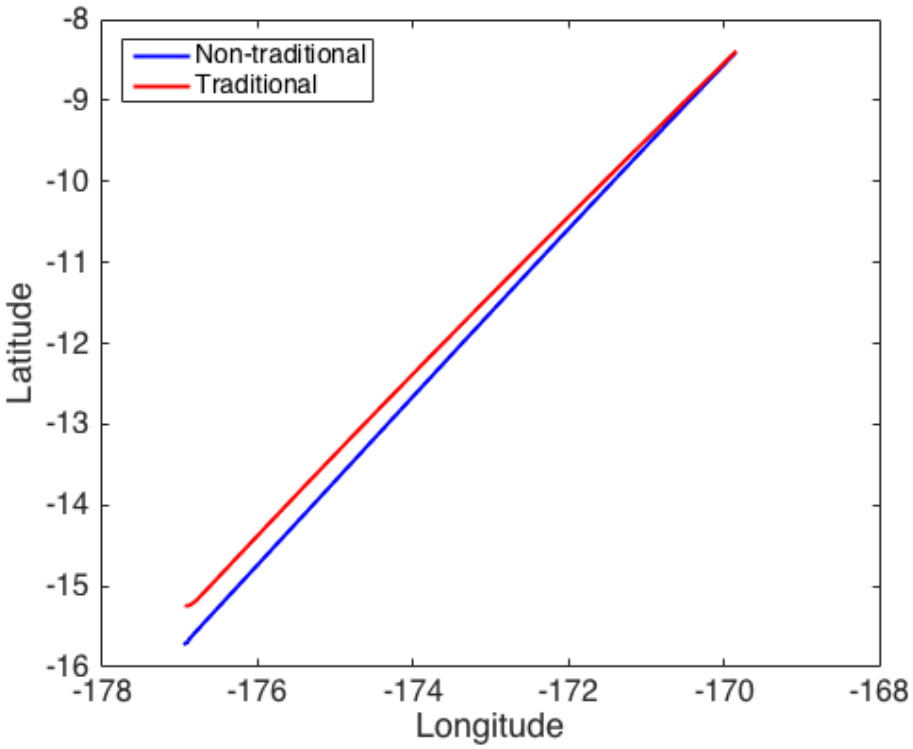

Figure 4.12: Ray tracing starting from the surface propagating down to the observation site. The wave originates at ((15°36.6′S, 175°04.2′W)) when $\tilde{f}$ is included, and when $\tilde{f}$ is neglected the wave originates at (15°46.2′S, 175°36.6′W). The origination sites are seperated by a distance of 52 km.

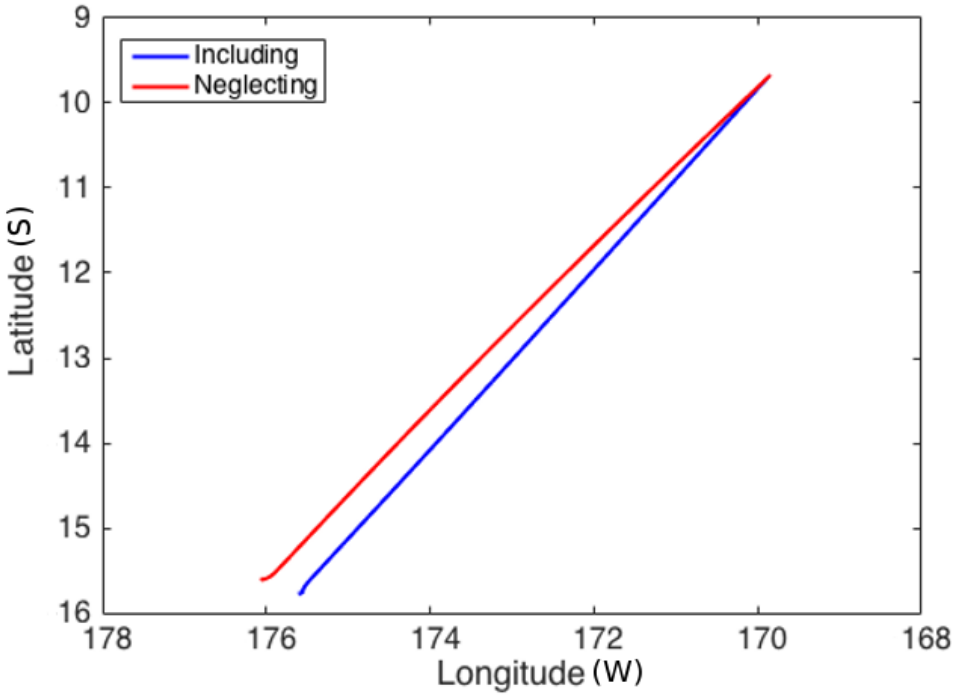

Figure 4.13: Ray tracing starting from the surface propagating down to the observation site. The wave originates at ((15°36.6′S, 175°04.2′W)) and takes 226.5 days when $\tilde{f}$ is included. When $\tilde{f}$ is neglected the wave takes 235.3 days to propagate to the observation site from (15°46.2′S, 175°36.6′W).

Following Guiles (2004), equations are converted to independent variables and then the percent difference is calculated. As a simplification, the inertial limit is applied. A full discussion of the derivation technique is outlined in Appendix 8.1. All figures shown illustrate the percent difference in the southern hemisphere as this is the location of the Samoan Passage. Calculations can be applied to the northern hemisphere.

4.4.1 Dispersion relation

When comparing the dispersion relation including $\tilde{f}$ (Eqn. 4.12) to that neglecting $\tilde{f}$ (Eqn. 4.11), it is apparent that the magnitude of the divergence between the two equations is dependent on the latitude and N (Eqn. 4.37). At low latitudes, $\tilde{f}$ is going to play a large role in the dispersion relation. This is simply due to the differences in magnitude of the respective Coriolis force components. In regions of low stratification, N^2 will not dominate the dispersion relation and the $\tilde{f}$ term will be more important.

The latitude is varied from the equator to 60°S and N from 0 to 0.05 Hz, in the calculation of Δ_{ω^2}, while holding all other variables constant to determine the relative importance of including $\tilde{f}$ (Fig. 4.14). As expected, at low latitudes and low stratification $\tilde{\omega}$ is larger, when the horizontal Coriolis term is included. The significant percent difference only occurs over a small range of latitudes, $2-5°$ S, and low N, $N < .0007$. Outside of this range there is no discernible difference between the two equations. As the Samoan Passage is outside of this range, the percent difference of ≈ 0.004 for Δ_{ω^2} in the Samoan Passage (latitude = 9°40.65'S and stratification ≈ 0.001 Hz) is expected (Fig. 4.2). There is a decrease in the percent difference between the two forms of the ω^2 equations at the equator: when the latitude is 0, where the terms with f in the difference equation drop out and the remaining terms are small, and the numerator is effectively multiplied by 0, reducing the value of the percent difference. At most latitudes and N, the inclusion of $\tilde{f}$ does not make a significant difference in the calculation of ω^2, although it may at low latitudes and extremely low N.

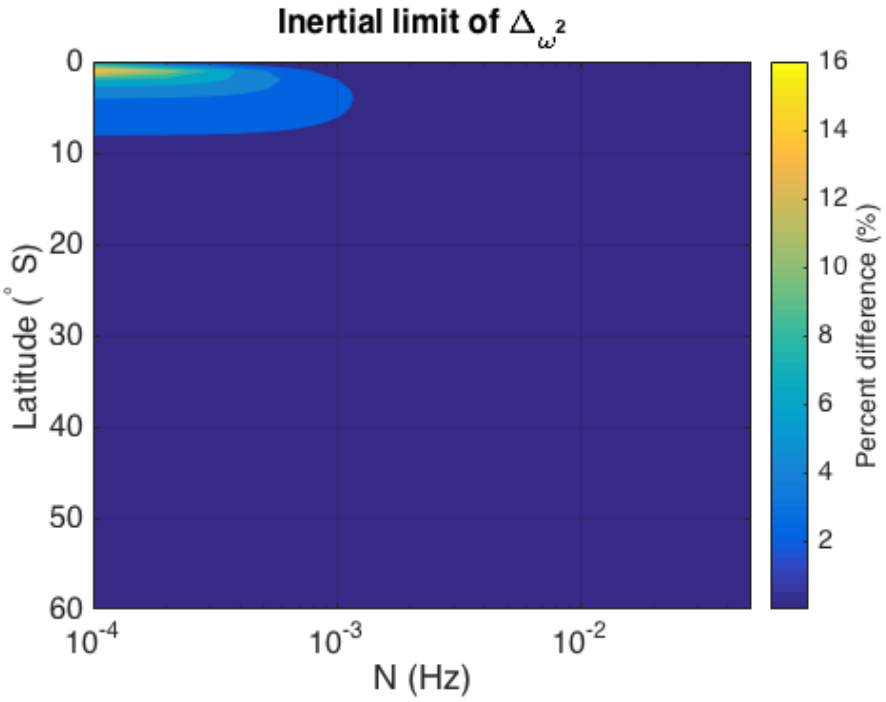

Figure 4.14: Calculation of Δ_{ω^2} near the inertial limit as θ approaches $\frac{\pi}{2}$ as a function of latitude and N.

4.4.2 Meridional group speed

The percent difference of the meridional group speed exceeded 20% in our case study of the Samoan Passage (Fig. 4.2). If we expand $\Delta_{c_{gy}}$ be a function of both latitude and N (Fig. 4.15), it is shown that the inclusion of $\tilde{f}$ is significant across a wide range of latitudes and N. This is particularly true for low N^2, $N < 0.003$, across our range of latitudes where the two calculations diverge by at least 5%. Similar to the Δ_{ω^2}, near the equator, the percent difference decreases due to the low inertial frequency going to 0. $\Delta_{c_{gy}}$ has the largest percent differences out of any of our calculations and the inclusion of $\tilde{f}$ needs to be considered in most situations with low N.

4.4.3 Vertical group speed

The vertical group speed has a smaller percent difference than horizontal group speed but still shows a considerable difference when $\tilde{f}$ is included. Similar to c_{gy}, the largest difference between the two terms is determined by the value of N^2, as was seen in our calculation for the Samoan Passage (Fig. 4.4). For values of $N < 0.003$, across most latitudes, the difference between including $\tilde{f}$ and neglecting $\tilde{f}$ is in excess of 10% (Fig. 4.16).

4.5 Summary

The percent difference was used to determine the necessity of including $\tilde{f}$ in both the Samoan Passage and more generally at the inertial limit. At low latitudes and low stratification, the dispersion relation was significantly different when $\tilde{f}$ was included. As a result, the inclusion of $\tilde{f}$ needs to be determined situationally. The effective frequency and horizontal wavenumber were not found to differ with the inclusion of $\tilde{f}$ in the Samoan Passage and generally. The equations for f_{eff} and k_H including $\tilde{f}$, are unnecessarily complicated and the authors recommend neglecting $\tilde{f}$ for f_{eff} and k_H, for the ease of calculation. The magnitude of group speed was found to be significantly different in the Samoan Passage when $\tilde{f}$ is included. More generally, the percent difference of the group speeds are found to

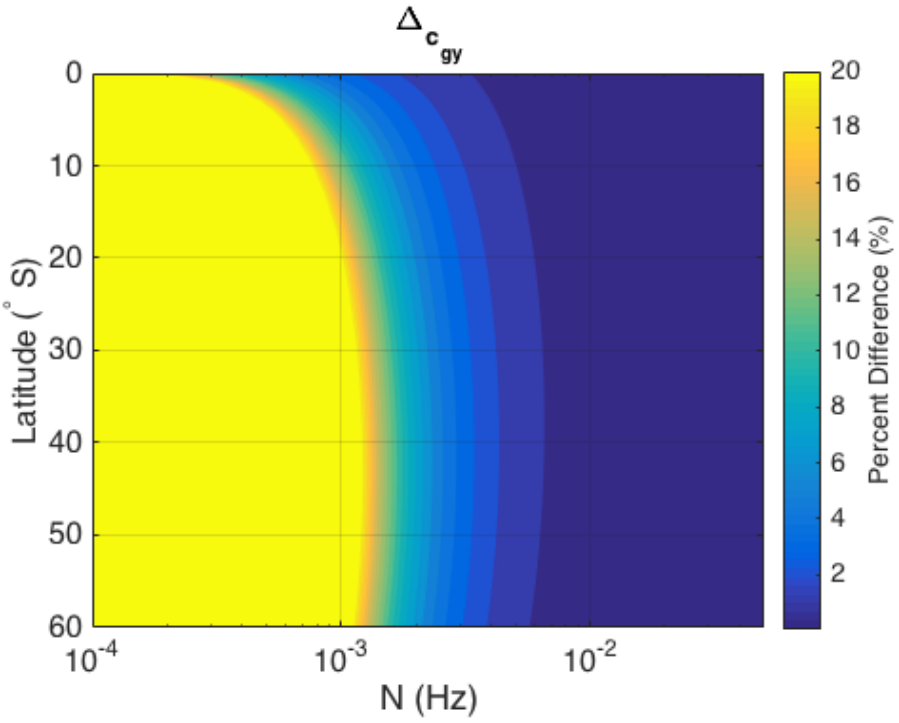

Figure 4.15: A plot of $\Delta = \frac{\tilde{c}_{gy} - c_{gy}}{c_{gy}}$ varying in latitude and N.

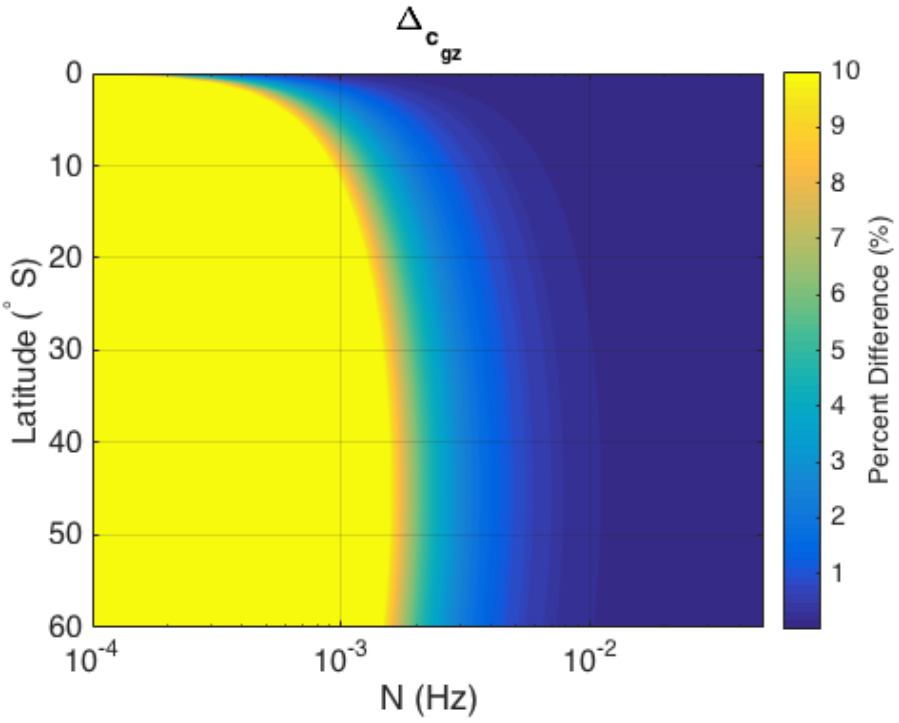

Figure 4.16: A plot of $\Delta = \frac{\tilde{c}_{gz} - c_{gz}}{c_{gz}}$ varying in latitude and N.

vary significantly at low N across a wide range of latitudes. The extent of the latitude range where the inclusion of $\tilde{f}$ is significant is extensive and in situations with low N $\tilde{f}$ should be included. This applies to calculations using the group speed such as ray tracing.

CHAPTER 5

Mixing

5.1 Introduction

Stommel (1958) was the first to propose a relationship between: abyssal circulation, deep water formation and water modification processes. This turbulent mixing diffuses heat downward and links the surface ocean to the deep ocean in the global thermohaline circulation. There is strong evidence for mixing in the abyss: cold dense water enters and warmer less dense water exits (Hogg et al., 1982). Some of such mixing is known to occur in constricted passages due to strong turbulence: Faroe Bank Channel (Fer et al., 2010), Vema Channel (Hogg et al., 1982) and in fracture zones: Romanche Fracture Zone (Ferron et al., 1998), Mid Atlantic Ridge (Polzin et al., 1997) and Southwest Indian Ridge (MacKinnon et al., 2008).

Near-inertial waves are commonly observed throughout the world's oceans, including at deep and abyssal depths (Webster, 1968, Fu, 1981). Estimates of the near-inertial energy input vary from 0.3 TW to 0.7 TW (Alford, 2003). NIW have been associated with increased mixing in the interior

ocean (Hebert & Moum, 1994, Alford & Gregg, 2001). In the internal ocean NIW have the potential to induce more mixing than internal tides (Alford et al., 2016). Microstructure measurements have shown enhanced diffusivity once per inertial period corresponding to strain induced instantaneous stratification. This corresponds to a Richardson number (Ri) of 0.6 (Alford & Gregg, 2001). Kunze & Sanford (1986) found amplification of NIWs during periods of NIW propagation opposing the mean flow. This is expected to induce increased mixing. During periods of propagation with the mean flow, the NIW is dispersed. There is seasonal variation in near-inertial mixing: Alford & Whitmont (2007) found an increase in mixing events corresponding to the winter.

Looking at the general thermohaline circulation in the Pacific, dense water flows up along the deep western boundary current and encounters Robbie Ridge and Manihiki Plateau (Reid & Lonsdale, 1974, Roemmich et al., 1996, Voet et al., 2016). This is where the majority of deep, cold, oxygen rich Antarctic Bottom Water (AABW) passes through the Samoan Passage (5.6 Sv (Voet et al., 2015)/6.0 Sv (Roemmich et al., 1996)), the first gap water below 4000 m encounters. Over the course of the passage, the AABW signal is mixed away (Roemmich et al., 1996). The Samoan Passage has been found to have 1000 to 10,000 times the typical abyssal mixing (Alford et al., 2013). This appears to be a result of various topographic features and accompanying hydraulic responses. The majority of the mixing in the Samoan Passage appears to be due to the trio of hydraulic jumps distributed across the Passage (Alford et al., 2013). Roemmich et al. (1996) concluded that strong mixing was required to eliminate the NADW high salinity signature and estimated a turbulent diapycnal diffusivity (K_ρ) of $5 \times 10^{-2} \frac{m^2}{s}$. Pratt (in prep.) speculates that a significant proportion of mixing in the North Pacific occurs in the Samoan Passage. As 15% of the world's ocean lies below 2000 m in the North Pacific, it is pertinent to understand the flow through the Samoan Passage and its associated mixing.

The primary focus of this chapter is to present deep mixing that occurs due to NIW. Section 5.2 presents the methods used including the depth integrated dissipation rate and energy flux. Section 5.3a investigates mixing at depths corresponding to NIW observations and 5.3b looks at turbulence below the interface and attempts to determine the cause of said turbulence and the near-inertial modulation of the signal. Correlation of various time series (Section 5.3c) and spectral analysis are

used to assess the causes of observed mixing between 4200 and 4600 m. The final two sections are the discussion and conclusion, 5.4 and 5.5 respectively, where the origin of the mixing and its relative importance in the Samoan Passage are discussed.

5.2 Methods

5.2.1 Dissipation

Epsilon (ϵ) values are calculated from density profiles using Thorpe scaling method specifically using the intermediate profile. Where ϵ is calculated as

$$\epsilon = L_0^2 N^3 = c L_T^2 N^3, \tag{5.1}$$

where $c = (L_0/L_T)^2$, L_T = the Thorpe length scale, and the Ozmidov scale (L_0) is 0.8 of L_T. For more information on the calculation of the Thorpe scale method refer to the appendix of Voet et al. (2016).

As calculated in Cusack et al. (prep), the depth integrated dissipation rate (F) is calculated as

$$F = \rho_0 \int_{z_0}^{z_1} \epsilon(z) dz, \tag{5.2}$$

where $\rho_0 = 1000$ kg m^{-3} and z is depth.

5.2.2 Energy Flux

Energy flux (F_E) is a tool used to assess the loss of NI energy as the NIW propagates to depth. F_E is calculated following Alford & Gregg (2001) where

$$F_E = c g_z E \tag{5.3}$$

and

$$E = HKE + APE = \frac{< \tilde{u}^2 + \tilde{v}^2 + \bar{N}(z)^2 \tilde{\xi}^2 >_\phi}{2} \tag{5.4}$$

where $\tilde{}$ denotes a perturbation quantity, $<>_\phi$ is the time average over a wave phase, $\bar{N}(z)^2$ is the time-averaged buoyancy and ψ is the vertical displacement.

5.3 Results

5.3.1 Mixing between 4000 and 4200 m

In Chapter 3 NIW were observed between 4000 and 4200 m. Dissipation is observed at these same depths and does not correspond to any specific phase of the shear or velocity, Figure 5.1. Dissipation occurs throughout the duration of each mooring. The T11 mooring observed the highest amount of depth integrated dissipation, between 4000 and 4200 m, of 2×10^{-2} W kg^{-1}. This depth integrated dissipation is an order of magnitude larger than T9 (5×10^{-3} W kg^{-1}) and T10 (4×10^{-3} W kg^{-1}) the other downstream moorings and two orders of magnitude larger than the upstream mooring, T12 (3×10^{-4} W kg^{-1}).

When ϵ is plotted against u and v velocity, no clear pattern emerges individually or across all moorings showing there is not preferential dissipation during any of the observed velocity regimes. The same is observed for ϵ plotted against u_z and v_z. There is an even distribution of ϵ for all quadrants. The strongest dissipation events occur during periods of time with negative v_z, however there are a limited number of these events and cannot be concluded definitively.

Overall, fewer overturns were observed at T12 than at the other moorings. However, if T12 is looked at individually, there are more dissipation events during the first half of the mooring deployment compared to the second half. As described in Chapter 3, the wave either propagated past the mooring in the latter half of the week or the wave event decayed. During the latter half of the deployment, there was a decrease in overturn-inferred mixing. As decay has been observed to correspond to increased turbulence (Hebert & Moum, 1994) it is suspected the wave propagates past

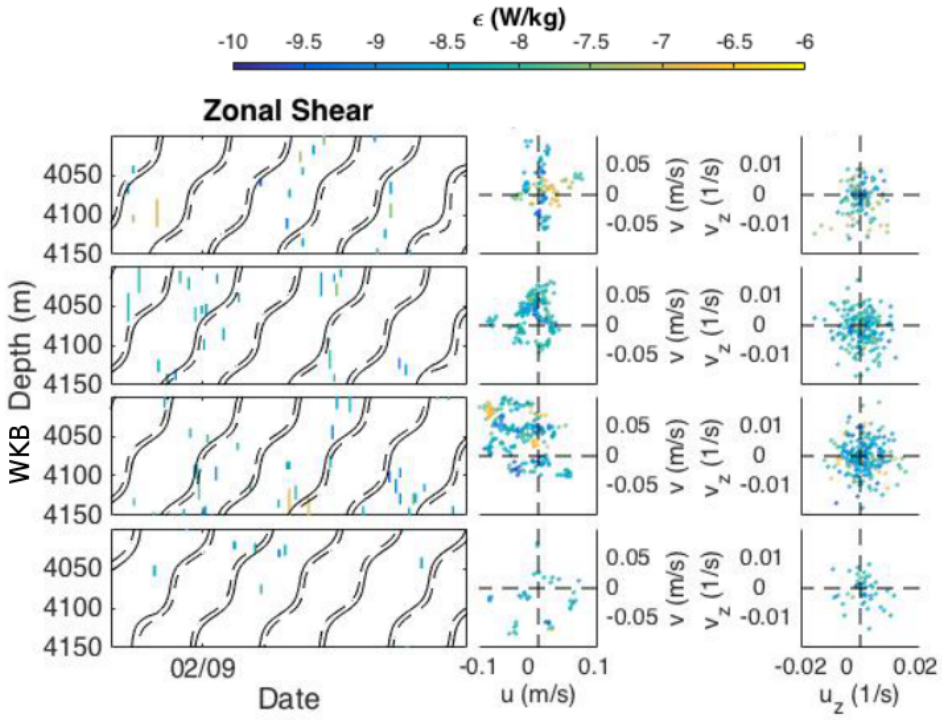

Figure 5.1: Depth-time plot of the $\log_{10}$ofϵ with the zonal shear contoured over the top in black. Zero values of the zonal shear plane wave solution are in solid black and black dashed contour indicates negative amplitude. The same ϵ values, between 4000 and 4200 m, are plotted against u and v velocities and zonal and meridional shear.

the mooring.

The magnitude and frequency of ϵ observed at these depths are much smaller and more infrequent than those observed below 4,200 m.

5.3.2 Mixing below the interface

Below the interface at 4200 m the moorings observed increased depth integrated dissipation rates (Fig. 5.2), particularly the moorings downstream of the sill (time-averaged, depth-averaged dissipation rates): T9 – 3×10^{-1} W kg^{-1}, T10 – 4×10^{-1} W kg^{-1}, and T11 – 3×10^{-1} W kg^{-1}. The upstream mooring, T12, had a depth integrated dissipation rate two orders of magnitude smaller than the

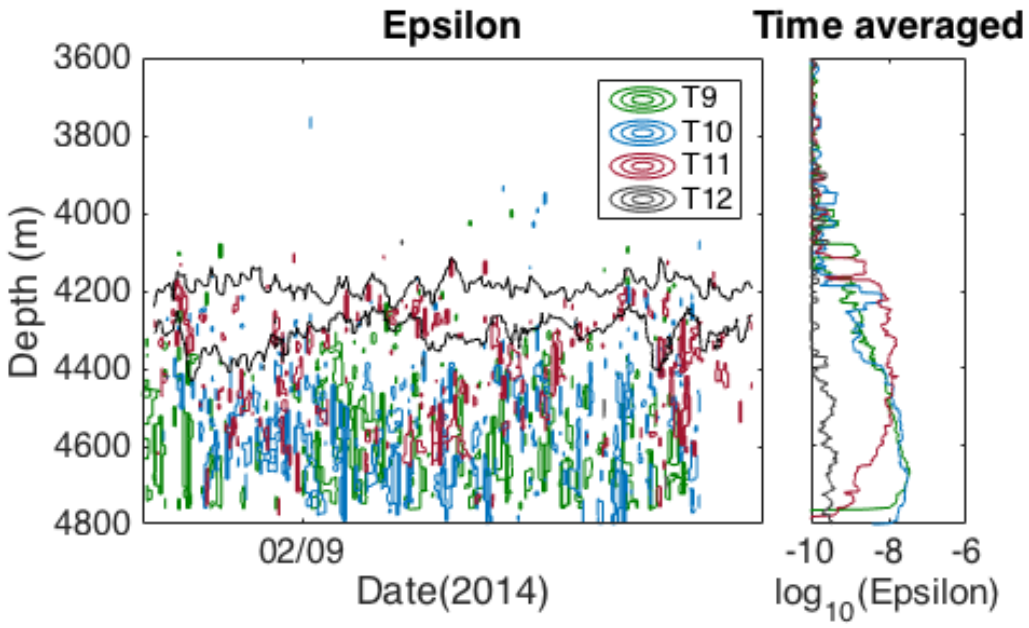

Figure 5.2: To the left, ϵ values from all moorings are plotted on top of each other. The 27.81 and 27.82 density levels are contoured in black. The time average ϵ values are plotted against depth to the right.

upstream moorings, T12 - 3×10^{-3} W kg^{-1}, only one order of magnitude larger than that observed between 4000 and 4200 m. The depth-time plot of epsilon shows a banding pattern that is not observed in the other moorings (Fig. 5.2). In addition, the time averaged dissipation signal at T11 is distinct from the signals observed at the other moorings (Fig. 5.2): bottom intensification is observed in the time averaged dissipation at T9 and T10 while the time averaged dissipation at T11 is higher in the water column with a near-bottom decay in intensity.

This banding pattern in ϵ is unique to T11 and is observed in both depth-time and mean isopycnal depth-time plots (Fig. 5.3 and Fig. 5.4). When plotted in both depth and mean isopcynal depth, below 4200m, the overturns appear to occur at a near-inertial frequency, below 4200 m. This is of particular interest as the other downstream moorings, that do not show this same banding T9 and T10, are only 2 and 1 km away respectively. No inertial signal in ϵ is observed at T9 and T10 even after bandpassing ϵ around f or complex demodulation of ϵ around f. This suggests that the inertial signal

at T11 is an isolated event and that an inertial signal at T9 and T10 is not obscured by ϵ from other sources: M2 (Cusack et al., prep) and hydraulic jump (Alford et al., 2016).

This banding signal is separate from the depths where we see the near-inertial signal in the shear (4000-4200 m). The inertial signal in ϵ occurs below the deep thermocline, at depths of accelerated flow (Fig. 3.4). The peak in dissipation coincides with a minimum in Richardson number indicating that the turbulence is produced by shear instability.

Similarly to Fig. 5.1, Fig. 5.5 plots the observed ϵ values in u and v velocities and u_z and v_z shears. Similar to the ϵ values discussed above, there is an even distribution of ϵ across all shear values. An increase in magnitude is not observed to correspond to negative values of v_z. However, the majority of dissipation events occur when there is positive values of v. This is to be expected as below the shear interface topographic acceleration has increased the northward magnitude of v. When plotted against the velocity perturbation from the mean, ϵ is symmetric about the origin for all of the moorings except for T11. Stronger and an increased number of dissipation events occur during periods when the perturbation v-velocity is negative.

Mean dissipation as a function of inertial phase is plotted for T11 in Fig. 5.6. Inertial phase is estimated as $\omega t + mz$ where ω represents the observed near-inertial frequency and m represents the vertical wavenumber. The near-inertial frequency, 0.35 cpd, and vertical wavenumber, 0.005 m^{-1} were calculated using a plane wave model in Chapter 3.2.4. At T11 the mean dissipation rate varies in an approximately sinusoidal manner over the inertial period where times of lower and higher mean dissipation differ by up to a factor of 2.

5.3.3 Correlation

The depth integrated dissipation rate time series will be used as a means of determining the variables that are correlated to the inertial mixing observed at T11 below 4200 m, Fig. 5.7. The variables compared include: depth integrated dissipation, transport, layer thickness, strain, N^2, shear, and velocity.

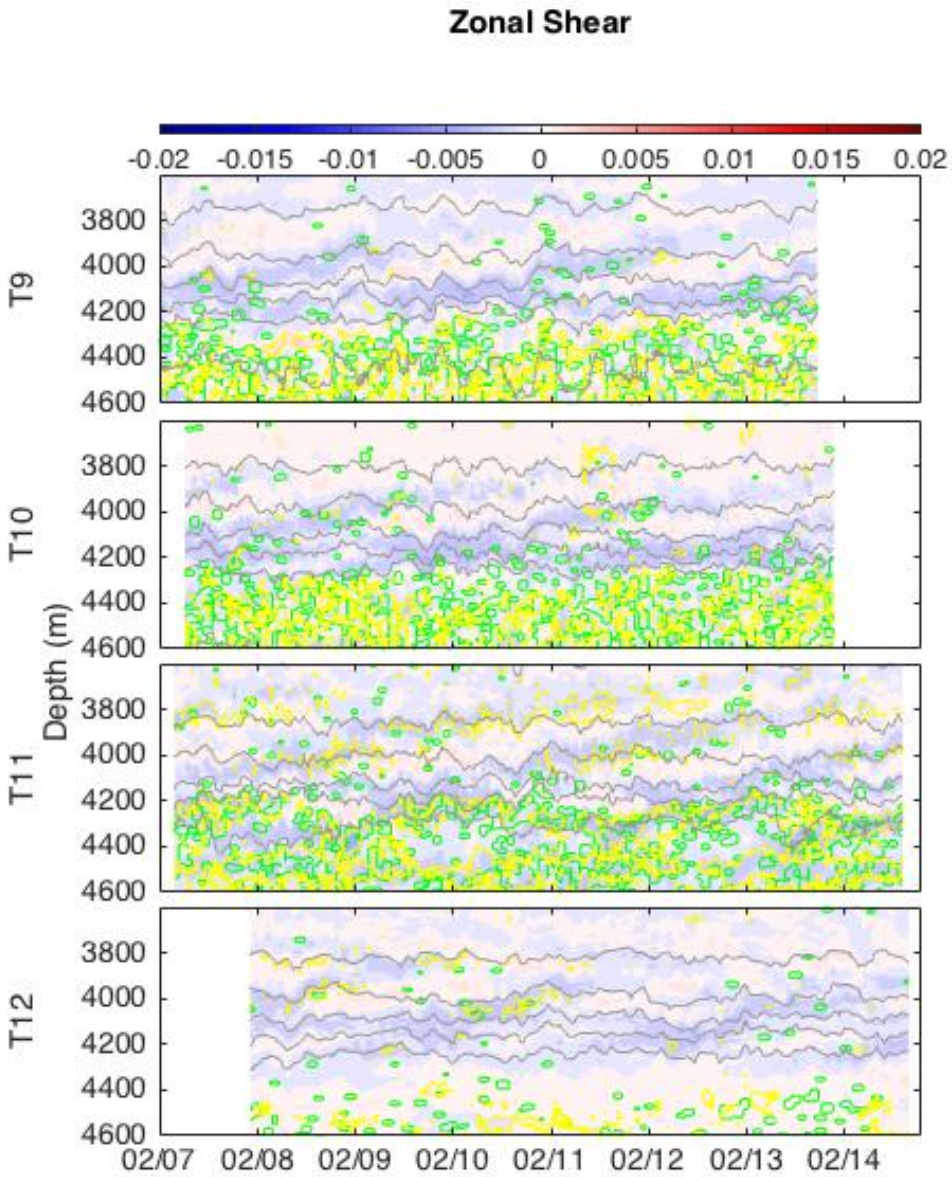

Figure 5.3: Background color is the zonal shear, calculated from the MP velocity profiles, plotted against depth. green contours the dissipation rate from overturns (contour value 5×10^{-9}W kg^{-1}). The Richardson number is contoured in yellow (contour value 0.25). Grey contours the isopycnals.

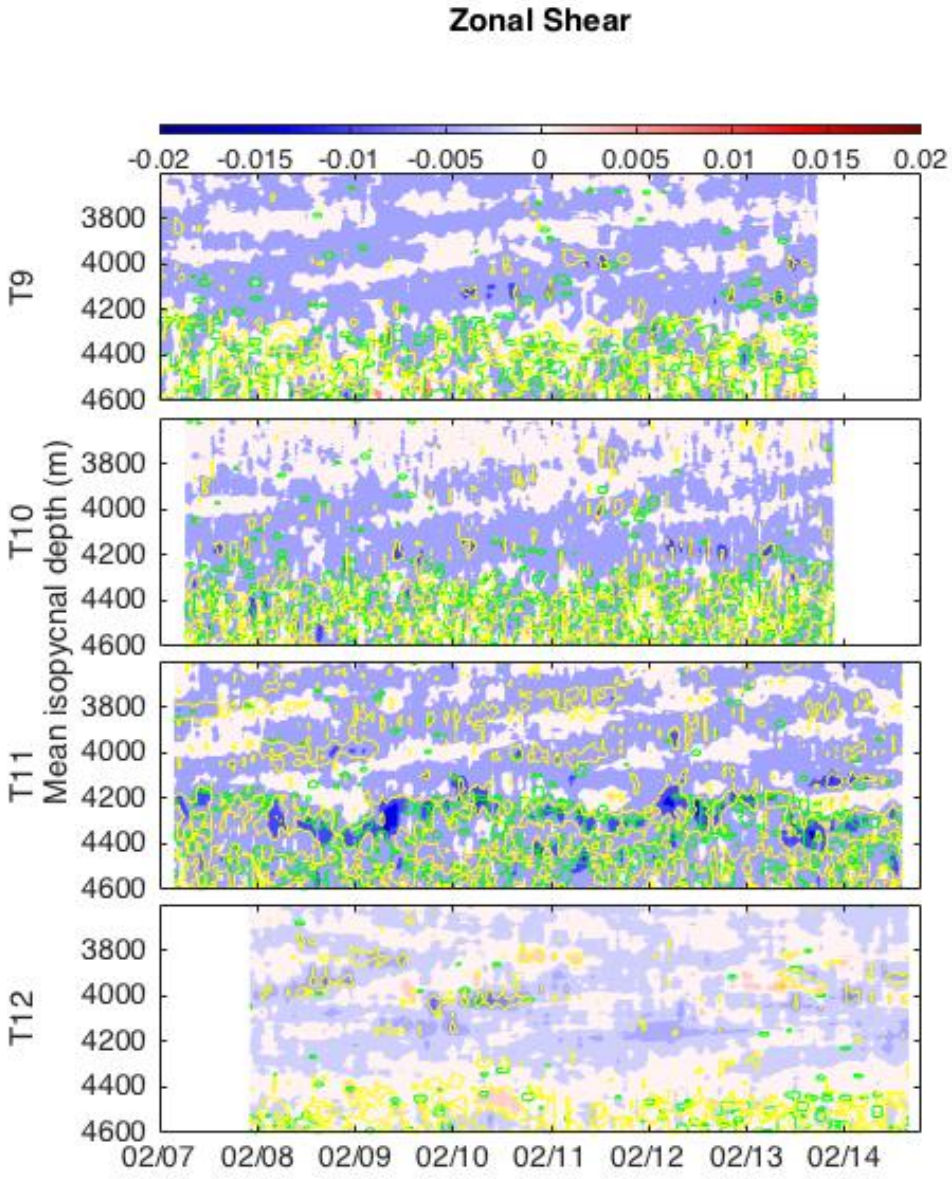

Figure 5.4: Background color is the zonal shear, calculated from the MP velocity profiles, plotted against the mean isopycnal depths. Green contours the dissipation rate from overturns (contour value 5×10^{-9}W kg^{-1}). The Richardson number is contoured in yellow (contour value 0.25).

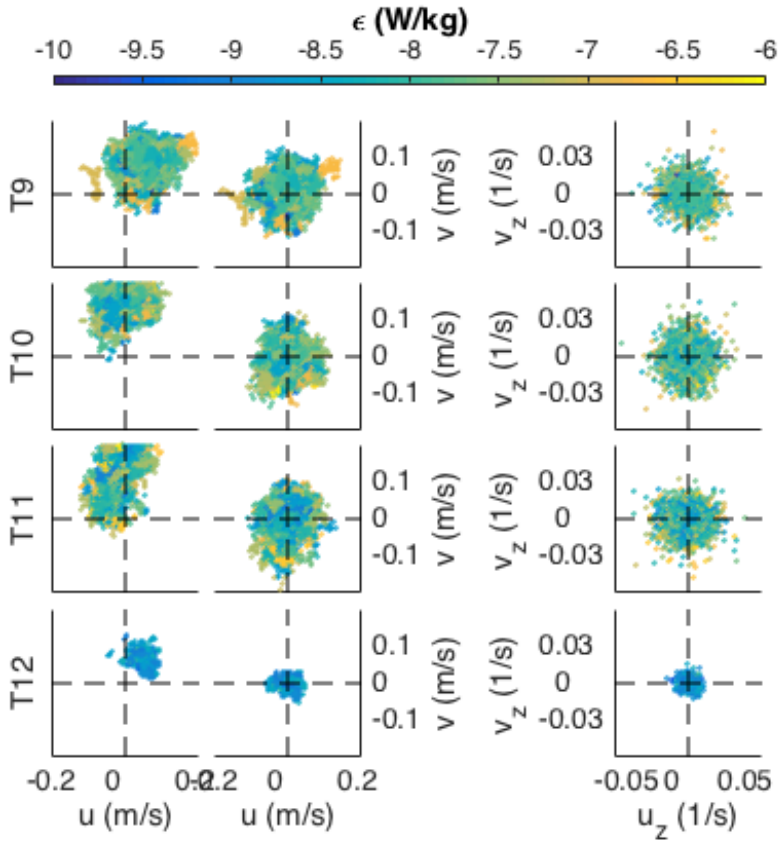

Figure 5.5: Similar to Fig. 5.1, $\log_{10}\epsilon$ between 4200 and 4600 m is plotted against velocity, perturbation velocity, and shear (from left to right) between 4200 and 4600 m.

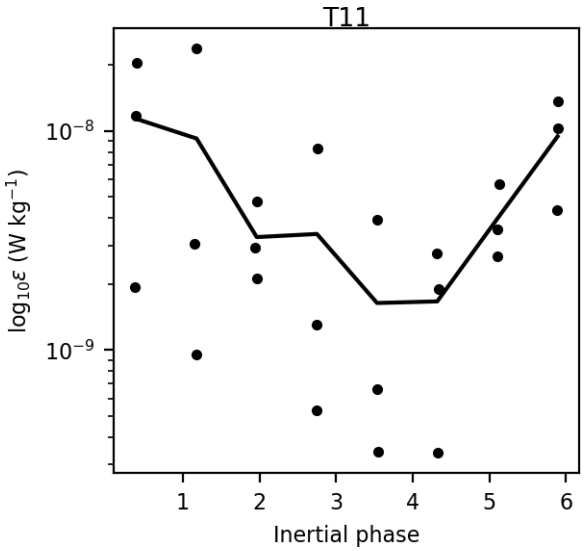

Figure 5.6: From Cusack et al. (prep) epsilon is plotted against the inertial phase for the depth averaged dissipation between 4200 and 4600 m.

For these sets of time series, correlation values (r) above/below ±0.25 are considered correlated. As the time series have not been filtered, there are other signals at various depths that obfuscate the signal and decrease the magnitude of r.

Depth integrated dissipation rate

The depth integrated dissipation rate is calculated for 4000-4200 m and 4200-4600 m, Fig. 5.7. The time series for 4000-4200 m does not show a signal, as expected (Sec. 5.3.1). However, the time series for 4200-4600 m does show modulation of the depth integrated dissipation at an inertial frequency. There is no correlation between the two time series ($r = -0.01$), depth integrated dissipation rate between 4000 and 4200 m and the depth integrated dissipation rate between 4200 and 4600 m. This is not surprising as the overturns between 4000 and 4200 m are infrequent.

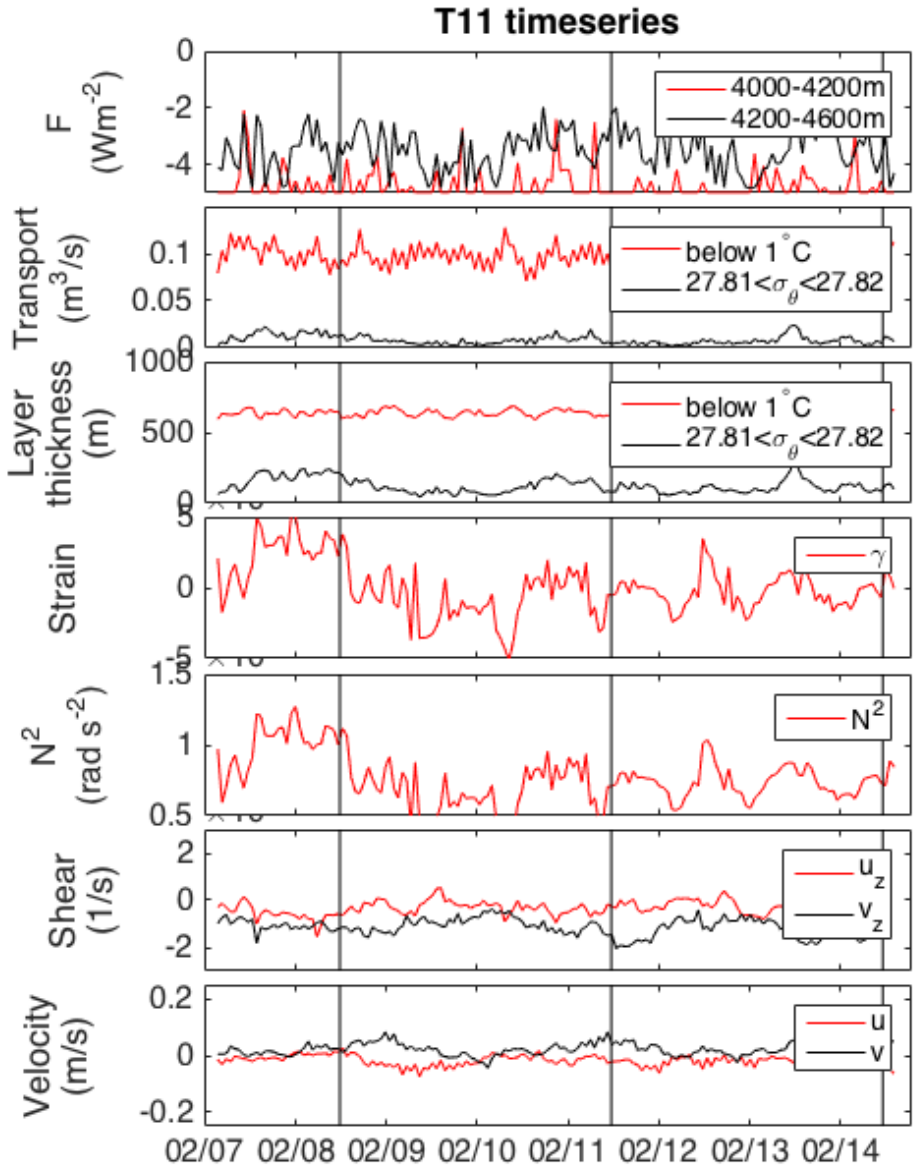

Figure 5.7: The depth averaged time series, between 4000 and 4200 m, 4200 and 4600 m, below 1°circC or $27.81 < \sigma_\theta < 27.82$, of depth integrated dissipation, transport, layer thickness, strain - between 4200 and 4600 m, N^2 - between 4200 and 4600 m, shear - between 4200 and 4600 m and velocity - between 4200 and 4600 m.

Transport

The transport below 1°C, chosen to match the definitions used in Rudnick (1997) and Voet et al. (2015), calculated over the short term moorings does not appear to have a near-inertial signal. When compared to the overturn signal between 4200 and 4600 m a negative correlation coefficient of $r = -0.12$ is found, showing a minimal correlation between the two time series.

The average value of epsilon between $27.81 \leq \sigma_\theta \leq 27.82$ (black) does show a near-inertial modulation of the signal at T11, but this is not observed at any of the other moorings, not shown. The transport between those two layers does have a higher positive correlation with the deep depth integrated dissipation rate, $r = 0.16$, but not showing a strong relationship. The transport does show a strong negative relationship with u_z, between 4200 and 4600 m, where $r = -0.51$ with no time lag. This is not the case with v_z where $r = -0.18$ with a time lag of approximately 2 minutes and with S where $r = 0.25$ with no time lag.

Voet et al. (2016) observed a near-inertial signal in the transport in the time series of the long-term moorings in the mouth of the channel with the peaks at f between 0.85 and 1°C. There is no obvious near-inertial signal in the transport below 1°C at T11, Fig. 5.7. The lack of inertial signal does not contradict Voet et al. (2016)'s findings as his observations were in a different location, time, and depth range.

Layer Thickness

There is a near-inertial signal, at T11, for the layer thickness between σ_θ of 27.81 and 27.82 and no near-inertial signal in the layer thickness of waters below 1°C, Fig. 5.7. The layer thickness, $27.81 < \sigma_\theta < 27.82$, has a correlation of $r = 0.33$ with the deep overturn signal. This density layer lies at the top of the 4200-4600 m depth range, in depths immediately above where the majority of overturns occur. Also, $r = 0.30$ and $r = -0.38$ for the density layer thickness with u_z and v_z, between 4200 and 4600 m, respectively. It is interesting to note that the layer thickness of waters below 1°C and v_z has a negative correlation coefficient of $r = -0.48$. This is one of the highest correlations

found in the various time series and shows that the layer thickness of waters below 1°C is either driving or driven by the meridional shear in and below those depths.

Strain

No inertial signal is apparent in the strain time series, Fig. 5.7. There is no correlation between the strain and the overturns between 4200 and 4600 m.

N^2

Similar to the strain, N^2 does not show an inertial periodicity and is not correlated to the deep overturn signal between 4200 and 4600 m.

Shear

The time series of shear shows near-inertial modulation of v_z and no apparent signal in u_z. The S and v_z time series are highly correlated to the depth integrated dissipation rate between 4200 and 4600 m, $r = 0.36$ and $r = -0.44$ with a 0 time lag respectively. The deep v_z also has a high correlation to the v_z above the interface, between 4000 and 4200 m, $r = 0.50$. The meridional shear above the interface has a high negative correlation to the overturns between 4200 and 4600 m, $r = -0.36$.

The anticyclonic and cyclonic shear spectra show a commonality of a peak in the anticyclonic shear spectra between 4000 and 4200 m in all moorings. A distinct secondary anticyclonic shear spectra peak is observed at 4300 m only in the T11 mooring. There is a signal in the cyclonic shear spectra below 4200 m but if we look at the difference between anticyclonic and cyclonic it becomes clear that the magnitude of the cyclonic shear spectra peak does not dominate the signal like anticyclonic shear spectra peak. Between 4200 and 4400 m, the depths of the overturn signal, there are approximately equal peaks in both anticyclonic and cyclonic shear spectra at T11. Below 4200 m flow is generally rectilinear, as shown by the low rotary coefficient.

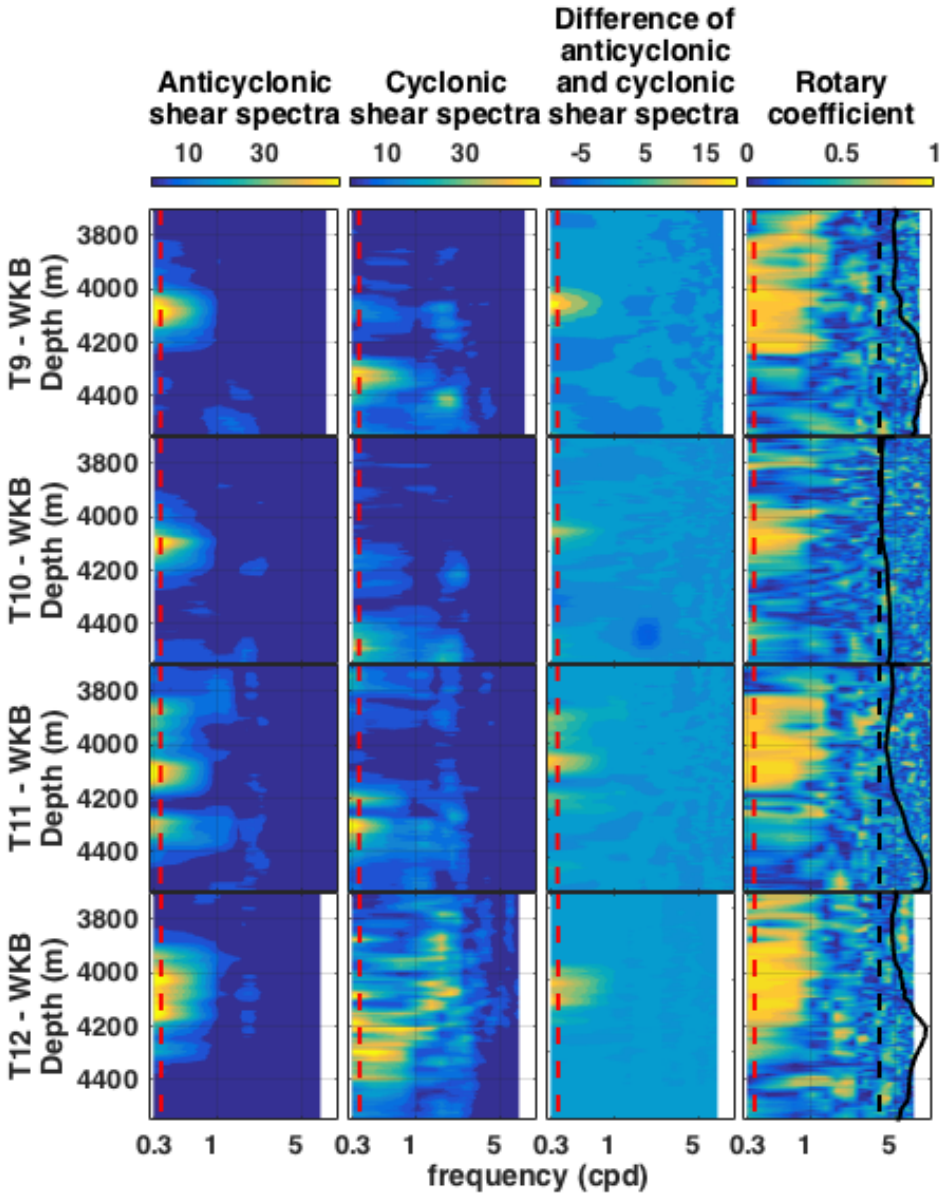

Figure 5.8: Depth plot of the shear spectra for the four short-term moorings. The red dashed line shows the local Coriolis frequency. The black line is the magnitude of the velocity with the black dashed line denoting 0 m/s. A zero rotary coefficient denotes rectilinear flow while 1 is circular flow.

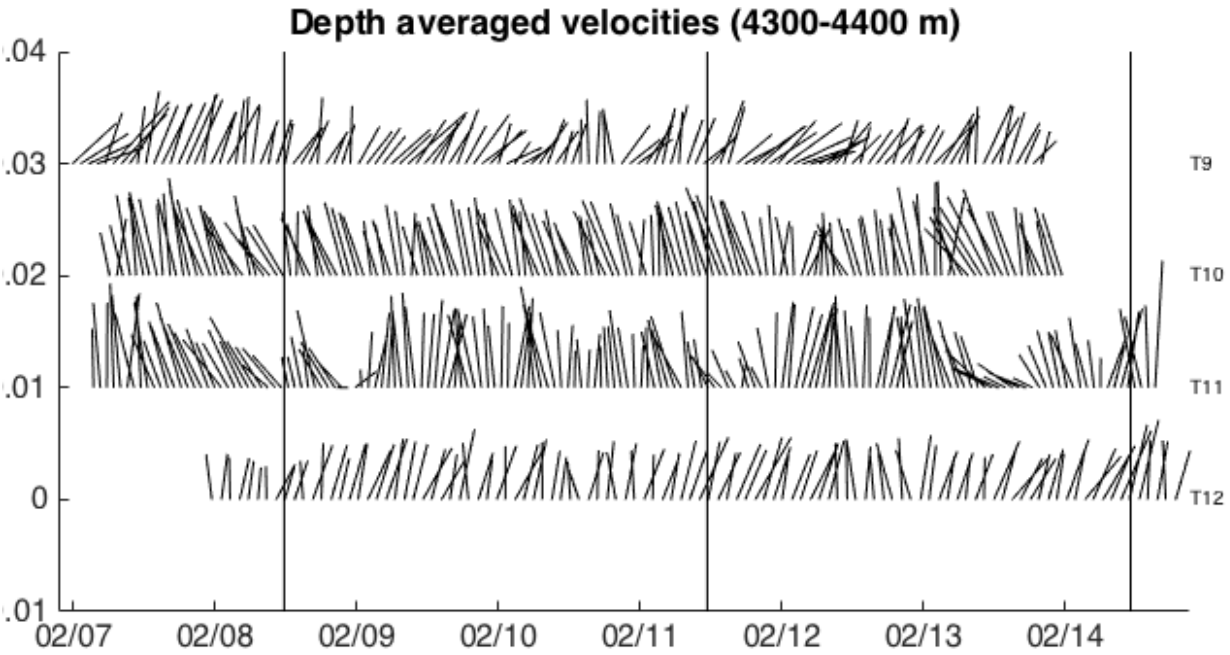

Figure 5.9: The average velocity between 4300 and 4400 m plotted for each of the four moorings. Vertical black lines are separated by one local inertial period.

Velocity

There is no apparent inertial signal in the depth averaged, between 4200 and 4600 m, velocity time series, Fig. 5.7. However the stick plot of the average velocity between 4300 and 4400 m, Fig. 5.9, shows decreased magnitude and modulation of the flow direction at an inertial frequency. These minimum vector lengths correspond to the maximum epsilon values. The flow does not reverse, as the direction of the near-inertial wave opposes the mean flow it just decreases the magnitude. The v-velocity time series has a negative correlation of $r = -0.33$ with the overturns between 4200 and 4600 m.

Above the interface, where the flow is dominated by the inertial signal, the average velocity between 4000 and 4150 m shows a very distinct signal in each of the moorings at a near-inertial frequency, Fig. 5.10. This is in the depth range where we see the near-inertial signal in the shear, as discussed in Chapter 3.

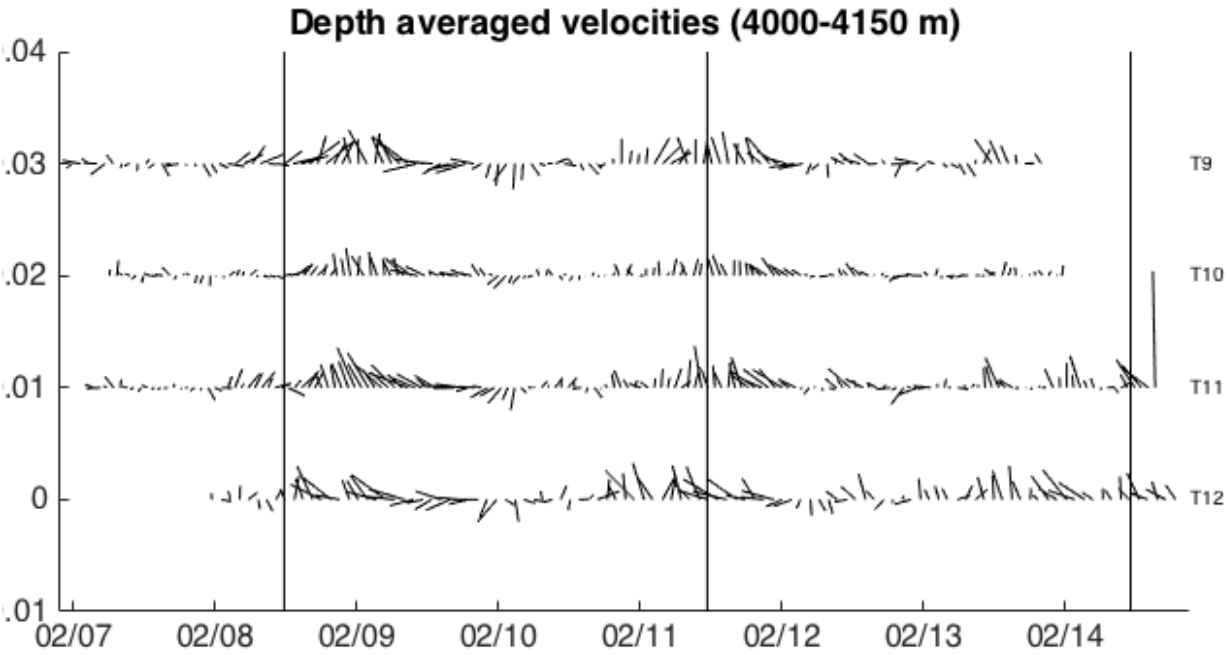

Figure 5.10: The average velocity between 4000 and 4150 m plotted for each of the four moorings. Vertical black lines are separated by one local inertial period.

The spectra of the velocities show a peak near the inertial frequency between 4000 and 4200 m for all moorings and a secondary, strong peak between 4200 and 4400 only at T11, Fig. 5.11. T9, T10, and T11 all have an insignificant peak in cyclonic velocity spectra near f below 4200 m. The differences between the anticyclonic and cyclonic velocity spectra highlight the differences in the magnitudes between the anticyclonic and cyclonic peaks. The secondary peak, centered on 4300 m, at T11 is more distinct than the secondary peak observed in the difference of shear spectra. The v-velocity, between 4200 and 4400 m, varies as a step function at a near-inertial frequency, Fig. 5.12. This step function banding extends over 200 m and as a result of the near-constant velocity in the vertical has a minimal shear signal at these depths.

5.4 Discussion

Although not a significant source of mixing it could be argued that the mixing between 4000 and 4200 m is increased by the presence of NIW. For a more conclusive result, moorings would need to be deployed during periods when a NIW is not observed. Between 4000 and 4200 m the dominant signal is inertial and when the near-inertial wave signal started to end, at the end of the time series at the T12 mooring, the depth integrated dissipation decreased. The depth integrated dissipation rates, between 4000 and 4200 m, vary similarly to the magnitude of the v-velocity. Not all of the NIW energy is dissipated between 4000 and 4200 m. The time-averaged flux shows a general increase in the energy flux with depth, Fig. 5.13, the increase is a result of topographic acceleration below 4200. As NI energy is the dominant signal between 4000 and 4200 m, the depth integrated dissipation rate between 4000 and 4200 m is a small fraction of the total depth integrated dissipation rate, and the time average total energy flux slightly increases from 4000 to 4200 m it indicates minimal energy is lost to dissipation at those depths.

The upward propagating wave could be the result of a few scenarios: partial internal reflection off of the N^2 peak, partial reflection off of the shear interface, reflection off of topography or locally formed and upward propagating. The source of the upward propagating wave is beyond the scope of

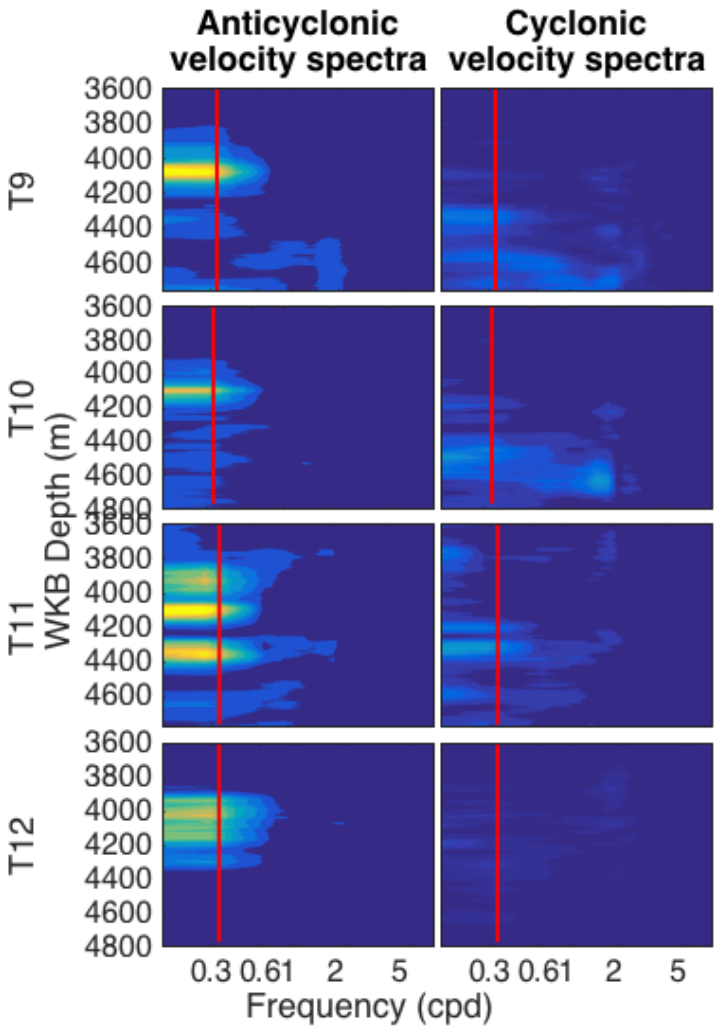

Figure 5.11: Rotary spectra of the velocity vs depth. The vertical red line is at the local Coriolis frequency.

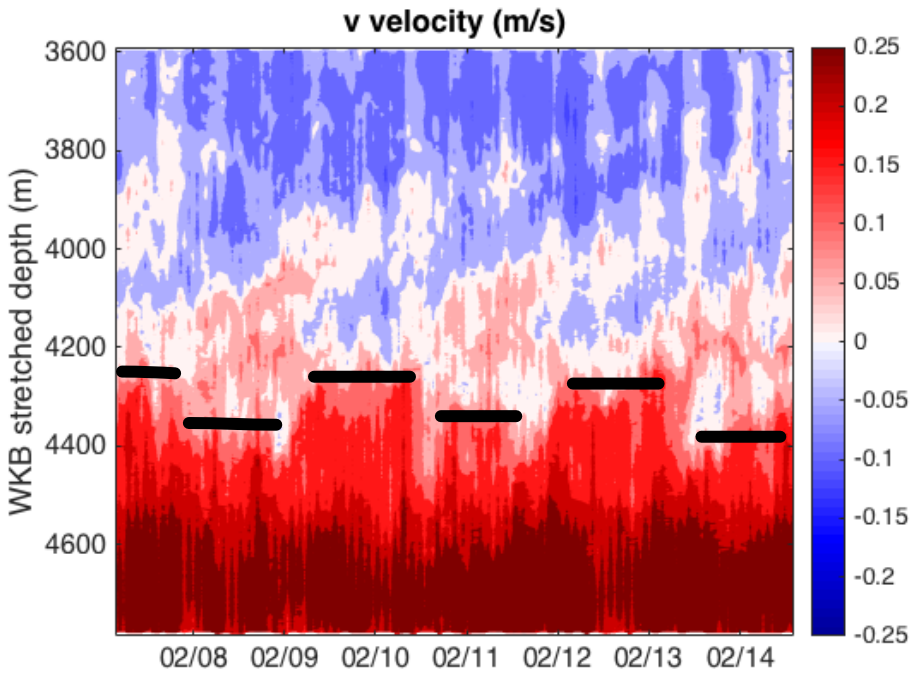

Figure 5.12: The WKB stretched depth vs time v-velocity at T11. The black bars were added manually to highlight the presence of a pseudo-step function around 4300 m.

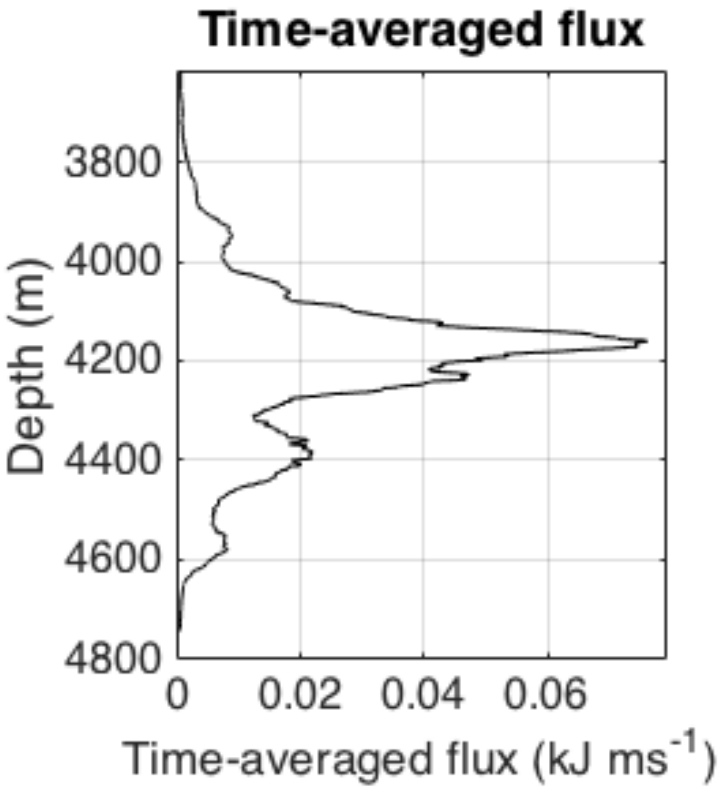

Figure 5.13: Time-averaged flux at T11 plotted against depth.

this paper. It is important to note, in all of these situations, NI energy propagates past the interface and shear layer into the depth ranges where the near-inertial signal was observed in the depth integrated dissipation rate.

Visually, a near-inertial signal is observed in the depth integrated flux, transport, layer thickness, v_z and velocity. There is a negative correlation ($r = -0.36$) between v_z between 4000 and 4200 m and the overturns between 4200 and 4600 m as well as a very strong correlation of 0.50 between the v_z above the interface and the v_z below the interface. These are the only significant relationship found between a variable above the interface and the overturns below the interface. The shear of the inertial wave signal discussed in Chapter 3 is modulating variables below the shear and leads to increased mixing at an inertial period. Below the interface there is a significant relationship between v-velocity, S, v_z or layer thickness and the deep overturns, with correlation coefficients of -0.33, 0.36, -0.44, and 0.33 respectively. In addition, layer thickness is found to vary with u_z and v_z with the respective correlation coefficients of 0.30 and -0.38. Strain is found to vary with shear: S, u_z and v_z with correlation coefficients of -0.30, -0.30 and -0.34 respectively. The ultimate path for the NIW shear, between 4000 and 4200 m, to elevate depth integrated dissipation rate is not clear. It is clear that the meridional shear dominates the process. Minimal Richardson numbers corresponding to turbulence corroborate this conclusion.

As we do not see other signals at T11: M2, K1, etc., the meridional shear above the interface must interact with the interface or accelerated flow and ultimately result in increased mixing between 4200 and 4600 m.

The Samoan Passage is comprised of two channels and 3 hydraulically controlled jumps. The strongest mixing (0.1W m^{-2}) occurs at the northern sill in the eastern channel. The observations described thus far in this chapter are at the southern sill in the western channel. Cusack et al. (prep) describes three moorings in the eastern channel: T4 located downstream of a sill(0.1 W m^2), P5 located on the sill (0.01 W m^{-2}) and T7 in the middle of the passage (0.002 W m^{-2}). While not as dissipative the northern sill, the southern sill can be similarly described by the dissipation observed at the moorings: T9 (0.004 W m$^-$2) located in a high dissipation environment downstream of the sill,

M5 (0.001 W m^{-2}) located on top of the sill and T12 (0.0002 W m^{-2}) located in a relatively quiescent region at the passage entrance. However the southern sill has an anomaly, T11 (0.003 W m^{-2}). This mooring is downstream of the sill with comparable depth integrated dissipation to the high dissipation environment at T9 yet it has a different pattern to dissipation. At T11, the near-inertial wave observed between 4000 and 4200 m propagates past the interface and induces increased mixing between 4200 and 4600 m. This near-inertial dissipation signal, below the interface, is only observed at T11.

A brief explanation of the flow pattern will illuminate the differences between T11 and the adjacent moorings. The southern sill has a secondary bump on the western edge, this topographic feature induces northward acceleration of the flow past T11. The moorings T9 and T10 do experience some topographic acceleration although not as extreme. However, T9 and T10 are in the path of the hydraulic jump over the southern sill and accordingly experience increased dissipation as a result.

5.5 Conclusion

Although near-inertial energy is observed at all moorings around the P2 sill, the time average depth of near-inertial wave integrated (4000-4200 m) dissipation rate for the T11 mooring downstream of the M5/P2 sill is 0.0001 W m^{-2}, a small fraction of the time average full depth integrated dissipation rate at T11 (0.004 W m^{-2}). This value is comparable to values observed at other moorings in the region. The near-inertial wave is the dominant signal above the shear layer however, the turbulent bottom boundary layer dominates the depth integrated dissipation as commonly observed with other moorings in the region (Cusack et al., prep).

Increased dissipation due to NIW is found between 4200 and 4600 m. The signal is isolated to the T11 mooring and is not observed at adjacent moorings, T9 and T10, only 2 and 1 km away respectively. The NIW observed between 4000 and 4200 m, Chapter 3, interacts with the interface and results in layer thickness modulation and meridional shear below 4200 m. Both the shallower and deeper depth averaged meridional shear are found to be correlated to the observed near-inertial

modulation of the depth integrated dissipation rate. The maximum dissipation occurs during periods where the magnitude of the v-velocity is minimized, not reversed, when the NIW opposes the direction of background flow. Low Richardson numbers correspond to mixing events in agreement that shear is driving the observed mixing. While not the highest in the Samoan Passage, the mixing between 4200 and 4600 m is found to be comparable to the increased mixing, due to the hydraulic jump at the southern sill, at T9 and T10.

Kunze & Sanford (1986) found that NIW induced mixing was increased when the NIW propagates against the background current, in agreement with our observations. They also concluded that when the NIW propagates with the current, the NIW is dispersed. It is impossible to say if that happens in these observations.

It has been found that NIW play an important role in the mixing in the western channel and as such would need to be considered for any comprehensive mixing budget for the Samoan Passage. In addition, NIW should be considered as an additional means of mixing in deep and abyssal topographic constrictions.

CHAPTER 6

Summary and conclusions

6.1 Summary

Observations show the presence of NIWs in the Samoan Passage. These waves can be described using the interference pattern of a downward propagating and an upward propagating, plane wave solution. The downward propagating wave has a vertical wavenumber of 0.005 m^{-1}, intrinsic frequency of 0.36 day^{-1}, and northward propagation. The upward propagating, 1/4 the amplitude, wave has a vertical wavenumber of 0.007 m^{-1}, and intrinsic frequency of 0.33 day^{-1}. This plane wave solution is found to be coherent across all four of the concurrent time series. Wavelet analysis shows seven NIW events over the course of the 17-month mooring. These events have vertical wavelengths ranging from 0.005 to 0.01 m^{-1}. During periods with NIW activity, the u velocity decreased (-0.0028 m/s), the v velocity increased (0.0023 m/s), and the 27.876 kg/m^3 isopycnal was depressed (14 m on average).

From the plane wave solution, it is possible to derive the effective frequency, horizontal wavenumber, and group speeds. When a range of latitudes and N^2 values are applied and the near-inertial limit is imposed, it becomes clear that the inclusion of the horizontal Coriolis term is necessary in regards to the calculation of group speeds and the dispersion relation. The differences in group

speeds are even more apparent during ray tracing.

One of the short-term moorings is found to have a unique signal in depth-integrated dissipation. The two other upstream moorings show increased dissipation associated with the hydraulic jump at the sill. The anomalous mooring has a near-inertial signal in dissipation that is found to be related to the NIW observed at all moorings. It does not appear that the NIW induces increased mixing at observation depths. Increased meridional velocity, due to topographic acceleration around the secondary bump on the sill interacts with the meridional shear and causes enhanced mixing below the interface. The time-averaged, depth-integrated dissipation rate is comparable to those found at the two other upstream moorings.

6.2 Research highlights

- NIW are difficult to observe as they are episodic and propagate away from their origin region. When the difficulties of taking measurements in the deep ocean are taken into account, it becomes apparent that the Samoan Passage data set with the presence of NIWs is special. It is unique to be able to observe NIWs in the deep ocean let alone on an array in addition to a long-term mooring. These observations show a NIWs having propagated downward and equatorward into the region and the wave's superposition with 1/4 the amplitude upward propagating wave.

- Small scale variations in N^2, currents, and topography do make a difference on NIWs over small scales. Plane wave solutions show the NIW observed at the short-term moorings is coherent across all of the moorings. Yet there are variations in the depth ranges where the NIW is observed and the ellipticity of the wave at each mooring.

- As more research is done into NIWs in the interior ocean and near the equator, the inclusion of $\tilde{f}$ will become even more important. Ray tracing is currently one of the key tools for identifying propagation pathways. As this research has shown, there are distinct differences between

propagation paths when $\tilde{f}$ is included and when $\tilde{f}$ is not. As more observations become available and more research into the propagation paths of NIWs is possible, $\tilde{f}$ will need to be included.

- Alford et al. (2016) notes a distinct lack of full depth profiles between 30N and 30S; this is a key latitude range for the inclusion of $\tilde{f}$. As waves propagate equatorward from storm tracks and other generation sites, propagation paths will take the NIWs into the low latitude, low stratification regions, where the inclusion of $\tilde{f}$ will make a difference. Also, as more focus is placed on other sources of NI energy other than the wind (such as lee waves, wave-wave interactions and spontaneous generation), NIW research will occur more in regions with low N^2, another key area where $\tilde{f}$ must be included.

- NIW observations were not only observed on a single mooring but an array of moorings located around a sill. The NIW is observed at all moorings at depths corresponding to a peak in N^2 immediately above the AABW overflow depths. The moorings are located in various regimes below the interface (4200 m) at overflow depths: relatively quiescent flow (T12), flow over a hydraulically controlled sill (M5), downstream of the hydraulically controlled sill (T9 and T10), and in a meridionally accelerated flow (T11). The best-fit plane wave solution for all moorings is comprised of the interference pattern of two waves. The upward propagating wave has a few potential sources: internal reflection due to variations in N^2, bottom reflection, or a near-bottom/bottom source. In all of these situations, NI energy propagates past the interface in the overflow layer and thus should be observed below the interface at all moorings. It is only the interaction with the accelerated flow that increases mixing (T11).

As more deep and abyssal ocean observations occur, the spatial and temporal extent of NIWs in the interior of the ocean will become more apparent. It is also through these future data sets that generation, propagation, and dissipation of NIWs will be better understood. Although the data collected during SPAM-Ex is extensive, it is limited in that there are no observations of the corresponding NIW generation and, beyond the single downstream mooring, no observations of its ultimate dissipation. It is the author's hope that this research will inspire increased observations with the focus of NIWs

in the deep ocean, research on NIW interaction with accelerated flows, and the inclusion of $\tilde{f}$ in the appropriate circumstances.

6.3 Future work

- This research focuses on the southern sill. Future research should be expanded to include the entirety of data from SPAM-Ex, which includes moorings around two other sills in addition to other observations.
- The currents are known to interact with NIWs. However topographically accelerated flow is observed at T9, T10, and T11. T11 does observe the highest speed; however, it is the only mooring in the topographically accelerated flow not directly upstream of the hydraulic jump. Is it the magnitude of the velocity, the lack of increased mixing from the hydraulic jump, or something else that induces the increased mixing observed at T11 but not at T9 and T10?
- Some mixing occurs above the interface where the NIW is observed. Does this mixing correspond to the presence of the NIWs or is it always present? If it corresponds to the presence of the NIW, how does the magnitude of that mixing compare to the mixing due to the hydraulic jumps? As NIWs are known to be coherent over tens of kilometers, this mixing signal could occur over a large area multiple times a year.
- What happens to the NI energy observed at the moorings other than T11?
- Is all of the NI energy observed above the interface at T11 dissipated?
- What is the origin of the upward propagating wave?
- Inclusion of $\tilde{f}$ to other NIW observations.

CHAPTER 7

Appendix 1

7.1 Error Analysis

7.1.1 f_{eff}

Neglecting $\tilde{f}$

The error for f_{eff} is calculated using error propagation following Taylor (1982) and will be calculated in components for ease. We start with the numerator:

$$\delta(N\omega) = N\omega\sqrt{\left(\frac{\delta N}{N}\right)^2 + \left(\frac{\delta\omega}{\omega}\right)^2}. \tag{7.1}$$

Then calculate each component of the denominator:

$$\begin{aligned}\delta A = \delta[(r_l^2 - 1)m^2U^2\cos^2(\theta-\alpha)] = \\ (r_l^2 - 1)m^2U^2\cos^2(\theta-\alpha)\sqrt{\left(\frac{2\delta r_l}{r_l}\right)^2 + \left(\frac{2\delta m}{m}\right)^2 + \left(\frac{2\delta U}{U}\right)^2 + \left(\frac{2\delta\cos(\theta-\alpha)}{\cos(\theta-\alpha)}\right)^2}\end{aligned} \tag{7.2}$$

$$\delta(N^2 r_l^2) = N^2 r_l^2 \sqrt{\left(\frac{2\delta N}{N}\right)^2 + \left(\frac{2\delta r_l}{r_l}\right)^2} \tag{7.3}$$

where $\delta(\cos(\theta-\alpha)) = \sin(\theta-\alpha) * \sqrt{(\delta\theta)^2 + (\delta\alpha)^2}$. The error for the denominator is:

$$\delta(\text{denominator}) = \frac{\sqrt{(\delta A)^2 + (\delta(N^2 r_l^2))^2}}{\sqrt{(r_l^2 - 1)m^2 U^2 \cos^2(\theta-\alpha) + N^2 r_l^2}}. \tag{7.4}$$

As a result, we get the error for the effective frequency:

$$\delta f_{eff} = f_{eff} \sqrt{\left(\frac{\delta(N\omega)}{N\omega}\right)^2 + \left(\frac{\delta(\text{denominator})}{\text{denominator}}\right)^2} \tag{7.5}$$

Including $\tilde{f}$

The error is calculated piece by piece:

$$\delta[2m^2 G^2(1-r_l^2)] = 2m^2 G^2(1-r_l^2) \sqrt{\left(\frac{2\delta m}{m}\right)^2 + \left(\frac{2\delta G}{G}\right)^2 + \left(\frac{\delta r_l}{r_l}\right)^2} \tag{7.6}$$

$$\delta[r_l^2(2N^2+\tilde{f}^2)] = r_l^2(2N^2+\tilde{f}^2) \sqrt{\left(\frac{2\delta r_l}{r_l}\right)^2 + \left(\frac{4N\delta N}{2N^2+\tilde{f}^2}\right)^2} \tag{7.7}$$

$$\delta[2\sqrt{2} r_l m G \tilde{f}] = 2\sqrt{2} r_l m G \tilde{f} \sqrt{\left(\frac{\delta r_l}{r_l}\right)^2 + \left(\frac{\delta m}{m}\right)^2 + \left(\frac{\delta G}{G}\right)^2} \tag{7.8}$$

and we get the error for A:

$$\delta A = \sqrt{(\delta[2m^2 G^2(1-r_l^2)])^2 + (\delta[r_l^2(2N^2+\tilde{f}^2)])^2 + (\delta[2\sqrt{2} r_l m G \tilde{f}])^2}. \tag{7.9}$$

Next we calculate the error for B:

$$\delta B = 2\sqrt{2}\tilde{f}\omega m G \sqrt{\left(\frac{\delta\tilde{f}}{\tilde{f}}\right)^2 + \left(\frac{\delta\omega}{\omega}\right)^2 + \left(\frac{\delta m}{m}\right)^2 + \left(\frac{\delta G}{G}\right)^2} \tag{7.10}$$

and for C:

$$\delta C = \omega^2(2N^2+\tilde{f}^2)\sqrt{\left(\frac{2\delta\omega}{\omega}\right)^2+\left(\frac{\sqrt{(4N\delta N)^2+(\delta\tilde{f})^2}}{2N^2+\tilde{f}^2}\right)^2} \tag{7.11}$$

Using these three components we calculate the error for the quadratic formula where the error for the numerator is calculated using:

$$\delta\text{Numerator} = \sqrt{(\delta B)^2+\left(\frac{\sqrt{B^2-4AC}\sqrt{(2B\delta B)^2+\left(4AC\sqrt{(\frac{\delta A}{A})^2+(\frac{\delta C}{C})^2}\right)}}{2(B^2-4AC)}\right)^2}. \tag{7.12}$$

$$\delta\text{Quadratic} = \frac{-B\pm\sqrt{B^2-4AC}}{2A}\sqrt{\left(\frac{\delta\text{Numerator}}{\text{Numerator}}\right)^2+\left(\frac{\delta A}{A}\right)^2} \tag{7.13}$$

Finally, we get the equation for the error on the effective frequency:

$$\delta f_{eff} = \frac{-B\pm\sqrt{B^2-4AC}}{2A}\sqrt{\left(\frac{2\delta A}{2A}\right)^2+\frac{(\delta B)^2+\frac{(2B\delta B)^2+\left(4AC\sqrt{\left(\frac{\delta A}{A}\right)^2+\left(\frac{\delta C}{C}\right)^2}\right)^2}{4(B^2-4AC)}}{(-B\pm\sqrt{B^2-4AC})^2}} \tag{7.14}$$

7.1.2 Intrinsic frequency

$$\omega_l = r_l f_{eff}\sqrt{\left(\frac{\delta r_l}{r_l}\right)^2+\left(\frac{\delta f_{eff}}{f_{eff}}\right)^2} \tag{7.15}$$

7.1.3 k_H

Neglecting $\tilde{f}$

$$\delta k_H = \frac{1}{2}\sqrt{\frac{m^2 f_{eff}^2(r_l^2)}{N^2}}\sqrt{\left(\frac{2\delta m}{m}\right)^2+\left(\frac{2\delta f_{eff}}{f_{eff}}\right)^2+\left(\frac{2\delta r_l}{r_l}\right)^2+\left(\frac{2\delta N}{N}\right)^2} \tag{7.16}$$

Including $\tilde{f}$

We find the errors for the components of the quadratic equation:

$$\delta A = 2N\delta N, \tag{7.17}$$

$$\delta B = \sqrt{2} f_{eff} \tilde{f} m \sqrt{\left(\frac{\delta f_{eff}}{f_{eff}}\right)^2 + \left(\frac{\delta m}{m}\right)^2} \tag{7.18}$$

and

$$\delta C = m^2 f_{eff}^2 (1 - r_l^2) \sqrt{\left(\frac{2\delta m}{m}\right)^2 + \left(\frac{2\delta f_{eff}}{f_{eff}}\right)^2 + \left(\frac{2\delta r_l}{r_l}\right)^2} \tag{7.19}$$

Then we use the the quadratic equation error, Eqn. 7.13 to find the horizontal wavenumber error.

7.1.4 Group speed

Neglecting $\tilde{f}$

We can calculate the error on the group speeds using:

$$\delta c_{gx} = \frac{kN^2}{m^2 \sqrt{f_{eff}^2 + \frac{N^2 k_H^2}{m^2}}} \sqrt{\left(\frac{2\delta m}{m}\right)^2 + \left(\frac{\delta(\text{numerator})}{\text{numerator}}\right)^2 + \left(\frac{\delta\left(\sqrt{f_{eff}^2 + \frac{N^2 k_h^2}{m^2}}\right)}{\sqrt{f_{eff}^2 + \frac{N^2 k_H^2}{m^2}}}\right)^2} \tag{7.20}$$

where:

$$\delta(\text{numerator}) = kN^2 \sqrt{\left(\frac{\delta k}{k}\right)^2 + \left(\frac{2\delta N}{N}\right)^2} \tag{7.21}$$

and

$$\delta\left(\sqrt{f_{eff}^2 + \frac{N^2 k_H^2}{m^2}}\right) = \frac{\sqrt{(2 f_{eff} \delta f_{eff})^2 + \left(\frac{N^2 k_H^2}{m^2} \sqrt{\left(\frac{2\delta N}{N}\right)^2 + \left(\frac{2\delta k_H}{k_H}\right)^2 + \left(\frac{2\delta m}{m}\right)^2}\right)}}{\sqrt{f_{eff}^2 + \frac{N^2 k_H^2}{m^2}}}. \tag{7.22}$$

The error for c_{gy} is the same as Eqn. 7.20 with δl and l instead of δk and k. The error on the vertical group speed is calculated using:

$$\delta c_{gz} = \frac{N^2 k_H^2}{m^2 \sqrt{f_{eff}^2 + \frac{N^2 k_H^2}{m^2}}} \sqrt{\left(\frac{2\delta N}{N}\right)^2 + \left(\frac{2\delta k_H}{k_H}\right)^2 + \left(\frac{3\delta m}{m}\right)^2 + \left(\frac{\delta\left(\sqrt{f_{eff}^2 + \frac{N^2 k_H^2}{m^2}}\right)}{\sqrt{f_{eff}^2 + \frac{N^2 k_H^2}{m^2}}}\right)^2} \tag{7.23}$$

using Eqn. 7.22.

Including $\tilde{f}$

The error for the group speeds are calculated using the following equations:

$$\delta c_{gx} = \frac{k(N^2 - \tilde{\omega}^2)}{\tilde{\omega} m^2} \sqrt{\left(\frac{\delta k}{k}\right)^2 + \left(\frac{\sqrt{(2N\delta N)^2 + (2\tilde{\omega}\delta\tilde{\omega})^2}}{N^2 - \tilde{\omega}^2}\right)^2 + \left(\frac{\delta\tilde{\omega}}{\tilde{\omega}}\right)^2 + \left(\frac{2\delta m}{m}\right)^2}, \tag{7.24}$$

$$\delta c_{gy} = \frac{l(N^2 + \tilde{f}^2 - \tilde{\omega}^2) + f_{eff}\tilde{f}m}{\tilde{\omega} m^2} \sqrt{\left(\frac{\delta \text{numerator}}{\text{numerator}}\right)^2 + \left(\frac{\delta\tilde{\omega}}{\tilde{\omega}}\right)^2 + \left(\frac{2\delta m}{m}\right)^2} \tag{7.25}$$

where:

$$\delta \text{numerator} = \sqrt{\left(l(N^2 + \tilde{f}^2 - \tilde{\omega}^2)\sqrt{\left(\frac{\delta l}{l}\right)^2 + \left(\frac{\sqrt{(2N\delta N)^2 + (2\tilde{\omega}\delta\tilde{\omega})^2}}{N^2 + \tilde{f}^2 - \tilde{\omega}^2}\right)^2}\right) + \left(f_{eff}\tilde{f}m\sqrt{\left(\frac{\delta f_{eff}}{f_{eff}}\right)^2 + \left(\frac{\delta m}{m}\right)^2}\right)}, \tag{7.26}$$

and

$$\text{numerator} = l(N^2 + \tilde{f}^2 - \tilde{\omega}^2) + f_{eff}\tilde{f}m \tag{7.27}$$

and finally:

$$\delta c_{gz} = \frac{\tilde{f} f_{eff} l + m(f_{eff}^2 - \tilde{\omega}^2)}{\tilde{\omega} m^2} \sqrt{\left(\frac{\delta \text{numerator}}{\text{numerator}}\right)^2 + \left(\frac{\delta\tilde{\omega}}{\tilde{\omega}}\right)^2 + \left(\frac{2\delta m}{m}\right)^2} \tag{7.28}$$

where:

$$\delta\text{numerator} = \sqrt{\left(f_{eff}\tilde{f}l\sqrt{\left(\frac{\delta f_{eff}}{f_{eff}}\right)^2+\left(\frac{\delta l}{l}\right)^2}\right)^2+\left(\frac{\delta m(f_{eff}^2-\tilde{\omega}^2)}{m(f_{eff}^2-\tilde{\omega}^2)}\right)^2} \tag{7.29}$$

and

$$\text{numerator} = \tilde{f}f_{eff}l + m(f_{eff}^2-\tilde{\omega}^2). \tag{7.30}$$

7.1.5 Water properties errors

The error for N and r_l are one standard deviation of all the observed values. The errors for ω and m are found using t-score. The errors for U and α were calculated using error propagation as follows:

$$\delta U = \frac{\sqrt{(2u\delta u)^2+(2v\delta v)^2}}{\sqrt{u^2+v^2}} \tag{7.31}$$

and

$$\delta\alpha = \frac{uv}{u^2+v^2}\sqrt{\left(\frac{\delta u}{u}\right)^2+\left(\frac{\delta v}{v}\right)^2} \tag{7.32}$$

where $|U| = \sqrt{u^2+v^2}$ and $\alpha = \arctan\left(\frac{u}{v}\right)$.

7.1.6 Ray Tracing

$\frac{dx}{dt}$

$$\delta\left(\frac{dx}{dt}\right) = \sqrt{(\delta c_{gx})^2+\left(|U|\cos(\alpha)\sqrt{(\delta\alpha\tan(\alpha))^2+\left(\frac{\delta U}{U}\right)^2}\right)^2} \tag{7.33}$$

$\frac{dy}{dt}$

$$\delta\left(\frac{dy}{dt}\right) = \sqrt{(\delta c_{gy})^2+\left(|U|\cos(\alpha)\sqrt{(\delta\alpha\tan(\alpha))^2+\left(\frac{\delta U}{U}\right)^2}\right)^2} \tag{7.34}$$

$\frac{dz}{dt}$

$$\delta\left(\frac{dz}{dt}\right) = \delta c_{gz} \tag{7.35}$$

$\frac{dl}{dt}$

$$\delta\left(\frac{dl}{dt}\right) = \frac{f_{eff}}{\omega_l}\beta\sqrt{\left(\frac{\delta f_{eff}}{f_{eff}}\right)^2 + \left(\frac{\delta\omega_l}{\omega_l}\right)^2} \tag{7.36}$$

CHAPTER 8

Appendix 2

8.1 Derivations

8.1.1 $\Delta_{\tilde{\omega}^2}$

Following Guiles (2004) we calculate the general percent difference for the dispersion relation as a function of $\tilde{f}$ and N. We start by converting the dispersion relation:

$$\tilde{\omega} = \frac{N^2 * K_H^2 + (\tilde{f}l + fm)^2}{K^2}, \tag{8.1}$$

into independent variables using the following conversions:

$$\cos\theta = \frac{\tilde{k_H} \cdot \tilde{K}}{|\tilde{k_H}||\tilde{K}|} \tag{8.2}$$

and

$$\cos\alpha = \frac{\tilde{\Omega} \cdot \tilde{K}}{|\tilde{\Omega}||\tilde{K}|}, \tag{8.3}$$

where θ ($-\frac{\pi}{2} \leq \theta \leq \frac{\pi}{2}$) is the angle the wavenumber vector makes with the local horizontal and

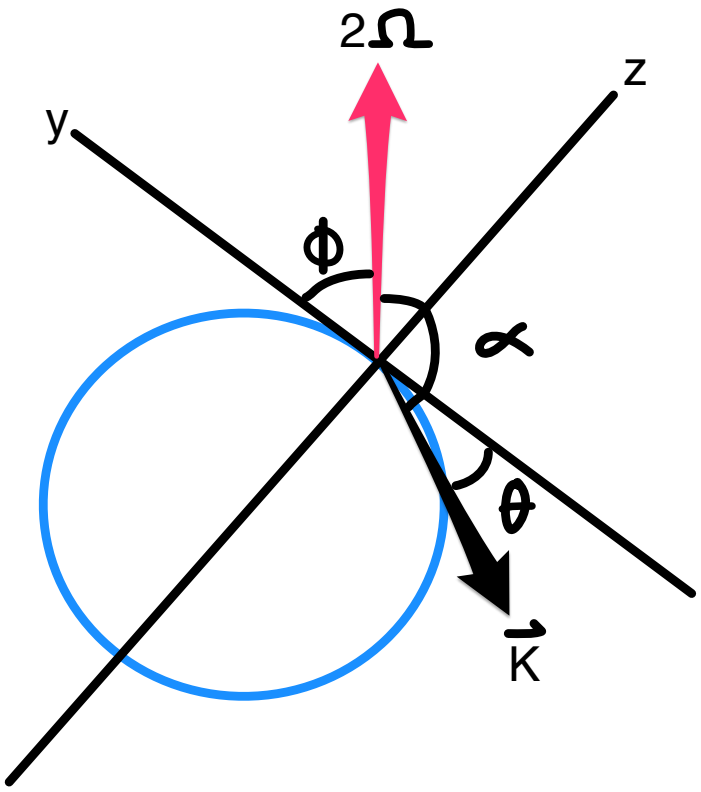

Figure 8.1: Schematic of the our independent variable conversion. θ is the angle between the wavevector and the local horizon, ϕ is the latitude and α is the angle between the wave vector and the rotation vector.

α ($0 \leq \alpha \leq \pi$) is the angle the wavenumber vector makes with the rotation vector (Fig. 8.1). The resulting dispersion relations (neglecting $\tilde{f}$ and including $\tilde{f}$ respectively):

$$\omega^2 = N^2\cos^2\theta + f^2\sin^2\theta \tag{8.4}$$

$$\tilde{\omega}^2 = N^2\cos^2\theta + (2\Omega)^2\cos^2\alpha \tag{8.5}$$

are plugged into the equation for the percent difference:

$$\Delta = \frac{\tilde{\omega}^2 - \omega^2}{\omega^2} \tag{8.6}$$

to get:

$$\Delta = \frac{\tilde{f}^2 + 2f\tilde{f}\tan\theta}{N^2 + f^2\tan^2\theta}. \tag{8.7}$$

We diverge from Guiles (2004) as apply the inertial limit as θ approaches $\frac{\pi}{2}$ to Eqn. 8.7 to get the percent difference for near-inertial waves (Fig. 4.14). Guiles (2004) assesses for the entire spectrum of internal waves while we are only concerned with NIW near the inertial limit.

8.1.2 $\Delta_{\tilde{c}_{gy}}$

We expand the techniques used in Guiles (2004) to calculate the general equation for the percent difference of $\tilde{c}_{gy}$, as we approach the inertial limit, as a function of only $\tilde{f}$ and N. The equations for c_{gy} (Eqn. 4.17) and $\tilde{c}_{gy}$ (Eqn. 4.14) are substituted into the equation for the percent difference:

$$\Delta = \frac{\tilde{c}_{gy} - c_{gy}}{c_{gy}} \tag{8.8}$$

and are converted to independent variables:

$$\Delta = \frac{(N^2 + \tilde{f}^2 - N^2\cos^2\theta - \tilde{f}^2\cos^2\theta - 2f\tilde{f}\cos\theta\sin\theta - f^2\sin^2\theta + \sqrt{2}f\tilde{f}\tan\theta)(f^2 + N^2\cot^2\theta)^{1/2}}{N^2(N^2\cos^2\theta + \tilde{f}^2\cos^2\theta + 2f\tilde{f}\cos\theta\sin\theta + f^2\sin^2\theta)^{1/2}}. \tag{8.9}$$

Then, we apply the limit as θ approaches $\frac{\pi}{2}$ to find the percent difference for NIW:

$$\Delta = \frac{\tilde{f}^2}{N^2} + \frac{f^2}{N^2} + \frac{\sqrt{2}\tilde{f}}{N} + \frac{\sqrt{2}f\tilde{f}\tan\theta}{N^2}. \tag{8.10}$$

We use $\tan\theta = 705$ as that is the value calculated from our ratio of m and k_H. Increasing/decreasing this translates the percentages to the right/left about 0.001 N. Unless the ratio of m to k_H varies dramatically from that used here, the authors expect a similar percent difference for other NIW observations.

We limit our calculations of the potential difference as a function of the latitude and N to the dispersion relation and the group speeds.

Bibliography

Alford, M. (2003). Redistribution of energy available for ocean mixing by long-range propagation of internal waves. *Letters to Nature*, 423, 159–162.

Alford, M. (2008). Observations of parametric subharmonic instability of the diurnal internal tide in the South China Sea. *Geophysical Research Letters*, 35, L15602.

Alford, M. (2010). Sustained, full-water-column observations of internal waves and mixing near Mendocino Escarpment. *Journal Physical Oceanography*, 40.

Alford, M., Cronin, M., & Klymak, J. (2012). Annual cycle and depth penetration of wind-generated near-inertial waves at ocean Station Papa in the northeast Pacific. *Journal of Physical Oceanography*, 42, 889–909.

Alford, M., Girton, J., Voet, G., Carter, G., Mickett, J., & Klymak, J. (2013). Turbulent mixing and hydraulic control of abyssal water in the Samoan Passage. *Geophysical Research Letters*, 40, 4668–4674.

Alford, M. & Gregg, M. (2001). Near-inertial mixing: modulation of shear, strain and microstructure at low latitude. *Journal of Geophysical Research*, 106(C8), 16947–16968.

Alford, M., MacKinnon, J., Pinkel, R., & Klymak, J. (2017). Space-time scales of shear in the North Pacific. *Journal of Physical Oceanography*, 47.

Alford, M., MacKinnon, J., Simmonds, H., & Nash, J. (2016). Near-inertial internal gravity waves in the ocean. *Annual Review of Marine Science*, 8, 95–123.

Alford, M., MacKinnon, J., Zhao, Z., Pinkel, R., Klymak, J., & Peacock, T. (2007). Internal waves across the Pacific. *Geophysical Research Letters*, 81.

Alford, M. & Whitmont, M. (2007). Seasonal and spatial variability of near-inertial kinetic energy from historical moored velocity records. *Journal of Physical Oceanography*, 37, 2022–2037.

Althaus, A., Kunze, E., & Sanford, T. (2003). Internal tide radiation from Mendocino Escarpment. *Journal Physical Oceanography*, 33.

Cairns, J. & Williams, G. (1976). Internal wave observations from a midwater float, 2. *Journal of Geophysial Research*, 34.

Cusack, J., Alford, M., Voet, G., & Pearson-Potts, K. (In prep.). Persistence and variability of turbulence in an abyssal passage.

D'Asaro, E. (1985). The energy flux from the wind to near-inertial motions in the surface mixed layer. *Journal of Physical Oceanography*, 15, 1043–1059.

D'Asaro, E. (1989). The decay of wind-forced mixed layer inertials oscillations due to the β effect. *Journal of Geophysical Research*, 94, 148–227.

D'Asaro, E. (1995). Upper-ocean inertial currents forced by a strong storm. part ii: Modeling. *Journal of Physical Oceanography*, 25, 2937–2952.

Davies, T., Cullen, M., Malcolm, A., Mawson, M., Staniforth, A., White, A., & Wood, N. (2005). A new dynamical core for the Met Office's global and regional modelling of the atmosphere. *Quarterly Journal of the Royal Meteorological Society*, 131.

Doherty, K., Frye, D., Liberatore, S., & Toole, J. (1999). A moored profiling instrument. *Journal of Atmospheric and Oceanic Technology*.

Ekman, V. (1953). Studies on ocean currents: Results of a cruise on board the "Armauer Hansen" in 1930 under the leadership of Bjorn Helland-Hansen. *Geofysiske Publikasjoner*, 19.

Eriksen, C. (1982). Observations of internal wave reflection off sloping bottoms. *Journal of Geophysical Research*, 87, 525–538.

Eriksen, C. (1985). Implications of ocean bottom reflection for internal wave spectra and mixing. *Journal of Physical Oceanography*, 15, 1145–1156.

Fer, I., Voet, G., Seim, K., Rudels, B., & Latarius, K. (2010). Intense mixing of the Faroe Bank Channel overflow. *Geophysical Research Letters*, 37.

Ferron, B., Mercier, H., Speer, K., Gargett, A., & Polzin, K. (1998). Mixing in the Romanche Fracture Zone. *Journal of Physical Oceanography*, 28, 1929–1945.

Freeland, H. (2001). Observations of the flow of abyssal water through the Samoa Passage. *Journal of Physical Oceanography*, 31, 2273–2279.

Fu, L. (1981). Observations and models of inertial waves in the deep ocean. *Reviews of Geophysics*, 19(1), 141–170.

Fukasawa, M., Freeland, H., Perkin, R., Watanabe, T., Uchida, H., & Nishina, A. (2004). Bottom water warming in the North Pacific Ocean. *Nature*, 427, 825–827.

Furuichi, N., Hibiya, T., & Niwa, Y. (2008). Model predicted distribution of wind-induced internal wave energy in the world's oceans. *Journal of Geophysical Research*, 113, C09034.

Garrett, C. (2001). What is the "near-inertial" band and why is it different from the rest of the internal wave spectrum. *Journal of Physical Oceanography*, 31, 962–971.

Garrett, C. & Monk, W. (1972). Space-time scales of internal waves. *Geophysical Fluid Dynamics*, 2, 225–264.

Garrett, C. & Munk, W. (1975). Space-time scales of internal waves:A progress report. *Journal of Geophysical Research*, 80, 291–297.

Gerkema, T. & Shira, V. (2005). Near-inertial waves on the "nontraditional" plane. *Geophysical Research Letters*, 110.

Gill, A. (1984). On the behavior of internal waves in the wakes of storms. *Journal of Physical Oceanography*, 14, 1129–1151.

Gonnella, J. (1972). A rotary-component method for analyzing meteorological and oceanographic vector time series. 19, 833–846.

Grinsted, A., Moore, J., & Jevrejeva, S. (2004). Application of the cross wavelet transporm and wavelet coherence to geophysical time series. *Nonlinear Processes in Geophysics*, 11, 561–566.

Guiles, M. (2004). Investigation of the Horizontal Coriolis Component. Master's thesis, University of Hawaii at Manoa.

Hazewinkel, J. & Winters, K. (2011). PSI of the internal tide on a β plane: flux divergence and near-inertial wave propagation. *Journal of Physical Oceanography*, 41, 1673–1682.

Hebert, H. & Moum, J. (1994). Decay of a near-inertial wave. *Journal of Physical Oceanography*, 24, 2334–2351.

Hogg, N., Biscaye, P., Gardner, W., & Schmidt, W. (1982). On the transport and modification of Antarctic bottom water in the Vema Channel. *Journal of Marine Research*, 40, 231–263.

Johnson, G., Rudnick, D., & Taft, B. (1994). Bottom water variability in the Samoa Passage. *Journal of Marine Research*, 52, 177–196.

Johnston, S., Chaudhuri, D., Mathur, M., Rudnick, D., Sengupta, D., Simmons, H., Tandon, A., & Venkatesan, R. (2016). Decay mechanisms of near-inertial mixed layer oscillations in the bay of bengal. *Oceanography*, 29, 180–191.

Kasahara, A. (2010). A mechanism of deep-ocean mixing due to near-inertial waves generated by flow over bottom topography. *Dynamics of Atmospheres and Oceans*, 49, 124–140.

Kunze, E. (1985). Near-inertial wave propogation in geostrophic shear. *Journal of Physical Oceanography*, 15, 544–565.

Kunze, E. & Sanford, T. (1986). Near-inertial wave interactions with mean flow and bottom topography near Caryn Seamount. *Journal of Physical Oceanography*, 16, 109–120.

Leaman, K. & Sanford, T. (1975). Vertical energy propagation of inertial waves: A vector spectral analysis of velocity profiles. *Journal of Geophysical Research*, 80, 1975–1978.

Lighthill, J. (1978). *Waves in Fluids*. Number pp. 317-337. Cambridge University Press.

MacKinnon, J., Johnston, T., & Pinkel, R. (2008). Strong transport and mixing of deep water through the Southwest Indian Ridge. *National Geoscience*, 1, 755–758.

Marshall, J., Adcroft, A., Hill, C., Perelman, L., & Heisey, C. (1997). A finite-volume, incompressible Navier Stokes model for studies of the ocean on parallel computers. *Journal Geophysical Research - Oceans*, 102.

McComas, C. & Muller, P. (1981). The dynamic balance of internal waves. *Journal of Physical Oceanography*, 11, 970–986.

Mooers, C. (1973). A technique for the cross spectrum analysis of pairs of complex-valued time series, with emphasis on properties of polarized components and rotational invariants. *Deep Sea Research and Oceanographic Abstracts*, 20, 1129–1141.

Muller, P., Holloway, G., Henyey, F., & Pomphrey, N. (1986). Nonlinear interactions among internal gravity waves. *Reviews of Geophysics*, 24, 493–536.

Munk, W. (1981). *Evolution of Physical Oceanography: Internal waves and small scale processes*. Number pp. 623. The MIT Press.

Needler, G. & LeBlond, P. (1973). On the influence of the horizontal component of the earth's rotation on long period waves. *Geophysical Fluid Dynamics*, 5.

Nikurashin, M. & Ferrari, R. (2010a). Radiation and dissipation of internal waves generated by geostrophic motions impinging on small-scale topography: Application to the Southern Ocean. *Journal of Physical Oceanography*, 40, 2025–2042.

Nikurashin, M. & Ferrari, R. (2010b). Radiation and dissipation of internal waves generated by geostrophic motions impinging on small-scale topography: theory. *Journal of Physical Oceanography*, 40, 1055–1074.

Olbers, D. (1981). The propagation of internal waves in a geostrophic current. *Journal of Physical Oceanography*, 11, 1224–1233.

Pinkel, R. (1985). A wavenumber-frequency spectrum of upper ocean shear. *Journal of Physical Oceanography*, 15, 1453–1569.

Polzin, K., Toole, J., Ledwell, J., & Schmitt, R. (1997). Spatial variability of turbulent mixing in the abyssal ocean. *Science*, 276, 93–96.

Purkey, S. & Johnson, G. (2013). Antarctic Bottom Water warming and freshening: Contributions to sea level rise, ocean freshwater budgets, and global heat gain. *Journal Climate*, 26, 6105–6122.

Reid, J. & Lonsdale, P. (1974). On the flow of water through the Samoan Passage. *Journal of Physical Oceanography*, 13, 1544–1549.

Roemmich, D., Huatala, S., & Rudnick, D. (1996). Northward abyssal transport through the Samoan Passage and adjacent regions. *Journal of Geophysical Research*, 101, 14039–14055.

Rudnick, D. (1997). Direct velocity measurements in the Samoan Passage. *Journal of Geophysical Research*, 102(C2), 3293–3302.

Silverthorne, K. & Toole, J. (2009). Seasonal kinetic energy variability of near-inertial motions. *Journal of Physical Oceanography*, 39, 1035–1039.

Simmonds, H. (2008). Spectral modifications and geographic redistribution of the semi-diurnal internal tide. *Ocean Model*, 21, 126–138.

Simmons, H. & Alford, M. (2012). Simulating the long-range swell of internal waves generated by ocean storms. *Oceanography*, 25, 30–41.

Sloyan, B., Wijffels, S., Tilbrook, B., Katsumata, K., Murata, A., & Macdonald, A. (2013). Deep ocean changes near the western boundary of the South Pacific Ocean. *Journal of Physical Oceanography*, 43, 2132–2141.

Stommel, H. (1958). The abyssal circulation. *Deep Sea Research*, 5, 80–82.

Taft, B., Hayes, S., Friederich, G., & Codispoti, L. (1991). Flow of abyssal water into the Samoa Passage. *Deep-Sea Research I*, 38, S103–S128.

Taylor, J. (1982). *An introduction to error analysis the study of uncertainties in physical measurements*. Number 270p. University Science Books Oxford University Press.

Tomczak, M. & Godfrey, J. (2003). *Regional Oceanography: an Introduction*. Number 390p. Daya Publishing House.

van Haren, H. & Millot, C. (2004). Rectilinear and circular inertial motions in the Western Mediterranean Sea. *Deep-Sea Research I*, 51.

Vanneste, J. (2012). Balance and spontaneous wave generation in geophysical flows. *Annual Review of Fluid Mechanics*, 45, 147–172.

Voet, G., Alford, M., Girton, J., Carter, G., Mickett, J., & Klymak, J. (2016). Warming and weakening of the flow through Samoan Passage. *Journal of Physical Oceanography*, 46(8).

Voet, G., Girton, J., Alford, M., Carter, G., Klymak, J., & Mickett, J. (2015). Pathways, volume transport, and mixing of abyssal water in the Samoan Passage. *Journal of Physical Oceanography*, 45, 562–588.

Warren, B. (1983). Why is no deep water formed in the North Pacific? *Journal of Marine Research*, 41, 327–347.

Webster, F. (1968). Observation of inertial period motions in the deep sea. *Review Geophysics*, 6, 473–490.

White, A. & Bromley, R. (1995). Dynamically consistent quasi-hydrostatic equations for global models with a complete representation of the Coriolis force. *Quarterly Journal of the Royal Meteorological Society*, 121.

Winters, J. M. K. (2005). Suptropical catastrophe significant loss of low-mode tidal energy at 28.9°. *Geophysical Research Letters*, 32.

Wunsch, C. & Ferrari, R. (2004). Vertical mixing, energy, and the general circulation of the oceans. *Annual Review of Fluid Mechanics*, 36, 281–314.